



Michigan Technological University
Create the Future Digital Commons @ Michigan Tech

Dissertations, Master's Theses and Master's
Reports - Open

Dissertations, Master's Theses and Master's
Reports

2013

NONLINEAR EFFECTS IN MAGNETIC GARNET FILMS AND NONRECIPROCAL OPTICAL BLOCH OSCILLATIONS IN WAVEGUIDE ARRAYS

Pradeep Kumar
Michigan Technological University

Follow this and additional works at: <https://digitalcommons.mtu.edu/etds>


 Part of the [Optics Commons](#)

Copyright 2013 Pradeep Kumar

Recommended Citation

Kumar, Pradeep, "NONLINEAR EFFECTS IN MAGNETIC GARNET FILMS AND NONRECIPROCAL OPTICAL BLOCH OSCILLATIONS IN WAVEGUIDE ARRAYS", Dissertation, Michigan Technological University, 2013.
<https://doi.org/10.37099/mtu.dc.etds/482>

Follow this and additional works at: <https://digitalcommons.mtu.edu/etds>

 Part of the [Optics Commons](#)

NONLINEAR EFFECTS IN MAGNETIC GARNET FILMS AND
NONRECIPROCAL OPTICAL BLOCH OSCILLATIONS IN WAVEGUIDE
ARRAYS

By
Pradeep Kumar

A DISSERTATION

Submitted in partial fulfillment of the requirements for the degree of

DOCTOR OF PHILOSOPHY

In Engineering Physics

MICHIGAN TECHNOLOGICAL UNIVERSITY

©2013 Pradeep Kumar

This dissertation has been approved in partial fulfillment of the requirements for the Degree of DOCTOR OF PHILOSOPHY in Engineering Physics.

Department of Physics

Dissertation Advisor: *Dr. Miguel Levy.*

Committee Member: *Dr. Kim Fook Lee.*

Committee Member: *Dr. Will H. Cantrell.*

Committee Member: *Dr. Durdu O. Guney.*

Department Chair: *Dr. Ravindra Pandey.*

To My Family

Table of Contents

List of Figures	vii
List of Tables.....	xii
Preface	xiii
Acknowledgements	xv
Abbreviations.....	xvii
Abstract.....	xviii
1. Introduction.....	1
1.1. Literature review	2
1.2. Dissertation outline	5
2. Magnetic Garnets: Properties and Applications	7
2.1. Types of magnetism in magnetic materials.....	7
2.2. Garnet crystal structure	9
2.2.1. YIG structure	10
2.2.2. Bi-substituted YIG.....	12
2.2.3. Ce-substituted YIG	13
2.3. Thin film fabrication and characterization techniques.....	13
2.3.1. Liquid phase epitaxy (LPE)	15
2.3.2. Pulsed laser deposition (PLD).....	15
2.3.3. Sputtering.....	16
2.3.4. Film characterization.....	19
2.4. Magnetic garnet thin-film-based applications.....	20
2.5. Garnet-semiconductor integration: issues and solutions.....	22
3. Second Harmonic Generation in Bi:YIG Films*.....	25
3.1. Aim and motivation.....	25
3.2. Theoretical background.....	26
3.2.1. The nonlinear susceptibility.....	26
3.2.2. The SHG process.....	28
3.2.3. SHG in magnetic garnet films.....	30
3.3. Experimental methods.....	32
3.3.1. Film fabrication: tools and techniques	33

3.3.2.	Film characterization.....	38
3.3.3.	Types of strain and their determination	43
3.3.4.	Strain measurements	45
3.3.5.	SHG measurements	47
3.4.	Results and discussion.....	50
3.4.1.	The role of substrates in SHG.....	50
3.4.2.	The role of oxygen in SHG.....	51
3.4.3.	The role of annealing in SHG.....	54
3.4.4.	The role of film thickness in SHG.....	55
3.4.5.	The role of interface in SHG	56
3.4.6.	The role of lattice mismatch, micro-strain, and composition in SHG	58
3.4.7.	Hyper-Rayleigh scattering (HRS) study.....	63
3.4.8.	Surface effects investigation.....	64
3.5.	Summary	66
4.	Nonreciprocal and Unidirectional Optical Bloch Oscillations in Asymmetric Waveguide Arrays**	67
4.1.	Introduction and background	67
4.1.1.	An overview on Bloch oscillation phenomena.....	69
4.1.2.	Beam dynamics in a dielectric waveguide	71
4.2.	Analytical study	78
4.2.1.	Nonreciprocal phase shift (NRPS) effect.....	79
4.2.2.	Nonreciprocal BO in magneto-optic waveguide arrays	80
4.2.3.	Unidirectional BO in garnet/SOI waveguide arrays.....	92
4.2.4.	On-chip optical isolation via unidirectional Bloch oscillations.....	98
4.3.	Array designs, performance and fabrication	105
4.4.	Summary	110
5.	Conclusions and Future Work	111
5.1.	Conclusions	111
5.2.	Future work	112
	Reference List	114
	Publications & Achievements.....	123
	Appendix 1.....	125
	Appendix 2.....	130

Appendix 3.....	131
Appendix 4.....	133
Appendix 5.....	134
Appendix 6.....	137
Appendix 7.....	138
Appendix 8.....	141
Appendix 9.....	143
Appendix 10.....	144

List of Figures

Fig. 1.1. Thin-film material based technological applications [4].	1
Fig. 2.1. Ordering of magnetic dipole moments in magnetic materials.	9
Fig. 2.2. An illustration of the yttrium iron garnet (YIG) lattice structure, highlighting the ionic arrangement in a unit cell [56].	11
Fig. 2.3. Schematics showing typical steps in a, (a) physical vapor deposition (PVD) process, and (b) chemical vapor deposition (CVD) process.	14
Fig. 2.4. Liquid phase epitaxy (LPE) set-up.	16
Fig. 2.5. Schematic view of a PLD-system.	16
Fig. 2.6. Schematic view of a DC sputtering system.	18
Fig. 2.7. Schematic view of a RF sputtering system. Here a RF generator (13.56 MHz) with a matching network is used; this allows sputtering of the insulating materials.	19
Fig. 2.8. A picture showing a prototype photonics crystal waveguide switch device developed by Levy and coworkers [52].	21
Fig. 2.9. Schematic view of a magneto-photonic crystal chemical sensor developed by Levy and coworkers [73].	22
Fig. 2.10. A schematic, showing the cross-sectional view of a SOI substrate with a garnet cover layer. Inset is highlighting the lattice mismatch at the interface layer. Typical lattice constants of the materials are given in the brackets.....	23
Fig. 2.11. Schematic of surface activated direct wafer bonding technique [85].	24
Fig. 3.1. Graphical illustrations showing, optical polarization (P) Vs optical electric field vector (E), for linear and nonlinear optical responses in a medium.	27
Fig. 3.2. (a) Geometrical representation of SHG. (b) Illustration of SHG using the energy-level diagram.	29
Fig. 3.3. Schematic representations of space-inversion and time-reversal symmetry operations. Image on the right also highlights the time-reversal symmetry in particles possessing electric dipole moments (e.g. electrons).	30
Fig. 3.4. Schematic representation of plasma confinement in a conventional magnetron system.	34
Fig. 3.5. Schematic and picture of the RF-magnetron sputtering system used in the present study.	34
Fig. 3.6. Schematic representation of Bi:YIG thin film growth process. The sputtering process is highlighted in the inset (for details see section 2.3.3).	35
Fig. 3.7. Typical film growth parameters used to grow Bi:YIG thin films.	36
Fig. 3.8. Scintag XDS-2000 θ/θ diffractometer used for x-ray measurements of Bi:YIG films.	39

Fig. 3.9. XRD pattern of BiYIG080607 film deposited without oxygen (upper graph) and of BiYIG120507 film deposited with oxygen (lower graph).....	40
Fig. 3.10. (a) Schematic of a prism coupler, and (b) illustration of measured spectrum showing dips in the intensity at various mode angles.	41
Fig. 3.11. RBS experimental setup.....	43
Fig. 3.12. Peak fit of (444) sample peak of a typical Bi:YIG sample using symmetrical Pearson VII profiles. Both film and substrate profiles have two peaks corresponding to XRD $K\alpha_1$ and $K\alpha_2$ lines.....	45
Fig. 3.13. Depth profiles of elemental concentrations in a typical sample	46
Fig. 3.14. Experimental Setup for SHG measurements.	48
Fig. 3.15. Dependences of SHG signal on azimuthal angle of rotation for a sample shined on from film side (graph on left) and same sample shined on from substrate side (graph on right)	49
Fig. 3.16. SHG rotational anisotropy of GGG (left graph) and CMG:GGG (right graph) substrates.....	51
Fig. 3.17. (a) SHG measurement for film prepared with oxygen (in Argon + Oxygen), (b) SHG measurement for film prepared without oxygen (in Argon only).	52
Fig. 3.18. SHG rotational anisotropy of (a) BiYIG111507 (in Ar + O ₂), (b) BiYIG021808 (post annealed in O ₂), (c) BiYIG072407 (in Ar) and, (d) BiYIG013108 (in Ar), all illuminated on the film side.	53
Fig. 3.19. Oxygen effect on Lattice mismatch-A statistical graph drawn for the films from set-1 and set-2	54
Fig. 3.20. SHG signal dependence on lattice mismatch strain (left graph), and micro-strain (right graph) of the annealed (close circles) and unannealed (open circles) film samples.	55
Fig. 3.21. Thickness Vs SHG graph drawn using samples from three different sets, diamonds in blue for PP geometry and square in pink for PS geometry.....	56
Fig. 3.22. SHG rotational anisotropy of (a) 2-layer, (b) 5-layer, (c) 10-layer, and (d) 15-layer garnet films.	57
Fig. 3.23. SHG rotational anisotropy measurements of a typical Bi:YIG sample (a) when sample is illuminated from film side, and (b) when sample is illuminated from substrate side.	58
Fig. 3.24. Plot of (a) Bi-concentration Vs LM strain, (b) Y-concentration Vs LM strain, (c) Bi-concentration Vs micro-strain, and (d) Y-concentration Vs micro-strain... ..	59
Fig. 3.25. Normalized SHG signal (PP geometry) dependence on (a) the lattice mismatch strain, and (b) the micro-strain. A second power allometric fit to LM strain dependence is plotted in (a) [105].	61
Fig. 3.26. Normalized SHG signal (PP geometry) dependence on (a) the Bi concentration, and (b) the Y concentration.	62
Fig. 3.27. Experimental Setup for HRS measurements	63

Fig. 3.28. HRS indicatrix of a film with a large lattice mismatch strain (a), narrow RS coherent peak indicate that the SHG signal is mostly coming from the surface/interface. Figure (b) depicts a broad HRS indicatrix for a LPE grown film with zero strain, showing that the film has a strong luminescence and there is no SHG signal.	64
Fig. 3.29. Surface patterning using photolithography and plasma etching techniques. ..	65
Fig. 3.30. SEM micro-graph of line patterns over Bi:YIG film.....	66
Fig. 4.1. Schematic representation of electronic BO motion in a crystal.....	69
Fig. 4.2. Dispersion curve for a particle in a periodic potential.....	71
Fig. 4.3. Schematic of a planar (slab) waveguide structure.	72
Fig. 4.4. Schematic of a ridge waveguide with air cover.	73
Fig. 4.5. Wave-vector representation, showing the wave-vector in longitudinal (k_z), and transverse (k_x) directions.....	74
Fig. 4.6. Calculated TE and TM modes for Ce:YIG/GGG slab structure. The graph shows that a micron thick film supports only one TE and one TM mode.	78
Fig. 4.7. Schematic demonstration of the nonreciprocity for TM waves.....	79
Fig. 4.8. Schematic of a ridge waveguide.	82
Fig. 4.9. Calculated $\Delta\beta = \frac{2\pi}{\lambda} \Delta n$ between FW and BW directions as a function of ridge-waveguide thickness. The figure displays plots for two substrate indices n_s (1.95, 2.25) and the same waveguide film index of 2.35. Note the shift in peak position and height with substrate index.....	84
Fig. 4.10. $\Delta\beta^{nr}$ as a function of silicon layer thickness in a Ce:YIG/SOI waveguide. In the graph diamond points are for ridge-waveguides and continuous curve is for corresponding planar waveguides. Graph indicates that the finite widths of the ridges have negligible effect on $\Delta\beta^{nr}$	84
Fig. 4.11. A ridge waveguide of Ce:YIG/Si/SiO ₂ (on left). $\Delta\beta^{nr}$ for slab and ridge structures are tabulated on right.....	85
Fig. 4.12. Schematic of a ridge waveguide array highlighting the mode index ramp of $\delta\beta$ between the adjacent waveguides.....	85
Fig. 4.13. Schematic depiction of the waveguide array highlighting the effective index progression between adjacent waveguides.	87
Fig. 4.14. Plot of nonreciprocal $\Delta\beta^{(nr)}$ versus normal mode β showing a nearly uniform $\Delta(\Delta\beta^{(nr)})$ between consecutive normal modes. The insets show the power distribution of the first normal mode of the array.	89
Fig. 4.15. BPM simulation results of (a) Bloch mode oscillations for the waveguide array with film index 2.35 and substrate index 2.25, showing a BO period of $\sim 945 \mu m$ for a $1 \mu m$ -wide input beam. (b) Simulated BO in FW, and (c) BW directions. The strength of $\Delta(\Delta\beta^{(nr)})$ has been artificially enhanced by a	

factor of twenty to highlight the difference in BO period shown with dashed lines.	91
Fig. 4.16. Schematic of Ce:YIG/SOI waveguide array, note that the widths are scaled up and separations scaled down four times to fit in the sketch.	93
Fig. 4.17. Plot showing nearly equally spaced NRPS $\Delta\beta^{nr}$ and propagation constant β for adjacent normal modes.	95
Fig. 4.18. (a) Beam evolution for single-guide excitation in the forward (FW) direction showing BO motion, (b) backward (BW) direction, showing diffractive beam spread. A 6- μm -wide beam excitation (c) in FW direction shows BO motion with the beam mostly confined to the high index side. (d) Diffractive beam spread in BW direction.	97
Fig. 4.19. (a) Bloch oscillator waveguide array (widths are scaled up and separations scaled down 4 times to fit in the sketch), (b) unidirectional BO based isolator design showing the BO array with damping channels on each side.	100
Fig. 4.20. Schematic showing working principle of the unidirectional BO based optical isolator.	102
Fig. 4.21. In the FW direction the beam returns to the central channel after travelling one Bloch period as shown by the intensity plot in (a), and the simulation plot in (c); in the BW direction a diffractive beam spread occurs with the beam reaching the damping channels as depicted by simulation plot in (b), and the corresponding intensity plot in (d). The intensity plots (a) and (d) show the slice output at the Bloch period (highlighted with square boxes in (c) and (b)) in FW and BW direction, respectively.	103
Fig. 4.22. Isolator schematic with modified damping channel design. This design gives isolation of ~ 55 dB.	104
Fig. 4.23. SEM image of a test structure fabricated in SOI via e-beam lithography for the design parameters simulated in Fig. 4.19(a).	105
Fig. 4.24. Schematic of a typical focused-ion-beam (FIB) column.	106
Fig. 4.25. Scanning-electron-micrographs of FIB-fabricated ridges of different heights in SOI.	107
Fig. 4.26. Atomic force microscope (AFM) image of the milled surface on Si (beam M0-50, beam current= 20 pAmp)	108
Fig. 4.27. Optical test results of a wide Si waveguide. Upper picture shows the end-fire coupling to the waveguide input. Lower picture is showing an optical mode of the waveguide.	109
Fig. A2.1. XRD diffraction patterns of a typical sample at five different angles (0, 45, 90, 135 and 180 degree).	130
Fig. A4.1. Intermediate terms in TM mode Eq. (4.27).	133
Fig. A6.1. Nonreciprocal delta beta calculation of Eq. (4.29).	137
Fig. A7.1. Page-1 of the derivation for the field dynamics in the coupled array structure Eq. (4.30).	138

Fig. A7.2. Page-2 of the derivation for the field dynamics in the coupled array structure Eq. (4.30).....	139
Fig. A7.3. Page-3 of the derivation for the field dynamics in the coupled array structure Eq. (4.30).....	140
Fig. A8.1. FDTD calculation.	141
Fig. A9.1. BPM simulation graphs showing FW and BW propagation of normal modes (supermodes) of the array structure. Note that normal modes maintain constant amplitude and width in FW direction, whereas they diffract out in BW direction.....	143

List of Tables

Table 2.1. YIG structural properties [43].....	11
Table 2.2. Effects of various parameters in LPE, PLD, and sputtering methods.....	17
Table 3.1. Analytical Parameters: RBS experiment.....	43
Table 3.2. Elemental concentrations and strain values of the Bi:YIG samples [105].....	47
Table 3.3. Analytical parameters: SHG experiment.....	48
Table A1.1. Bi:YIG films set-1 summary.....	125
Table A1.2. Bi:YIG films set-2 summary.....	126
Table A1.3. Bi:YIG films set-3 summary.....	127
Table A1.4. Bi:YIG films set-4 summary.....	128
Table A1.5. Bi:YIG films set-5 summary.....	129
Table A3.1. SHG results in PP geometry.....	131
Table A3.2. SHG results in PS geometry.....	132

Preface

The present dissertation is based on my PhD research work in Engineering Physics at the Michigan Technological University conducted during the period August 2007-January 2013. This preface serves as an explanation of my role in the work that comprises each of the chapters that make up the body of this dissertation.

The research studies conducted under this dissertation work include, in part, text and images published in the following four peer-reviewed journal articles.

1. **Pradeep Kumar**, A. I. Maydykovskiy, Miguel Levy, N. V. Dubrovina, O. A. Aktsipetrov, “Second harmonic generation study of internally-generated strain in bismuth-substituted iron garnet films,” *Optics Express* Vol. **18**, Issue 2, 1076-1084 (2010).
2. **Pradeep Kumar** and Miguel Levy, “On-chip optical isolation via unidirectional Bloch oscillations in a waveguide array,” *Optics Letters* Vol. **37**, Issue 18, 3762-3764 (2012).
3. **Pradeep Kumar** and Miguel Levy, “Unidirectional optical Bloch oscillations in asymmetric waveguide arrays,” *Optics Letters* Vol. **36**, Issue 22, 4359-4361 (2011).
4. Miguel Levy and **Pradeep Kumar**, “Nonreciprocal Bloch oscillations in magneto-optic waveguide arrays,” *Optics Letters* Vol. **35**, Issue 18, 3147-3149 (2010).

I (Pradeep Kumar) have coauthored all the four articles listed above published in the “*Optics Express*” and “*Optics Letters*” journals of the *Optical Society of America* (OSA). I have the necessary copyright permission from OSA (see Appendix 10) to reproduce, text and images, from the above listed journal articles in the present dissertation titled:

“NONLINEAR EFFECTS IN MAGNETIC GARNET FILMS AND NONRECIPROCAL OPTICAL BLOCH OSCILLATIONS IN WAVEGUIDE ARRAYS”

The work published in “*Optics Express*” (Publication 1) is the result of our collaboration with the research group of Professor Oleg Aktsipetrov at M.V. Lomonosov Moscow State University (MSU). All the thin film samples used in publication 1 were sputter deposited and characterized for crystallinity, strain, transmittance, thickness, refractive index and polarization rotation by myself together with Professor Miguel Levy

at Michigan Tech before being sent to MSU for second harmonic (SH) measurements. I travelled to Moscow, spent some time at MSU and took part in some of these measurements. Final data were analyzed by myself and Prof. Levy together with input from our collaborators (Prof. Oleg Aktsipetrov, Anton Maydykovskiy and Natasha Dubrovina) at MSU. Chapter 3 of this dissertation includes, in part, contents published in “*Optics Express*” (publication 1).

The work in Chapter 4 of the dissertation is based on the results published in three “*Optics Letters*” journal articles (publication 2 to publication 4). Chapter 4 addresses an important technological need, namely the development of on-chip optical isolator devices for optical communications and data processing. It is based on novel effects, namely, nonreciprocal and unidirectional optical Bloch oscillations recently proposed by Prof. Miguel Levy and theoretically demonstrated both by myself and Prof. Levy (see publications 2-4). My contributions include numerical calculations and simulations of a model system in a dielectric platform. Subsequently, together with Prof. Levy I extended the idea further and developed the concept of unidirectional Bloch oscillations in semiconductor substrates [see publications 2-4].

Chapter 1 and Chapter 2 do not include any collaborative or published work. Chapter 5 summarizes the important findings of this dissertation and provides directions for the future work.

The following article is not included in this dissertation.

1. R. El-Ganainy, **Pradeep Kumar**, and Miguel Levy, “On-chip optical isolation based on non-reciprocal resonant delocalization effects,” *Optics Letters* Vol. **38**, Issue 1, 61-63 (2013).

Acknowledgements

I would like to express my sincere gratitude to Professor Miguel Levy for giving me the opportunity to work in his supervision. I am thankful for his constant encouragement, guidance and support throughout my PhD research. I would like to thank Professor Levy sincerely and graciously for always being available and willing to help me whenever I needed it.

At the same time, it would have not been possible for me to come this far without the tremendous love and support from my dear parents and my brothers. I would like to thank all my family members for their moral support and encouragement throughout.

The best thing that happened to me during my PhD is that I met my other half - Neluka Dissanayake. As a colleague, she has always been there to help me in my research; as a wife, she is doing great to support me in all aspects of life. I should say thank you to my dear wife Neluka for all her help. I would like to thank my son Aryan for all the joy he brought to us.

My work would not be successful without the collaboration with the group of Professor Oleg Aktsipetrov at the Moscow State University (MSU). Special thank to Anton Maydykovskiy and Natasha Dubrovina for carrying out nonlinear optical measurements and fruitful discussions.

I would like to give my sincere thanks to Professor Tetsuya Mizumoto of the Tokyo Institute of Technology for collaborative experimental work in fabricating waveguide arrays. Thanks to Dr. Michael Steel, Dr. Vladimir Belotelov, Dr. Mathias Vanwolleghem, Dr. Ilya Vitebskiy, and Dr. Ramy El-Ganainy for their constructive feedback on the Bloch oscillation work.

I take this opportunity to acknowledge the help from my colleagues. Dr. Amir Jalali trained me in the sputter deposition technique. Dr. Raghav Vanga, Dr. Xiaoyue Huang, Dr. Ziyu Zhou, and Dr. Zhuoyuan Wu introduced me to various experimental methods at the beginning of my PhD career. Thanks to Jacob Ruben for helping me in developing a LabView program for an experiment. Thanks to Yong Meng Sua, Ashim Chakravarty,

and Ding Chu for their help while pursuing their own graduate studies.

I am grateful to Professor Ravindra Pandey, staff, and fellow graduate students in the Department of Physics. I would like to thank Owen Mills, and Ed Laitila from the Material Science and Engineering Department for their help on characterization equipment. Special thanks to William Knudsen, director of the Microfabrication facility, for his valuable time in training me on various fabrication tools and techniques.

Last but not the least I would like to thank Dr. Anand Kulkarni and my advisory committee members: Dr. Kim Fook Lee, Dr. Will Cantrell, and Dr. Durdu Guney for having spent time providing me with valuable suggestions in my dissertation work.

Abbreviations

AFM	Atomic Force Microscopy
BIG	Bismuth Iron Garnet ($\text{Bi}_3\text{Fe}_5\text{O}_{12}$)
Bi:YIG	Bismuth-substituted Yttrium Iron Garnet ($\text{Bi}_x\text{Y}_{3-x}\text{Fe}_5\text{O}_{12}$)
BO	Bloch Oscillation
BPM	Beam Propagation Method
BW	Backward
Ce:YIG	Cerium-substituted Yttrium Iron Garnet ($\text{Ce}_x\text{Y}_{3-x}\text{Fe}_5\text{O}_{12}$)
CMOS	Complementary metal-oxide-semiconductor
CVD	Chemical Vapor Deposition
Eq.	Equation
FIB	Focused-ion-beam
Fig.	Figure
FR	Faraday Rotation
FW	Forward
GGG	Gadolinium Gallium Garnet ($\text{Gd}_3\text{Ga}_5\text{O}_{12}$)
IR	Infrared
LPE	Liquid Phase Epitaxy
MO	Magneto-optical
NRPS	Nonreciprocal Phase Shift
PLD	Pulsed Laser Deposition
RBS	Rutherford Backscattering Spectrometry
RF	Radio Frequency
SEM	Scanning Electron Microscope
SHG	Second Harmonic Generation
SOI	Silicon-On-Insulator
XRD	X-Ray Diffraction
YIG	Yttrium Iron Garnet ($\text{Y}_3\text{Fe}_5\text{O}_{12}$)

Abstract

This dissertation presents detailed experimental and theoretical investigations of nonlinear and nonreciprocal effects in magnetic garnet films. The dissertation thus comprises two major sections. The first section concentrates on the study of a new class of nonlinear magneto-optic thin film materials possessing strong higher order magnetic susceptibility for nonlinear optical applications. The focus was on enlarging the nonlinear performance of ferrite garnet films by strain generation and compositional gradients in the sputter-deposition growth of these films. Under this project several bismuth-substituted yttrium iron garnet $(\text{Bi,Y})_3(\text{Fe,Ga})_5\text{O}_{12}$ (acronym as Bi:YIG) films have been sputter-deposited over gadolinium gallium garnet ($\text{Gd}_3\text{Ga}_5\text{O}_{12}$) substrates and characterized for their nonlinear optical response. One of the important findings of this work is that lattice mismatch strain drives the second harmonic (SH) signal in the Bi:YIG films, in agreement with theoretical predictions; whereas micro-strain was found not to correlate significantly with SH signal at the micro-strain levels present in these films. This study also elaborates on the role of the film's constitutive elements and their concentration gradients in nonlinear response of the films. Ultrahigh sensitivity delivered by second harmonic generation provides a new exciting tool for studying magnetized surfaces and buried interfaces, making this work important from both a fundamental and application point of view.

The second part of the dissertation addresses an important technological need; namely the development of an on-chip optical isolator for use in photonic integrated circuits. It is based on two related novel effects, nonreciprocal and unidirectional optical Bloch oscillations (BOs), recently proposed and developed by Professor Miguel Levy and myself. This dissertation work has established a comprehensive theoretical background for the implementation of these effects in magneto-optic waveguide arrays. The model systems we developed consist of photonic lattices in the form of one-dimensional waveguide arrays where an optical force is introduced into the array through geometrical design turning the beam sideways. Laterally displaced photons are periodically returned to a central guide by photonic crystal action. The effect leads to a novel oscillatory

optical phenomenon that can be magnetically controlled and rendered unidirectional. An on-chip optical isolator was designed based on the unidirectionality of the magneto-optic Bloch oscillatory motion. The proposed device delivers an isolation ratio as high as 36 dB that remains above 30 dB in a 0.7 nm wavelength bandwidth, at the telecommunication wavelength 1.55 μm . Slight modifications in isolator design allow one to achieve an even more impressive isolation ratio ~ 55 dB, but at the expense of smaller bandwidth. Moreover, the device allows multifunctionality, such as optical switching with a simultaneous isolation function, well suited for photonic integrated circuits.

1. Introduction

From its very inception, the field of material science and engineering has emerged as an imperative interdisciplinary field for its vital functions in all areas of applied science and engineering. The field involves synthesizing, processing, and characterizing different materials for specific purposes, varying from simple surface coatings to designing complex quantum bits. In the past few decades, thin-film materials possessing unique electric, magnetic, and optical properties have drawn special attention as they play a crucial role in developing advanced compact devices [1,2].

Thin films of various material types, i.e. metals, semiconductors, dielectrics and insulators, can be deposited on suitable substrates using physical or chemical vapor deposition techniques [2]. These films play a key role in advanced technological devices and common appliances, for example, magnetic storage devices, cell phones, solar panels, medical electronics, chemical sensors, photonics, and complex microelectronic devices [2,3]. Some of these applications are depicted in Fig. 1.1 below.

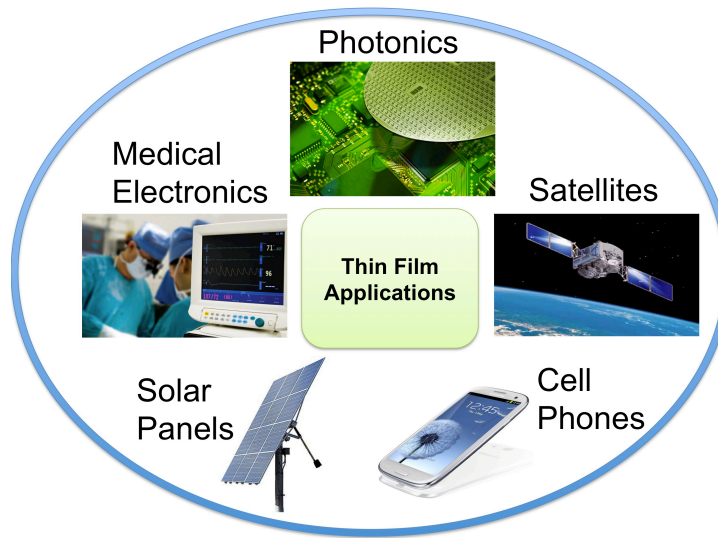


Fig. 1.1. Thin-film material based technological applications [4].

This dissertation encompasses important novel findings relating to nonlinear and magneto-optical properties of magnetic garnet thin films. Magnetic garnets are a well-

known group of materials currently used in various types of optoelectronic and nonreciprocal devices, such as optical isolators, switches, modulators and circulators [3]. The high applicability of magnetic garnets originates from their unique magneto-optical properties, which combine high Faraday rotation (FR) with low optical losses in the near-infrared (near-IR) spectral region, of high interest in optical communications [3]. At the same time, the technological parameters responsible for high nonlinear response in these materials are still not so well understood. This dissertation documents an exploration of key factors engendering nonlinear effects in magnetic garnet films, through rigorous experimental investigations. Besides the nonlinear study, the dissertation also includes a comprehensive analysis of novel nonreciprocal and unidirectional magneto-optical Bloch oscillation phenomena in asymmetric waveguide-array structures; first proposed and developed by Professor Miguel Levy and graduate student Pradeep Kumar [see publications section].

1.1. Literature review

The study of nonlinear optics forms an integral part of modern optics research. The field of nonlinear optics was known long before the invention of the laser. However lasers provided an incredible momentum to the field by allowing experimental observation of nonlinear effects in different material systems. In 1961, Peter Franken and coworkers reported the first experimental evidence of nonlinear optical effects in a quartz crystal using then newly developed laser system [5]. This pivotal event launched a golden era in optical physics. Thereafter, a tremendous progress in the field of nonlinear optics prevailed becoming possible with the advent of state-of-the-art high power laser systems [6-9].

Nonlinear optics provides new and complementary information compared to conventional linear optics, partly due to the different selection rules and higher-order optical susceptibilities involved [10]. Numerous nonlinear optical processes have been discovered since its first experimental observation in 1961 [5]; examples include harmonic generation, optical Kerr effects, multi-photon absorption, and four-wave mixing [11-15]. The lowest-order nonlinear process, namely, second harmonic

generation (SHG), plays an essential role in non-centrosymmetric materials i.e. materials lacking the inversion symmetry [10,16-17]. Therefore, observation of SHG in centrosymmetric materials requires broken inversion symmetry, making the study of strained epitaxial films of particular interest.

A number of publications have reported on the phenomenology of nonlinear effects in magnetic garnet films [10-12,18-20]. Gridnev et. al. presented a detailed theoretical treatment on their nonlinear behavior in [10]. Among the early-published experimental works, Aktsipetrov and coworkers, reported magnetic field induced SHG in liquid phase epitaxy (LPE) grown iron garnet films [12]. Lyubchanskii et. al. performed a detailed theoretical analysis on the influence of strain on SHG in magnetic garnet films [21,22]. In an experimental study, Pisarev et. al. pointed out that a symmetry lowering mechanism in epitaxial magnetic garnet thin films results from elastic deformations [23]. These authors further suggested that lattice imperfections and composition gradients are the key factors affecting the inversion centers in the film. Yet they note that more in-depth systematic studies of SHG in magnetic garnet films as a function of various strain components, strain gradients, film stoichiometry, composition gradient etc. are required. In the present work we address these concerns by inducing strain via lattice mismatch, and by the generation of compositional gradients in the bismuth component of the sputter deposited bismuth-yttrium iron garnet (Bi:YIG) films.

Beyond fundamental studies, this work is also very important from an applications point of view. The ultra-high sensitivity delivered by SHG is best suited for the exploration of magnetized surfaces and buried interfaces of metallic and non-metallic materials with a centrosymmetric structure; a task difficult to achieve with conventional techniques [11].

The second major study in the dissertation deals with the intriguing nonreciprocal and unidirectional optical Bloch oscillation effects [24,25]. Bloch oscillation (BO) is a remarkable phenomenon first predicted by F. Bloch and C. Zener in the 1930s, consisting of oscillatory motion for electrons subject to a constant electric field in a one-dimensional crystal [26,27]. In a theoretical treatment of the problem, Bloch and Zener proposed that electrons should exhibit a periodic oscillatory motion with period $T_B = h/(eEa)$, where e is electronic charge, E is the electric field amplitude, a is the lattice parameter, and h is the Planck constant, rather than uniform motion. However, this oscillatory motion of electrons had never been observed in natural crystals because the scattering time of the electrons by the crystal defects was much shorter than the Bloch period T_B [28].

The first experimental evidence of BO was reported in 1960 by Chynoweth et. al. in the form of an evenly spaced energy spectrum, called the Wannier-Stark ladder, for electrons in a crystal placed in a external electric field [29]. Thereafter, a number of studies exhibiting similar non-classical behavior in different particle systems, for example, electrons in semiconductor superlattices, cold atoms and Bose-Einstein condensates in optical lattices, and electromagnetic waves in periodic dielectric structures, have been reported [30-34]. Optical analogues of electronic Bloch oscillations have been also observed, as spatial beam oscillations using periodic-discrete-optical systems exhibiting diffraction-less propagation of an optical beam [35,36]. As an example of particular relevance, photons in an array of evanescently coupled waveguides with a transverse effective refractive index ramp have been shown to perform a periodic oscillatory motion with controlled beam dynamics [33,35-38].

In optical systems, the modal refractive index in waveguides plays the role of atomic potential in the crystal, whereas the external electric field is replicated through a constant waveguide-mode index ramp achieved by either through a systematic modification in waveguide dimensions or by applying a temperature gradient [33,35,36]. Although the phenomenon has been studied in reciprocal optical system in recent years [33,35-38], nonreciprocal BO effects have not been demonstrated yet.

In the present work we utilize the nonreciprocal phase shift effect, a characteristic property of the magnetic garnets, to analytically demonstrate a new type of optical Bloch oscillation phenomenon exhibiting different Bloch period in the forward and backward directions of propagation. Nonreciprocity into the array structure is introduced by imposing unequal vertical refractive index gradients at the substrate/core, and core/cover interfaces in the presence of transverse magnetization. We conduct a detailed study on two types of structures: magnetic-iron-garnet core ridge waveguides with air covers, and silicon ridge waveguides with sputter-deposited magnetic-iron-garnet covers.

As industrial device requirements become increasingly more stringent and loss-intolerant, the need for alternative approaches to serial integration becomes imperative [39-41]. Furthermore, essential components such as optical isolators are still missing from the integrated circuits. In the present work, we show that the unidirectionality of the Bloch oscillatory phenomenon can be used for on-chip optical isolation purposes. Isolators are critical components that protect signal stability in optical circuits by blocking out back-reflected light. At the same time, through the unidirectional Bloch oscillation effect, the same isolator device can perform as a fast optical switch via magnetization reversal, turning off the forward beam. Routing, a critical function in signal processing, can be performed by adjusting lateral beam spread through electro-optic control. The output of the present dissertation work has the potential to strongly impact telecommunications and data processing by enabling compact integration, fast switching and insertion loss minimization. Moreover, by overcoming serial integration it takes an important step towards cost reductions in photonic circuit technology.

1.2. Dissertation outline

The dissertation consists of two major sections. In first section we establish a relation between the crystallographic properties and SHG signal in bismuth-substituted yttrium iron garnet $(\text{Bi,Y})_3(\text{Fe,Ga})_5\text{O}_{12}$ (Bi:YIG) films, based on experimental findings. This work includes the fabrication, and the structural, optical, and nonlinear-optical characterization of magnetic garnet films. The focus was on enlarging the nonlinear

performance of Bi:YIG films by strain generation, and by compositional gradients in the sputter-deposition growth of these films.

In the second section of the dissertation, we present the novel nonreciprocal and unidirectional optical Bloch oscillation effects, recently proposed and developed by us [24,25]. We present a comprehensive theoretical basis for the implementation of nonreciprocal and unidirectional optical Bloch oscillations. We design and simulate a waveguide-array based optical isolator, a technologically important component in photonic integrated circuits [42].

The rest of the dissertation is organized as follows.

- Chapter two develops a theoretical background on magnetic garnet thin films, and their structural, optical and magneto-optical properties, which provides a foundation for the studies discussed throughout the dissertation.
- Chapter three describes an in-depth experimental study of the crystallographic origin of nonlinear effects in epitaxially grown Bi:YIG films.
- Chapter four reports on novel nonreciprocal and unidirectional optical BO phenomena in magneto-optic waveguide arrays. Besides the analytical treatment of the problem, application to on-chip isolation and multi-functionality are discussed.
- Chapter five concludes the dissertation and proposes new directions for the future of this research.

2. Magnetic Garnets: Properties and Applications

Over the last few decades, magnetic garnets have been the subject of both fundamental and application-oriented research [43-46]. The active interest in optical, magneto-optical, and structural properties of these materials is related to the fact that their properties can be varied by a number of substitutions, and by changes in the composition and the orientation of the substrate [43]. Considering the importance of garnet materials in the field of magneto-optics, it is surely worth to provide an overview of their structural and optical properties in this early chapter of the dissertation. The contents of the chapter are intended to set the groundwork for the remainder of the dissertation, which include novel findings based on optical and magneto-optical properties of iron garnet films.

The opening section gives a brief summary on different types of magnetism, which is then followed by a detailed description of this versatile class of garnets.

2.1. Types of magnetism in magnetic materials

Magnetic materials are composed of tiny magnets that possess finite dipole moments called magnetic domains. Based on the magnitude and direction of the magnetic domains, these materials are primarily categorized in four categories: paramagnets, ferromagnets, antiferromagnets, and ferrimagnets. The following paragraphs provide a quick overview on the characteristic ordering in magnetic materials [47].

- **Paramagnetism**

This class of magnetic materials, known as paramagnets, tends to have randomly oriented dipole moments due to thermal fluctuations in the absence of an external magnetic field; see Fig. 2.1 (a). When a magnetic field is applied, the dipole moments start aligning along the field direction such that the induced magnetization in the material is proportional to the applied field strength at low magnetic fields. Examples of paramagnetic elements include magnesium, molybdenum, and lithium.

- **Ferromagnetism**

Ferromagnetic elements, such as Cobalt (Co) and iron (Fe), comprise domains that have the tendency to have their net magnetic moments become aligned parallel to each other under the influence of an external magnetic field. However, unlike paramagnets, ferromagnetic domain magnetic moments will persist even when the field is removed, as shown in Fig. 2.1 (b).

- **Antiferromagnetism**

In this type of magnetic ordering, adjacent magnetic moments tend to align anti-parallel to each other in the absence of an applied field. In general, adjacent magnetic moments are equal in magnitude and opposite in direction, resulting in a net zero magnetization as shown in Fig. 2.1 (c). Antiferromagnetism vanishes above a certain temperature, called the Néel temperature. After the Néel temperature, the material acquires paramagnetism. Chromium is an example of an antiferromagnetic element.

- **Ferrimagnetism**

Ferrimagnets exhibit the phenomenon of ferrimagnetism, in which the aligned magnetic moments are antiparallel in neighboring sublattices having unequal magnitude as shown in Fig. 2.1 (d). Therefore, a non-zero spontaneous magnetization occurs in ferrimagnetic materials. The well-known examples of ferrimagnetic materials are ferrites and magnetic iron garnets.

Garnets represent a much broader class of materials exhibiting antiferromagnetism, weak ferromagnetism, and ferrimagnetism [43,47]. This chapter aims at summarizing the important material and optical properties in ferrimagnetic ion garnets, with a particular emphasis on bismuth-substituted and cerium-substituted yttrium iron garnet (Bi-, Ce-YIG).

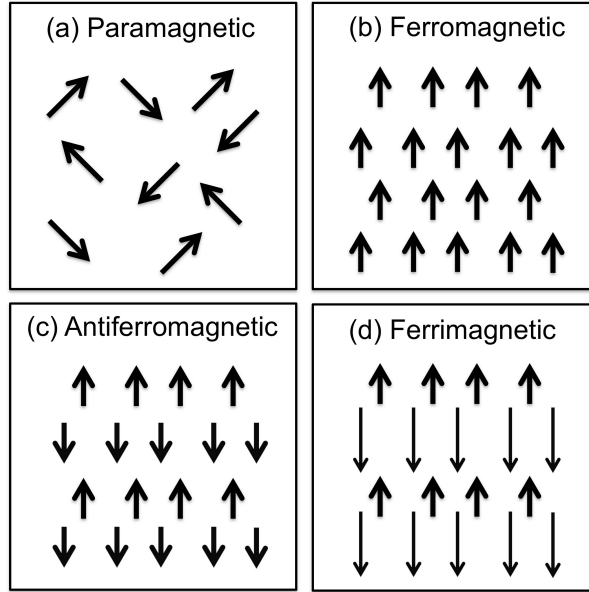


Fig. 2.1. Ordering of magnetic dipole moments in magnetic materials.

2.2. Garnet crystal structure

Garnets are a well-known group of materials represented by the following prototypic chemical formula: $\{C^{3+}\}_3[A^{3+}]_2(D^{3+})_3O_{12}$, where C, A, D stands for the ions that occupy different sublattices in the structure [43]. Ideally, a garnet structure is cubic in symmetry and belongs to centrosymmetric space group $Ia\bar{3}d$ (O_h^{10}). The unit cell of the garnet crystal contains 8-formula-units with a total of 160 ions at four different sites. Of the 160 ions, 24 ions occupy the tetrahedral (d) sites, 16 ions occupy the octahedral [a] sites, 24 ions occupy the dodecahedral {c} sites, and 96 oxygen ions surround the three sublattices with the coordination number 4, 6, and 8, respectively. The three sublattice positions (i.e. {c}, [a], and (d)) lack any degree of freedom, whereas the O_2 occupying the h -positions have three degrees of freedom (see Fig. 2.2 for an example).

Prior investigations in iron garnets have shown that the unequal dipole moment contribution from their constituting sublattices result in their ferrimagnetic character [43,47]. The sublattice magnetizations play a crucial role in determining the saturation magnetization of the garnet structure, and generally, the temperature-dependent

saturation magnetization $M_s(T)$ is calculated by a vector sum of sublattice contributions, as given in Equation (2.1).

$$M_s(T) = |M_d(T) + M_c(T) - M_a(T)| \quad (2.1)$$

Where $M_d(T)$, $M_c(T)$, and $M_a(T)$ denote the saturation magnetizations of tetrahedral, dodecahedral, and octahedral sites, respectively. The saturation magnetization varies with temperature, decreasing to zero at the Curie temperature (T_c).

2.2.1. YIG structure

Yttrium iron garnet (YIG) $\{Y^{3+}\}_3[Fe^{3+}]_2(Fe^{3+})_3O_{12}$ is the most thoroughly studied ferrimagnetic garnet material due to its various applications in microwave communication and optical devices [43-46,48]. For example, in an optical isolator, a YIG crystal is used as a Faraday rotator, which protects a laser source from the unwanted back-reflections. A single crystal of YIG shows a significant magneto-optical effect, i.e. the Faraday rotation (FR), which spans the visible and near-IR spectral regimes, making it a suitable FR material. The FR, optical absorption, and refractive index values of YIG are 214 Degree/cm, 0.05 cm^{-1} , and 2.2, respectively, measured at the telecommunication wavelength 1310 nm [49].

The ionic arrangement in the unit cell of a YIG crystal is shown in Fig. 2.2, and its structural properties are summarized in Table 2.1. The unit cell is comprised of 24 Fe^{3+} ions at the tetragonal (d) sites, 16 Fe^{3+} ions at the octahedral [a] sites, 24 Y^{3+} at the dodecahedral {c} sites, and 96 O_2 ions surrounding the three sublattices. A closer look at the YIG structure reveals that Fe^{3+} ions occupy octahedral and tetrahedral sites and possess antiparallel and unequal magnetic moments resulting in a net magnetization along the tetrahedral direction.

The average lattice parameter of YIG structure is approximately 12.38 Å, which is very large in comparison to other materials [43]. The large and open structure of YIG allows one to prepare advantageous derivatives through substitution processes. Besides YIG, companion structures prepared by various substitutions in the lattice also play vital roles in advanced technological applications, e.g. optical isolators, magnetic switches,

and chemical sensors [43-46,50-54]. In particular, bismuth and cerium are the two most successful substitutions that enhance the figure of merit of the parent YIG structure [52-55]. We provide some more details on Bi:YIG and Ce:YIG structures in the following subsections.

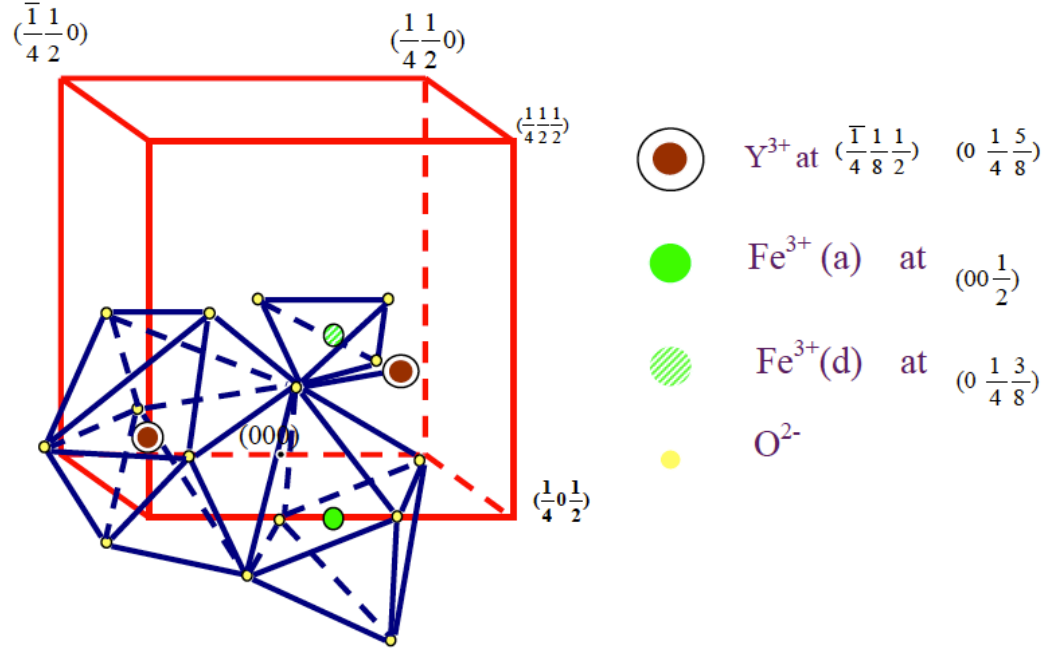


Fig. 2.2. An illustration of the yttrium iron garnet (YIG) lattice structure, highlighting the ionic arrangement in a unit cell [56].

Table 2.1. YIG structural properties [43].

Space Group Position	24c	16a	24d	96h
Typical ideal formula	$\{Y_3\}$	$[Fe_2]$	(Fe_3)	O_{12}
Coordination to O_2	8	6	4	
Type of polyhedron	dodecahedron	octahedron	tetrahedron	

2.2.2. Bi-substituted YIG

Elemental-substitutions in the YIG crystal have a huge impact on its crystalline, optical, and magneto-optical properties [43,57]. A leading example is bismuth-substituted YIG (Bi:YIG), which exhibits a remarkable improvement in the magneto-optic properties of the original YIG structure. The reported highest FR of completely substituted bismuth iron garnet (BIG) is 4300 degree/cm, and its refractive index is 2.548 at the telecommunication wavelength 1550 nm [58,59], the wavelength where the fiber optic communication system is developed. A vast amount of theoretical studies have attempted to elucidate the origin of the giant magneto-optic (MO) effect in Bi:YIG materials [43,57,60-63]. In a widely accepted theory, the large MO effect is predicted to originate from the splitting of the excited states of the Fe^{3+} ions due to the enhanced spin-orbit interaction in Bi:YIG structure [63].

Applications of crystalline thin films of magnetic iron garnets were realized as early as the 1970's [43]. Since then, their use has been spread to large variety of magnetic and optical devices such as magnetic memory, display, data processing and optical communications [50-54,64,65]. In the wide class of magnetic garnets, Bi:YIG is one of the most comprehensively studied and widely used material. A large volume of literature exists which reports on various intriguing properties of Bi:YIG and its specific applications in modern-day devices [60-65]. Some interesting applications of magnetic garnet films are presented in section (2.5).

Nonlinear effects in anisotropic magnetic garnet films were reported in 2001 by Gridnev *et. al* [10]. These authors have shown that in addition to non-cubic deformations of the crystal structure in epitaxial garnet films, space-inversion symmetry can be broken as well in anisotropic magnetic films. However, the symmetry breaking mechanism responsible for second harmonic generation (SHG) has not been studied in detail in these films. Little information of the crystallographic origin of SHG is available. In the present dissertation, we address this issue with the help of a systematic experimental investigations of nonlinear effects in sputter deposited Bi:YIG films (see chapter 3).

2.2.3. Ce-substituted YIG

In 1985, Leycuras et. al. reported that the inclusion of cerium in YIG (Ce:YIG) single crystals induce large Faraday rotations [66]. Subsequently, in an experimental study, Gomi et. al. found a five-times stronger FR in sputter deposited Ce:YIG compared to Bi:YIG in the near-IR optical regime [55]. The reported highest FR of Ce:YIG is 4800 degree/cm, and its refractive index is 2.22 at the telecommunication wavelength 1550 nm [67]. A drawback of cerium-substitution is that it causes high optical losses. Nevertheless, the quality factor for Ce:YIG films, Faraday rotation per damping, is still better than the competing Bi:YIG films [68].

There is abundant theoretical and empirical literature suggesting that Ce:YIG is one of the best material for developing high performance nonreciprocal devices, such as optical circulators, isolators, etc. [51,55,68]. In this dissertation work, we make use of the large magneto-optic effect offered by Ce:YIG in designing an on-chip optical isolator, a technologically important component in photonic integrated circuits (PIC) (see chapter 4).

2.3. Thin film fabrication and characterization techniques

The ever-increasing need to develop highly integrated electronic and optical devices rely largely on innovative thin-film technologies. For example, to realize an on-chip optical isolator, a magnetic garnet thin film with appropriate Faraday rotation must be deposited on a substrate. The garnets are usually grown with different techniques on matching substrates. This section of the chapter will provide an overview on the thin film deposition processes.

At present a number of well-established film growth techniques are in use. These can be broadly classified into two groups:

I. Physical vapor deposition (PVD)

This can be either evaporation- or a sputter-deposition-process. The two processes are purely physical in the sense that they involve either a high

temperature vacuum evaporation with subsequent condensation (i.e. evaporation method) or plasma sputter bombardment of the substrate to be coated (i.e. sputter method). Typical steps in a PVD process are shown in Fig. 2.3 (a).

II. Chemical vapor deposition (CVD)

This process involves inclusion of specific reactive-gas species into a vacuum chamber containing a heated substrate to be coated. The chemical reaction occurs on and around the heated substrate, resulting in a thin film deposition on the substrate. Typical steps in a CVD process are shown in Fig. 2.3 (b).

Both PVD and CVD processes are extensively used in research laboratories and in the semiconductor industry to produce high quality thin films of a wide range of materials. As we are only concerned with sputter deposition technique, we will restrict this discussion to physical processes, with a particular emphasis on sputter deposition technique.

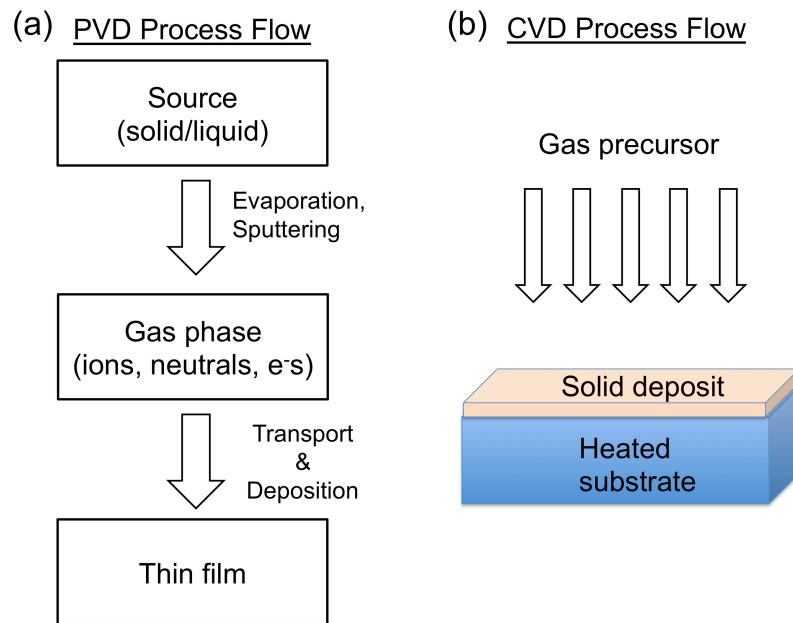


Fig. 2.3. Schematics showing typical steps in a, (a) physical vapor deposition (PVD) process, and (b) chemical vapor deposition (CVD) process.

Three major film-growth processes are liquid phase epitaxy (LPE), pulsed laser deposition (PLD), and sputtering. These processes are briefly summarized in the following subsections.

2.3.1. Liquid phase epitaxy (LPE)

The LPE technique is commonly employed to grow semiconductor and garnet crystal layers from their melt. To grow magnetic garnet films, a single crystal of garnet substrate is dipped into the undercooled solution and rotated at a predetermined speed (see Fig. 2.4). After the process is complete, the film is pulled out to just above the melt and rotated again to remove the excess melt. The rotation speed and undercooling conditions give control over film thickness and film stoichiometry, respectively. The process can occur at temperatures well below the melting point of the deposited material.

Reportedly, LPE is the only commercially available technique to fabricate high quality mono-crystal films for use in film-based Faraday rotators [69]. Some drawbacks of the LPE method include: poor control over film thickness, requirement of lattice-matched substrate, and high optical absorption in the deposited film due the presence of lead (lead oxide is typically used in LPE melt). Usually, the LPE method is preferred for growing film with thicknesses $\geq 1 \mu\text{m}$.

2.3.2. Pulsed laser deposition (PLD)

The PLD process uses an intense laser beam to ablate the target material. In a typical laser ablation process, material from a solid target is removed through an energy transfer method. The ablated material forms a plasma plume and a thin film is deposited on a substrate placed inside the vacuum chamber (see Fig. 2.5). The PLD process generates congruent evaporation, which is a nonequilibrium process. Therefore, the technique allows achievement of complete Bi substitution in a YIG crystal (BIG) [59]. The major drawbacks of the PLD method include rough surfaces and structural inhomogeneity in the films [70].

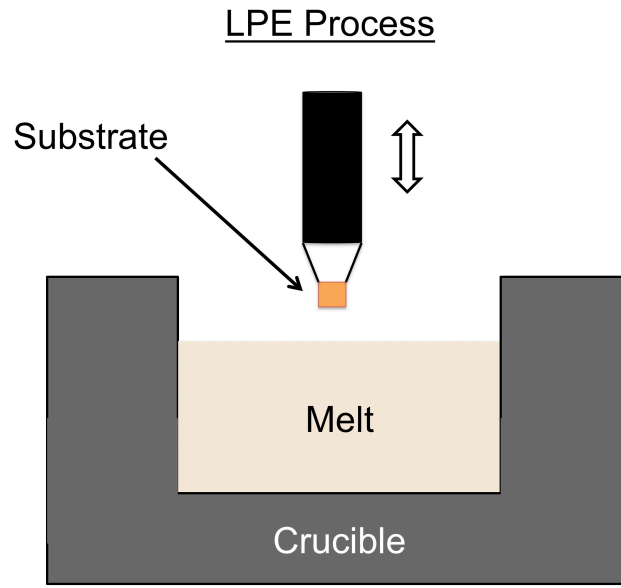


Fig. 2.4. Liquid phase epitaxy (LPE) set-up.

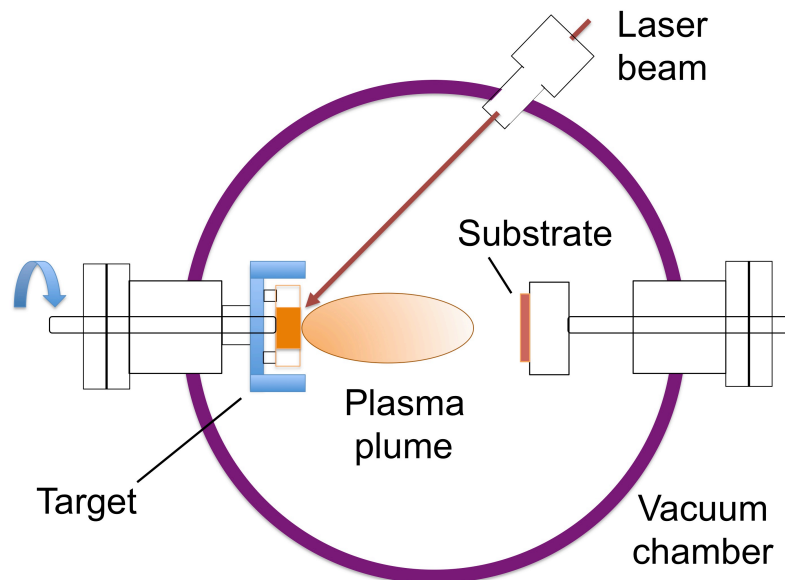


Fig. 2.5. Schematic view of a PLD-system.

2.3.3. Sputtering

Sputtering is a widely used technique for depositing thin films of a wide range of materials. It is a physical process; in which energetic ionic species (e.g. Ar^+) hit the

target and knockout material from the surface layer through a momentum transfer process. The sputtered atoms then deposit on a substrate placed inside a high vacuum chamber.

Sputtering is the primary technique for metal deposition in modern silicon-based technologies and is widely used in other thin film depositions. All three major film-growth methods (LPE, PLD, and sputtering) can be used to prepare epitaxial thin films of magnetic garnets. A comparative study of the influence of different parameters in PVD processes is given in Table 2.2.

Table 2.2. Effects of various parameters in LPE, PLD, and sputtering methods.

	LPE	PLD	Sputtering
<u>Bi-Substitution</u>	Yes (limited to low substitution)	Yes -	Yes (complete substitution possible)
<u>Lattice Matching</u>	Required	Not required	Not required
<u>Thickness Control</u>	Coarse	Coarse	Fine
<u>Crystalline Quality</u>	Very high	High	High
<u>Multilayer Film</u>	Difficult	Easy	Easy

The three basic variants of a sputter-deposition system are [71]:

- (i) DC (or diode) sputtering: -

This represents the simplest version of the sputter deposition technique. In DC configuration a target, made of a material to be deposited, is placed on the cathode, and a substrate is placed on the anode. A negative voltage of about -2 kV to -5 kV is applied across the two electrodes resulting in ionization of the working gas (e.g. Argon) atoms. The positive ions thus created are accelerated

towards the negatively biased cathode. When the positive ions collide with the cathode (target), the kinetic energy transferred is sufficient to eject atoms of the surface layer of the target. Before the process starts chamber is evacuated to high vacuum $\sim 10^{-6} - 10^{-7}$ Torr. During the sputtering process, the chamber pressure is normally about $10^{-3} - 10^{-2}$ Torr. Argon is very often used as the working gas, as it is coast-effective and provides sufficient momentum for sputtering a very wide range of materials. Schematic illustration of a DC sputtering system is shown in Fig. 2.6.

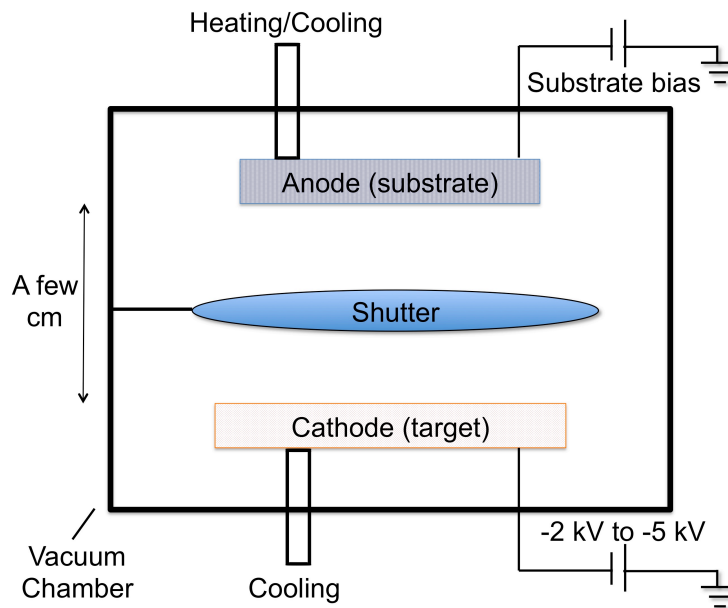


Fig. 2.6. Schematic view of a DC sputtering system.

(ii) RF (radio-frequency) sputtering: -

Here the basic principle is the same as for DC sputtering, however this design is preferred when sputtering from insulating target materials. The polarities of the electrodes are varied at a radio frequency (normally 13.56 MHz) to avoid charge build-up when sputtering insulating materials such as PZT, and magnetic garnets. Schematic illustration of a RF sputtering system is shown in Fig. 2.7.

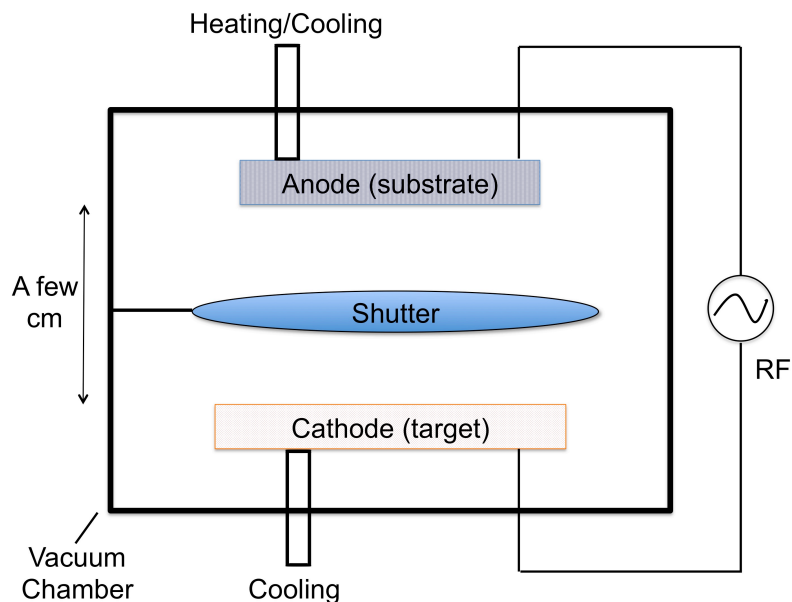


Fig. 2.7. Schematic view of a RF sputtering system. Here a RF generator (13.56 MHz) with a matching network is used; this allows sputtering of the insulating materials.

(iii) Magnetron-sputtering

In this special configuration, a magnetic trap is used to enhance the sputtering rate, by confining the charge particles near the target surface. Use of magnets around the target not only allows confining the electrons, but also the charged species at the target, to prevent re-sputtering on the substrate. For the present dissertation work, we used an in-house RF magnetron sputtering system to grow strained Bi:YIG films. The RF sputter deposition technique allows the incorporation of Bi and the generation of strain gradients. A detailed description of the RF magnetron system used for the present is given in chapter 3.

2.3.4. Film characterization

In this section, we list some common techniques employed for characterization of magnetic garnet thin film structures:

- Crystallinity: - An x-ray diffraction (XRD) technique can be used to find the crystalline quality of thin film structures.

- Surface morphology: - An atomic force microscope (AFM) is usually employed to access the film's surface quality, such as surface roughness and inhomogeneity. In addition, a scanning electron microscope (SEM) allows one to take high quality pictures with submicron details of various film structures (e.g. waveguides, photonic crystals, microcavities, etc.).
- Thickness and refractive index measurement: - A prism coupler or an ellipsometer can be used to get information on a film's thickness and refractive (material) index. An ellipsometer is a versatile tool capable of providing high accuracy and precision measurements in a wide spectral range (193 nm to 3200 nm) [72]. Moreover, variable wavelength and angle of incidence allow flexible measurement of a number of parameters, such as reflectance, transmittance, and general ellipsometry.
- Film composition: - Several techniques are available to measure a film's elemental composition. These techniques include Rutherford backscattering spectrometry (RBS), x-ray photoelectron spectroscopy (XPS), and electron probe microanalysis (EPMA). In this dissertation, stoichiometric compositions of sputtered Bi:YIG samples were analyzed by the RBS technique (for details see chapter 3).
- Magnetic properties: A vibrating sample magnetometer (VSM) is commonly used to measure magnetic properties of a wide range of materials. The working principle of VSM is based on Faraday's law of induction, which tells that a changing magnetic field will produce an electric field.

A detailed description of film characterization methods used in this dissertation work is available in chapter 3.

2.4. Magnetic garnet thin-film-based applications

Since its inception, magnetic garnet films have stimulated research in a number of areas. These areas include data storage, magneto-optic imaging, integrated nonreciprocal devices and photonic crystal technology [68,69,73-75]. Magneto-optical imaging devices

allow one to perform real-time detection of two-dimensional magnetic patterns such as magnetic flux in superconductors, magnetic tracks on audiotapes and videotapes, and small currents in microelectronic circuits [76-78]. Recently developed magnetic garnet based optical sensors provide electromagnetic interference free sensing with an excellent signal to noise ratio and frequency response [79].

Over the years, researchers at the integrated photonics laboratory at Michigan Tech led by Professor Miguel Levy have been involved in pioneering work in developing magnetic garnet thin films and photonic crystals for novel applications. Recently, some innovative device applications were reported by the Levy group. Fig. 2.8 shows a gyrotropic photonic crystal waveguide switch [52]; and Fig. 2.9 shows a magneto-photonic crystal chemical sensor [73]. Waveguide-based magneto-optic switches and sensors are indispensable components in integrated photonic circuit technology.

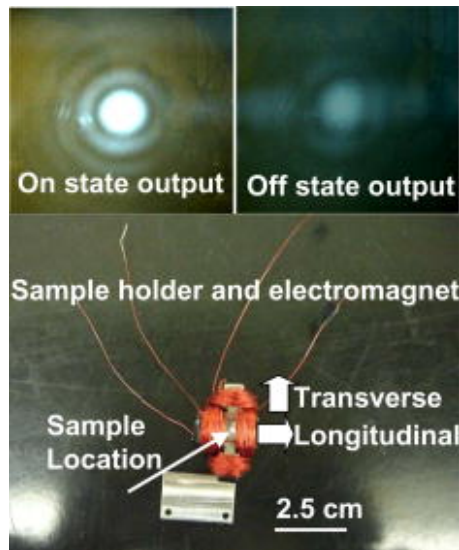


Fig. 2.8. A picture showing a prototype photonic crystal waveguide switch device developed by Levy and coworkers [52].

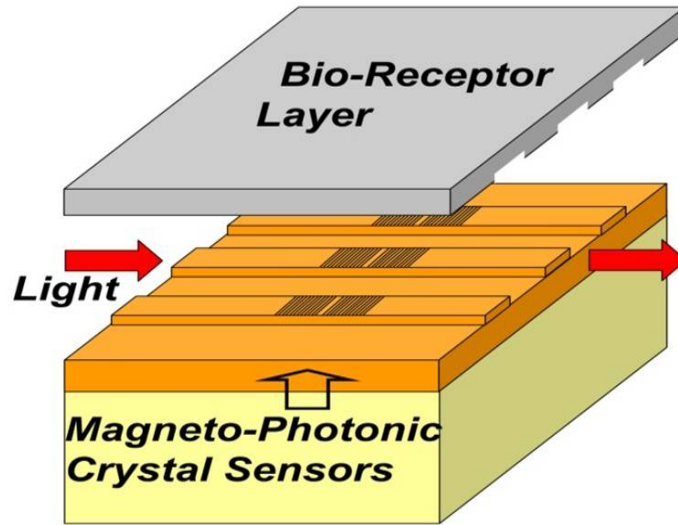


Fig. 2.9. Schematic view of a magneto-photonic crystal chemical sensor developed by Levy and coworkers [73].

2.5. Garnet-semiconductor integration: issues and solutions

Over the last few years, design and fabrication of on-chip optoelectronic components have gained popularity due to their promising role in implementation of highly integrated devices [39-41]. The key components of an optoelectronic circuit can be realized on Si and III-V compound semiconductor substrates. Interestingly, a crucial element, namely, an optical isolator, is still missing from CMOS compatible platforms. An optical isolator acts like an optical diode and allows only one-way propagation of the light beam, thereby providing stability to the laser sources. Commercial grade optical isolators, which rely on bulk optics, are available from a long time now. However, these isolators are not suitable for on-chip integration with other devices. Therefore, waveguide based optical isolator must be developed for the integrated optical circuits [80].

The large Verdet constant, large Faraday rotation, transparency in the near infrared range and ability to control the room temperature ferrimagnetism render magnetic iron garnet films as good candidates for designing waveguide isolators [43,68]. However, integration of such devices on technologically important semiconductor platforms has been a challenging task due to material incompatibilities and large device footprint [39]. A

severe integration problem is encountered due to the large differences in the material indices and lattice constants of garnet and semiconductor materials. The average lattice parameter of Bi:YIG crystal structure normally fall in the range of 12.4 Å to 12.6 Å [39], which is relatively larger than the commonly used semiconductor materials, such as Si and GaAs which have lattice parameters of 5.4307 Å and 5.65325 Å, respectively [81]. Fig. 2.10 shows a schematic that highlights the lattice mismatch at the garnet-silicon interface layer, a major reason for poor bonding between the two materials. The large discrepancies in refractive indices, thermal expansion coefficients, and lattice constants of garnet and semiconductor materials make it difficult to grow epitaxial films of one material over the other. At the same time, a garnet/silicon combination offers significantly large nonreciprocal phase shift effect due to the large index contrast involved [82].

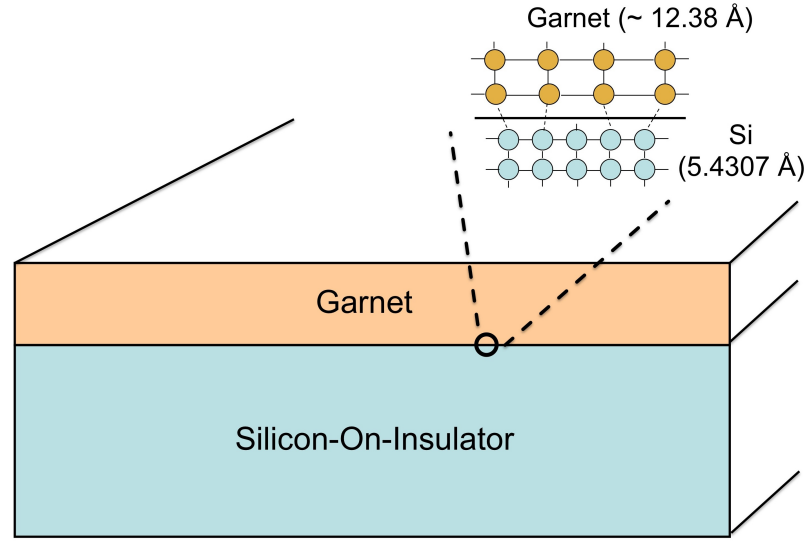


Fig. 2.10. A schematic, showing the cross-sectional view of a SOI substrate with a garnet cover layer. Inset is highlighting the lattice mismatch at the interface layer. Typical lattice constants of the materials are given in the brackets.

Silicon-on-insulator (SOI) platforms are well known for their vital role in silicon-based technology. Recent works in the field have revealed promising garnet-semiconductor hybrid structures comprising SOI substrates with magnetic garnet cover layer [83,84]. The pioneering works of Mizumoto and coworkers have established a

surface activated direct wafer bonding technique, which allows fabricating hybrid structures of garnet-semiconductor materials [85]. Their technique of direct surface bonding has the potential advantage that dissimilar materials are bonded at low temperature, which allows overcoming the issue related with the difference in thermal expansion coefficients. These authors have successfully demonstrated bonding between magnetic iron garnet film and silicon. The surface layers of the two wafers (e.g. Si and Ce:YIG) are activated via an oxygen plasma in a vacuum chamber, and then the wafers are pressed against each other at elevated temperatures, as shown in Fig. 2.11.

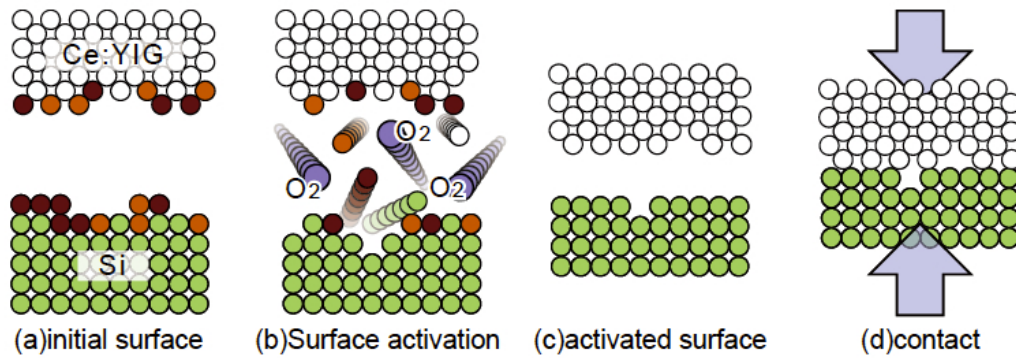


Fig. 2.11. Schematic of surface activated direct wafer bonding technique [85].

In a recent work, Ross and coworkers developed a monolithically integrated on-chip optical isolator in garnet/SOI hybrid materials system [84]. In their proposed prototype device, two layers of magnetic garnets were deposited on a silicon platform using a PLD system. The garnet/SOI structure was achieved using a two-step deposition method; first a thin YIG layer was deposited on Si and then a Bi:YIG (or Ce:YIG) layer was deposited on the YIG buffer layer.

The above-mentioned experimental demonstrations are very encouraging, and pave the path for future research activity on garnet/semiconductor materials. In the novel findings of the unidirectional Bloch oscillation (BO) effect and the related on-chip optical isolation function, we have used a model waveguide array structure in Ce:YIG/SOI material system (see chapter 4 and 5). The Ce:YIG/SOI combination offers a very large nonreciprocal phase shift effect best suited for designing an on-chip isolator.

3. Second Harmonic Generation in Bi:YIG Films*

3.1. Aim and motivation

This work is intended to fill a need for a deeper understanding of nonlinear effects in magnetic garnet systems because of the important connection of magnetic systems to applications in magnetic recording and memory storage [11,54]. The aim of this project is to examine nonlinear phenomena in magneto-optic systems and to establish the feasibility of harmonic generation as a tool for sub-micron magnetic surface/interface analysis by conducting a systematic study of stress/strain, composition, and surface/interface effects on second harmonic generation (SHG) in magnetic garnet thin films.

Besides a fundamental investigation of the surfaces and interfaces of the optical materials, the current study is also important from an applications point of view. A potential high-impact application of magnetization-induced SHG in magnetic materials is high spatial-resolution determination of magnetic symmetry [86,87]. Ultra high sensitivity delivered by SHG is increasingly being recognized as a versatile tool for the exploration of magnetized surfaces and buried interfaces of metallic and non-metallic materials with a centrosymmetric structure [11]. Moreover, SHG has been suggested as a nonlinear-optical nondestructive readout in thin-film-based optical memories [88].

One particularly important subject matter, although understudied in the literature, is the crystallographic origin of nonlinear response in magnetic garnet thin films. An epitaxially grown strained magnetic garnet film loses its centrosymmetric structure due to the missing inversion centers, which are largely confined in the vicinity of the interface layer in the film. Past investigations on the subject have been confined to theoretical analysis [11,89,90]. Thus, there is a great need for experimental evidence to support these theoretical works.

* The material contained in this chapter has been published in the *Optics Express* Vol. **18**(2), 1076-1084 (2010). For detailed citation, see reference [105].

Here, we present an in-depth study of the influence of crystallographic parameters such as strain components, stoichiometry composition, and composition gradients, on the SHG response of sputter-deposited magnetic garnet thin films. Our work includes a comprehensive experimental investigation systematically conducted over a period of three years. This investigation constitutes a collaborative effort with the research group of Professor Oleg Aktsipetrov of the Moscow State University (MSU). Important results of the study are in good agreement with the theoretical predictions previously formulated by Lyubchanskii and coworkers [21,22].

The remainder of the chapter contains a theoretical background, which gives an insight into theoretical aspects of the nonlinear effects in general, and in thin-film materials. This is followed by an experimental section, which presents a detailed examination of different experimental setups, film growth processes, and several characterization and measurement techniques to evaluate the films' properties. And finally, in the results and discussions section of the chapter, a thorough discussion on important findings and observations of this project is provided.

3.2. Theoretical background

3.2.1. The nonlinear susceptibility

The invention of the laser revolutionized the field of nonlinear optics. Generally, in low field-intensities (i.e. the optical field from conventional sources), a medium exhibits linear behavior that indicates the optical susceptibility (χ) and the dielectric constant (ϵ) of the medium are field-independent. However, when the field is not weak (i.e. the optical field from high power laser sources) both (χ) and (ϵ) can become functions of the electric field (E), resulting in nonlinear behavior of the medium [91]. As the optical field intensity increases, the nonlinear effects become more and more important, leading to a number of higher order nonlinear phenomena such as second harmonic generation, third harmonic generation, and two-photon absorption [7].

In the following section, we briefly study the dynamics of a nonlinear process, which can occur when an intense laser beam propagates through a medium. Typically, only laser light can provide sufficient intensity to cause changes in the optical properties of a material system [8]. The high-intensity levels of a laser optical field can induce a nonlinear polarization in the medium, which can be attributed to a nonlinear response of the elementary particles (e.g. atoms, molecules) of the medium to the incident optical field. For a loss-less medium, the induced polarization (P) can be given by a power series in the electric field vector (E), as given in Eq. (3.1) [10].

$$P_i(\omega, 2\omega, 3\omega, \dots) = \chi_{ij}^{(1)} E_j(\omega) + \chi_{ijk}^{(2)} E_j(\omega) E_k(\omega) + \chi_{ijkm}^{(3)} E_j(\omega) E_k(\omega) E_m(\omega) + \dots \quad (3.1)$$

Where the tensors $\chi^{(n)}$, $n = 1, 2, 3$, etc. represent the optical susceptibilities. Focusing on the first two terms in Eq. (3.1), and neglecting the third and higher order effects (see Eq. (3.2)) the equation becomes:

$$P_i(\omega, 2\omega, \dots) = \chi_{ij}^l E_j(\omega) + \chi_{ijk}^{nl} E_j(\omega) E_k(\omega) + \dots \quad (3.2)$$

Where the tensor χ^l is the linear optical susceptibility allowed in all media, and the tensor χ^{nl} denotes the second order harmonics (SHG) allowed only in noncentrosymmetric media. The graphical representations of linear and nonlinear responses are depicted in Fig. 3.1.

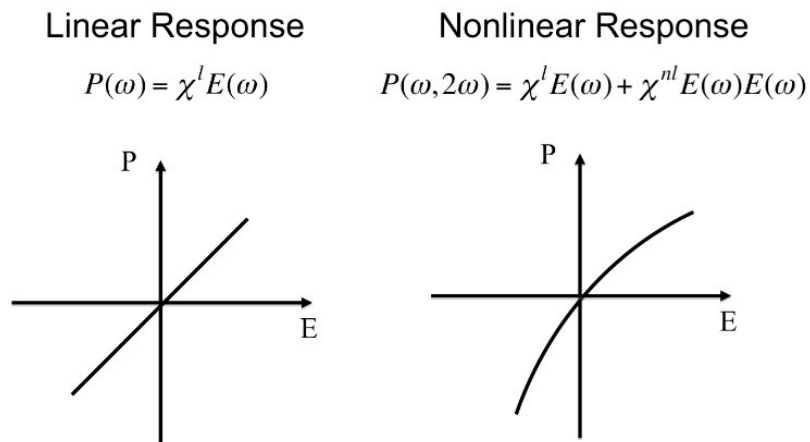


Fig. 3.1. Graphical illustrations showing, optical polarization (P) Vs optical electric field vector (E), for linear and nonlinear optical responses in a medium.

In a centrosymmetric medium, a medium with inversion symmetry, for every point (x, y, z) in the unit cell there is an indistinguishable point (-x, -y, -z). Therefore, in such a medium the inversion symmetry operation gives:

$$\hat{I}P(\omega, 2\omega, \dots) = -P(\omega, 2\omega, \dots) \quad (3.3)$$

$$\hat{I}E = -E \quad (3.4)$$

Here (\hat{I}) stands for the inversion symmetry operator. Using Eq. (3.3) and Eq. (3.4) in Eq. (3.1) we find:

$$\hat{I}P_i(\omega, 2\omega, 3\omega, \dots) = -\chi_{ij}^{(1)}E_j(\omega) + \chi_{ijk}^{(2)}E_j(\omega)E_k(\omega) - \chi_{ijkm}^{(3)}E_j(\omega)E_k(\omega)E_m(\omega) + \dots \quad (3.5)$$

Comparing Eq. (3.3) and Eq. (3.5), we find that all even powers in the susceptibility are zero in a centrosymmetric medium, i.e.

$$\chi_{ijk}^{(2)} = \chi_{ijkmq}^{(4)} = \dots = 0$$

This implies that even order effects such as SHG are only allowed in a medium with broken inversion symmetry [92]. Therefore, SHG is usually a forbidden process in bulk crystals of centrosymmetric magnetic garnet materials (e. g. YIG). However, epitaxially grown magnetic garnet films lack inversion centers due to the broken space-inversion and time-reversal symmetries, resulting in a SHG response in these films. Study of the origin of SHG signals in noncentrosymmetric magnetic garnet (Bi:YIG) films form the subject of this project.

3.2.2. The SHG process

SHG is the lowest order nonlinear-process and plays an essential role in a noncentrosymmetric material system. Crystalline materials with broken inversion symmetry can exhibit a so-called $\chi^{(2)}$ nonlinearity. The presence of a nonzero $\chi^{(2)}$ susceptibility leads to a nonlinear polarization in a medium. An in-depth analysis of the problem using the Maxwell's wave equations predicts that the induced nonlinear polarization wave radiates an electromagnetic field with a frequency, which is twice the

frequency of the fundamental radiation. Therefore, the process is also known as frequency doubling [7].

The physical mechanism behind the SHG process can be understood as follows. In a $\chi^{(2)}$ medium, the pump wave (ω) generates a nonlinear polarization wave, which then oscillates with twice the pump frequency (2ω), as shown in Fig. 3.2 (a). The energy-level diagram of Fig. 3.2 (b) describes the SHG as a quantum-mechanical process, where two photons of frequency (ω) are destroyed and a photon of frequency (2ω) is simultaneously created. Under proper experimental conditions, the process of SHG can be highly efficient; in fact, it is possible that almost all of the power in the incident fundamental beam can be converted to the second harmonic radiation [7].

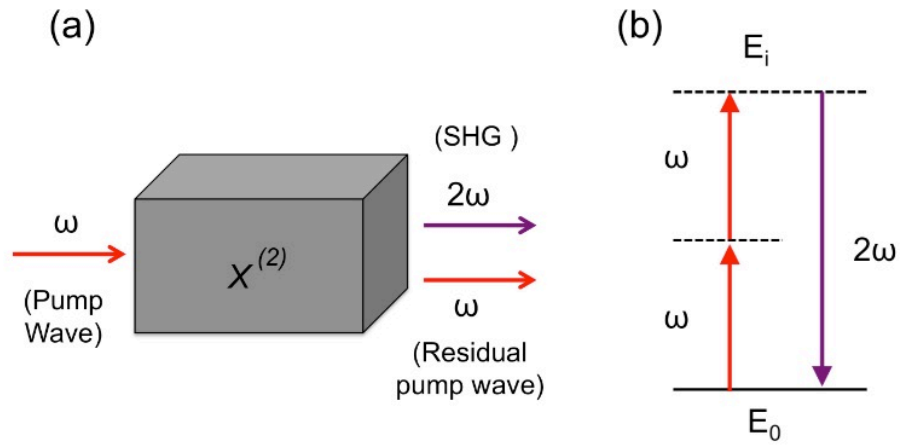


Fig. 3.2. (a) Geometrical representation of SHG. (b) Illustration of SHG using the energy-level diagram.

The SHG process finds a number of interesting applications in the field of surface nonlinear optics and nonlinear optical microscopy. The ultra-high sensitivity delivered by SHG has proven to be a very resourceful technique for rigorous diagnostics of the magnetized surfaces and buried interfaces of various materials types [10,11]. In nonlinear microscopy, SHG signals are shown to provide enhanced transverse and longitudinal resolution. This enhanced resolution is a result of the second harmonic waves being excited most efficiently in the region of maximum intensity of a laser beam

[7,8]. Moreover, in the nonlinear microscopy experiments, SHG is advantageous as it creates a large separation in frequency between the signal and the background noise.

3.2.3. SHG in magnetic garnet films

The bulk bismuth-substituted iron garnet is a cubic centrosymmetric material with inversion centers. However, prior studies on structural and magnetic properties of epitaxially grown magnetic iron garnet films have revealed that the films lose their cubic symmetry and transform to lower symmetry (uniaxial or orthorhombic) structures [23,86]. Thus, the films acquire a noncentrosymmetric configuration with missing inversion centers.

In the electric dipole approximation, two types of nonlinearity of crystallographic and magnetic origin may coexist in noncentrosymmetric crystal structures, such as in epitaxially grown anisotropic magnetic films [10]. The crystallographic part arises from space-inversion symmetry breaking, whereas the magnetic part arises from time-reversal symmetry breaking in a crystal. A schematic illustration of the two discrete-symmetry operations is shown in Fig. 3.3.

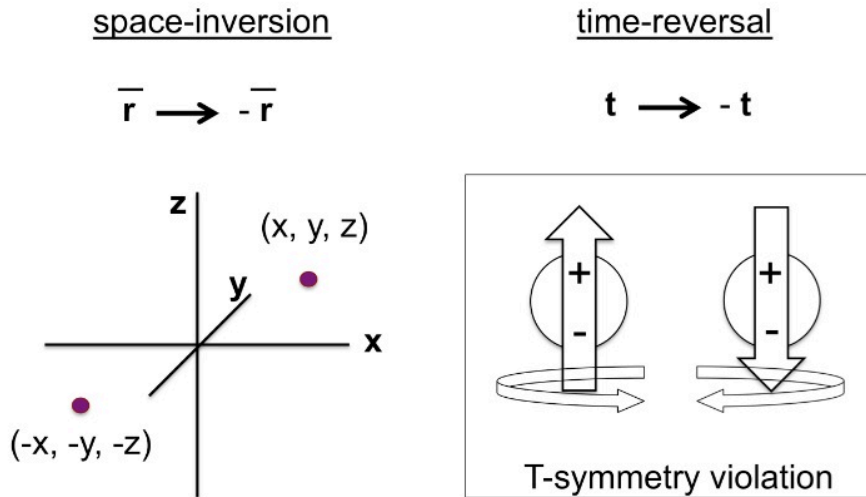


Fig. 3.3. Schematic representations of space-inversion and time-reversal symmetry operations. Image on the right also highlights the time-reversal symmetry in particles possessing electric dipole moments (e.g. electrons).

Usually, a charged particle possessing both an electric dipole moment and a spin is converted into a different type of particle carrying opposite spin. This time-reversal symmetry (T-symmetry) violation is depicted in Fig. 3.3 [93].

Thus, in an anisotropic medium lacking the two symmetry operations (space-inversion and time-reversal), the total quadratic nonlinear polarization can be given by:

$$P^{nl}(2\omega) = \chi^{cr} E(\omega)E(\omega) + \chi^{ma} E(\omega)E(\omega)M \quad (3.6)$$

$$P^{nl}(2\omega) = P^{cr}(2\omega) + P^{ma}(2\omega) \quad (3.7)$$

Where $P^{cr}(2\omega)$ represents the crystallographic contribution and $P^{ma}(2\omega)$ represents the magnetic contribution. The two contributions are of electric-dipole nature and simultaneously allowed in noncentrosymmetric media. The crystallographic susceptibility, χ^{cr} , is a polar tensor of rank 3 and the magnetic susceptibility, χ^{ma} , is an axial tensor of rank 4. In a lossless medium, χ^{cr} is a real tensor and χ^{ma} is an imaginary tensor.

A number of studies in the literature are available on the magnetic and crystallographic origin of the nonlinear response in centrosymmetric magnetic garnet films [94]. In a comprehensive work, Gridnev et. al. [10] reported on the effect of bismuth substitution on the second harmonic response in YIG films. Lyubchanskii and coworkers performed a detailed theoretical analysis on the influence of strain on SHG in these films [21]. In another study, Pisarev et. al. pointed out that a symmetry lowering mechanism in epitaxial grown magnetic garnet films results from elastic deformations [23]. However, a detailed systematic investigation of the effect of film strain, the systematic inclusion of lattice mismatch strain, strain gradients and fluctuations, and bismuth substitution on the nonlinear response in this material system is missing from this area of research.

This dissertation addresses these issues through a systematic and precise investigation in technologically-important bismuth-substituted iron garnet $(\text{Bi,Y})_3(\text{Fe,Ga})_5\text{O}_{12}$ films. The study includes the incorporation of internal stresses due to lattice mismatch and

micro-strain in sputter-deposited Bi:YIG films for their impact on SHG. We employ a radio-frequency (RF) sputter deposition method, which allows the inclusion of Bi and the generation of strain gradients. This is of particular interest since the presence of strain gradients and micro-strain (strain fluctuations), as well as the presence of lattice mismatch strain have been reported to contribute to the nonlinear response in magnetic garnets and other materials [21,22,95]. In the present work, we study their effect and that of composition on a set of Bi:YIG samples on the SHG response of the films.

3.3. Experimental methods

The development of internal stresses/strain, which is largely contributed by lattice mismatch between the gadolinium gallium garnet ($\text{Gd}_3\text{Ga}_5\text{O}_{12}$, acronym: GGG) substrate and the sputter-deposited bismuth-substituted iron garnet $((\text{Bi},\text{Y},\text{Lu})_3(\text{Fe},\text{Ga})_5\text{O}_{12})$ (acronyms: Bi:YIG, Bi:YLuIG or Bi:LuIG) film, produces a significant impact on SHG in ferrite garnet films. This study constitutes an important part of the dissertation work. An equally important part of this investigation is the surface/interface SHG, a process that has emerged as an important technique for probing surfaces and buried interfaces in the last two decades. Surface SHG can overcome the selection rule prohibition of second-order harmonics in bulk media with inversion symmetry such as YIG [96-100]. For this reason, our study plays an important role in deepening and extending the analysis of this process to magnetic media.

In this project, more than forty samples have been fabricated and characterized for their nonlinear response, with a particular emphasis on strain components and the films' stoichiometry composition. All samples were analyzed by carrying out a systematic study of the role of the different growth parameters on the nonlinear response of magnetic garnet films. These samples were tested for nonlinear response using a high-end femto-second Ti:Sapphire laser by our collaborators at the MSU. We then analyzed the results of these nonlinear tests for all of the samples at Michigan Tech.

3.3.1. Film fabrication: tools and techniques

We used an in-house radio-frequency (RF) magnetron sputtering system to grow epitaxial thin films of magnetic iron garnet materials. The large magneto-optic effects, transparency in the near-IR spectral range, and ability to control the room temperature ferrimagnetism adjudge Bi-substituted YIG films as good candidates for the present study. In this section, we first describe the RF-magnetron sputtering technique and then provide details on the Bi:YIG thin film deposition process.

(I) RF-magnetron sputtering: As mentioned earlier in chapter 2, the RF sputtering method differs from the DC sputter technique in that the electrode's polarity is varied at a radio frequency (13.56 MHz), allowing sputtering of almost all types of materials. In a magnetron, magnetic field traps are created to confine the motion of the electrons in close vicinity of the target. Typically, magnets are configured so that magnetic field lines are parallel to the target surface, thereby restricting the secondary electrons motion near the target. The arrangement of magnets in a conventional magnetron is shown in Fig. 3.4. The sputter-deposition system used in the present study is equipped with a conventional magnetron with a RF-power generator connected via a matching network (see Fig. 3.5).

A major advantage of a magnetron is that it increases the probability of electron-atom collisions, thereby providing dense plasma, which in turn results in improved sputtering rates. In recent years, magnetron sputtering has become the process of choice for the deposition of a wide range of industrially important coatings. In particular, the RF-magnetron technique plays an essential role in the sputter deposition of dielectric and insulator target materials. Specific advantages of this method include high elemental substitution and fine control over the film thickness.

(II) Film growth process: Fig. 3.5 shows a schematic drawing and a picture of the two-target RF-magnetron sputtering system used for depositing magnetic garnet thin films for this work.

Magnetron Sputtering

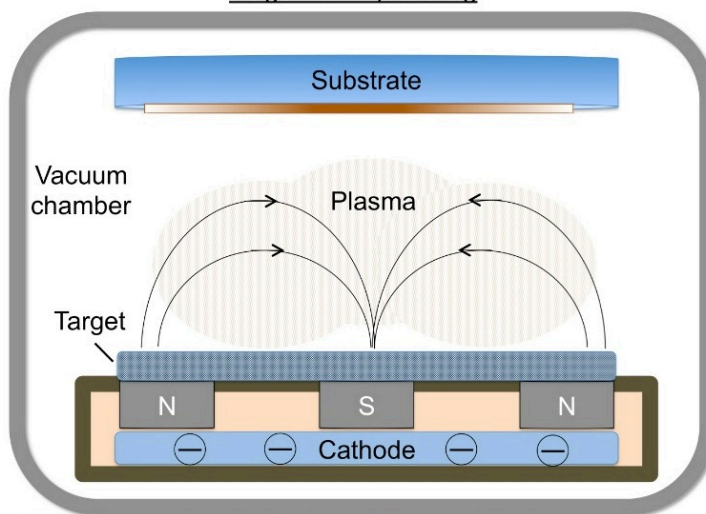
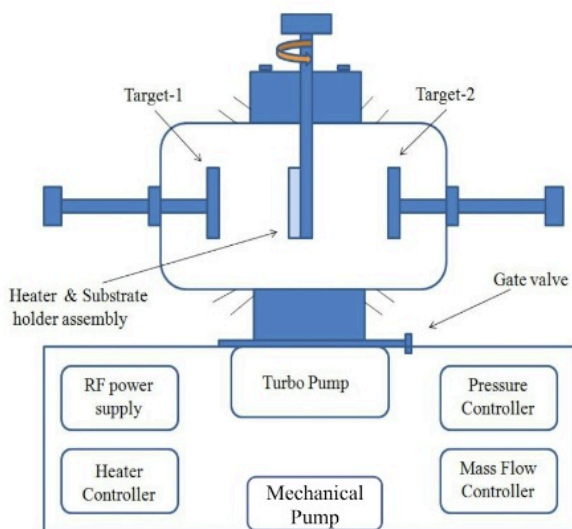


Fig. 3.4. Schematic representation of plasma confinement in a conventional magnetron system.

Sputtering system sketch



Sputter chamber picture

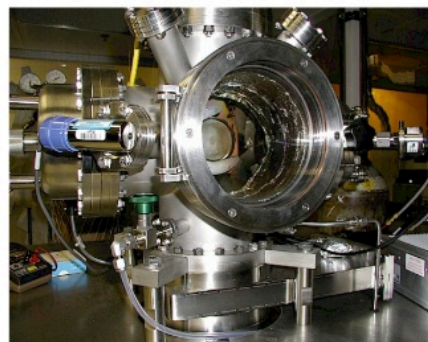


Fig. 3.5. Schematic and picture of the RF-magnetron sputtering system used in the present study.

Sintered ceramic targets, two-inches in diameter and a quarter-inch in thickness, with stoichiometric compositions of $\text{Bi}_{0.8}\text{Y}_{2.2}\text{Fe}_{4.8}\text{Ga}_{0.2}\text{O}_{12}$, $\text{Bi}_{0.8}\text{Y}_{2.2}\text{Fe}_4\text{Ga}_1\text{O}_{12}$, and $\text{Bi}_{1.5}\text{Lu}_{1.5}\text{Fe}_4\text{Ga}_1\text{O}_{12}$ were used.

The main steps in the film deposition process are as follows. The first step is substrate preparation. The substrate is cleaned in acetone, methanol, and de-ionized water in an ultrasonic bath and dried using a nitrogen gun. The purpose of this step is to remove large organic impurities from the substrate. Surface quality plays an important role in preparing high quality crystalline thin films. Therefore, the above cleaning process is repeated until cleanliness of the substrate surface is achieved. The substrate is attached to a molybdenum (Mo) substrate-holder using silver paste. It is then placed inside the sputtering chamber, which is subsequently evacuated to very low pressures (approximately 10^{-6} - 10^{-7} Torr) by using a turbo pump. The process steps are summarized in Fig. 3.6. A list of typical film-growth parameters is given in Fig. 3.7.

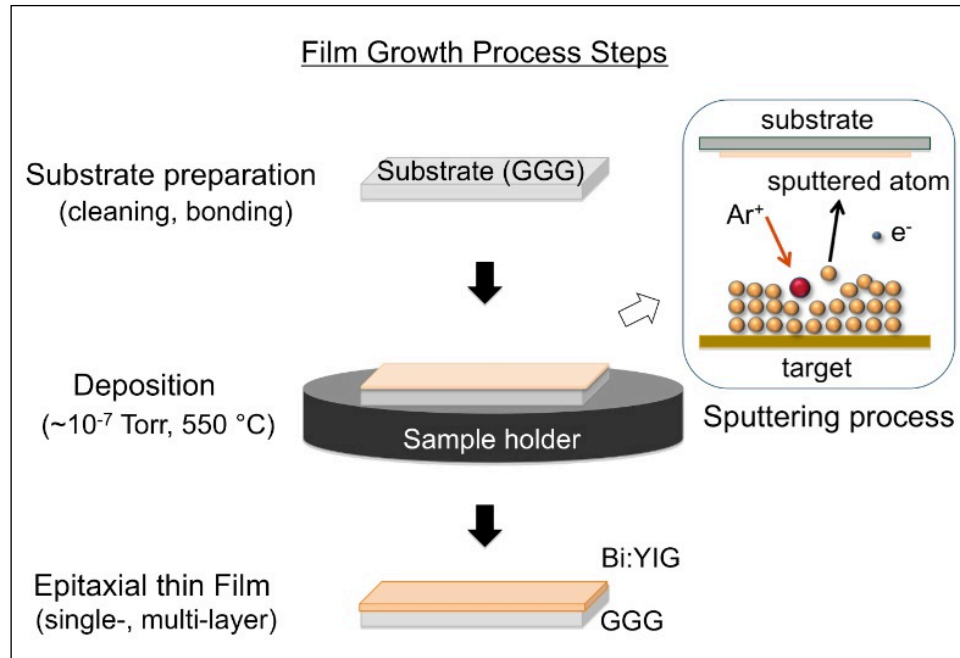


Fig. 3.6. Schematic representation of Bi:YIG thin film growth process. The sputtering process is highlighted in the inset (for details see section 2.3.3).

Film Growth Parameters

▪ Pressure (base)	-	10 ⁻⁷ Torr
▪ Pressure (working)	-	22 mTorr
▪ Power	-	80 Watt
▪ Substrate temperature	-	550 °C
▪ Argon flow rate	-	20 sccm
▪ Film thickness	-	300 nm to 1200 nm
▪ Deposition rate	-	4 to 6 nm/min

Fig. 3.7. Typical film growth parameters used to grow Bi:YIG thin films.

Bi:YIG films of different thicknesses (300nm-1200nm) are sputter-deposited on 1cm² pieces of (111)-oriented single crystal GGG or on (Gd,Ca,Mg)₃(Ga,Zr)₅O₁₂ (CMZ:GGG) substrates. The relevant growth parameters being systematically studied by this project for their impact on the garnet's nonlinear response are argon flow rate, gas pressure, growth temperature, oxygen ambient and film deposition time. A complete list of all samples, with corresponding sputtering conditions and target compositions, is given in Table A1.1 to A1.5 in the Appendix 1. Five different sets of films were fabricated and characterized for crystalline nature, transmittance, Faraday rotation, refractive index and thickness. These films were then sent to Moscow State University for second harmonic generation (SHG) studies. All samples were fabricated in five different sets, with the aim of carrying out a systematic study of the role of the different growth parameters on the nonlinear response of magnetic garnet films.

The first set of films (set-1) was grown using a single target (Bi_{0.8}Y_{2.2}Fe_{4.8}Ga_{0.2}O₁₂). This target was subjected to two different magnetron field configurations inside the chamber, determined by the gun on which the target was mounted. We identify these guns by their placement (left or right as seen from the loading port) on the chamber. The target to the left was under a stronger magnetic field strength and the distance between target and substrate was about 3.7cm. The same target when placed on the right side

was subjected to a weak magnetic field strength and larger distance between target and substrate ($\sim 4.0\text{cm}$). This set consists of total eight samples with four samples sputter deposited from each gun, using the same target (see Table A1.1 in Appendix 1).

All the films in set-2 were grown using a second target ($\text{Bi}_{0.8}\text{Y}_{2.2}\text{Fe}_4\text{Ga}_1\text{O}_{12}$) under conditions that were adjusted based on the preliminary results of the SHG measurements of set-1. In other words, we sought to optimize the sputtering conditions for maximal nonlinear response. The reason for this choice of different targets was also to conduct a study of the effect of target composition on the nonlinear response. The second set of samples (see Table A1.2 in Appendix 1) was fabricated using the parameters corresponding to the film that showed the best SHG response in the first sample set. In addition one blank GGG and one blank CMZ:GGG substrates were studied for the nonlinear response of the substrate for calibration purposes. One GGG substrate, treated in the chamber “without plasma” under normal film deposition conditions, was added to this sample set to see the effect of argon and oxygen gases on substrate crystallographic structure.

Sample set-3 consisted of samples fabricated with the aim of exploring the contribution to the nonlinear response from films surfaces and interfaces. The rationale for this approach was that our measurements on the first two sets were yielding evidence that the main contribution to the nonlinear response was coming from the surfaces and interfaces. Subsequent measurements have confirmed this assessment. This set (see Table A1.3 in Appendix 1) included two double layer films deposited using two different targets $\text{Bi}_{0.8}\text{Y}_{2.2}\text{Fe}_{4.8}\text{Ga}_{0.2}\text{O}_{12}$ and $\text{Bi}_{0.8}\text{Y}_{2.2}\text{Fe}_4\text{Ga}_1\text{O}_{12}$, in order to increase the number of interfaces and observe its effect on the second harmonic signal. Other films in the set were surface patterned, by photolithography and focused ion beam (FIB) milling, to understand the role of surface patterning on the nonlinear response. The surface nonlinear study was based on the fact that in surface region of centrosymmetric materials the inversion symmetry is broken and leads to a large nonlinear polarization [96-98].

The study of target composition on the nonlinear response was continued in sample set-4 (see Table A1.4 in Appendix 1). In this set two films were sputter-deposited using

target composition $\text{Bi}_{1.5}\text{Lu}_{1.5}\text{Fe}_4\text{Ga}_1\text{O}_{12}$. Other two films in the set were deposited using target $\text{Bi}_{0.8}\text{Y}_{2.2}\text{Fe}_4\text{Ga}_1\text{O}_{12}$.

A systematic study was done to explore the role of interfaces in the nonlinear response of the garnet films under set-5, totaling six multilayer films (two-5 layers, two-10 layers and two-15 layers films), and tested for SHG. The growth parameters for set-5 are presented in Table A1.5 in Appendix 1. The results obtained tend to confirm the role of interfaces in improving the nonlinear response in these magnetic garnet films (see Result/Discussion section).

We have also conducted a compositional study of the films using the Rutherford Backscattering Spectrometry (RBS) Technique [101]. This study has helped us pinpoint the elemental contribution to the nonlinear response; more detail on this is given in the Results and Discussion section.

3.3.2. Film characterization

The following characterization measurements were performed on all the sputter-deposited thin film samples.

(I) X-ray diffraction (XRD) measurements: The XRD analysis was carried out to study film crystallinity. All the experiments were performed on a Scintag XDS-2000 θ/θ diffractometer (see Fig. 3.8). We investigated the effect of oxygen inclusion in the chamber on the crystalline properties of the films. A comparison study was done between XRD spectra of two Bi:YIG samples deposited under different oxygen flow condition, one deposited in the absence of oxygen (BiYIG080607) and the other in the presence of oxygen (BiYIG120507) but under the same argon flow rate, RF power, and chamber pressure (see Fig. 3.9). The small growth temperature difference of 10 °C has been found not to affect the properties of the films and is not considered significant. Although both films exhibit a crystalline structure, as shown by the presence of XRD peaks in both cases, BiYIG080607 (grown in the absence of oxygen) is under a higher strain (as shown by the larger separation between film and substrate peaks) than BiYIG120507. Subsequent SHG measurements showed that samples grown in the

absence of oxygen display a stronger nonlinear response. We consider this to be an important finding of the project, the causes of which are discussed in the results/discussion section of this report.

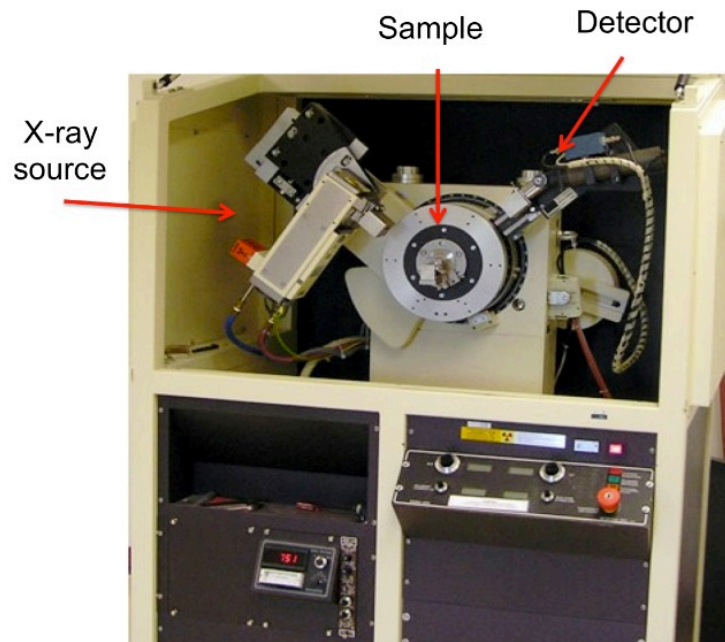


Fig. 3.8. Scintag XDS-2000 θ/θ diffractometer used for x-ray measurements of Bi:YIG films.

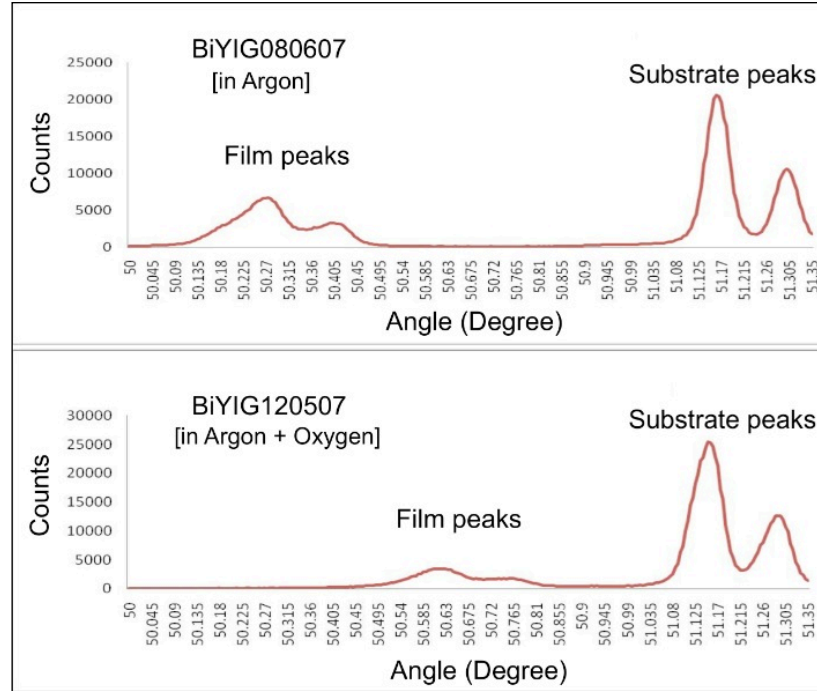


Fig. 3.9. XRD pattern of BiYIG080607 film deposited without oxygen (upper graph) and of BiYIG120507 film deposited with oxygen (lower graph).

In plane anisotropy study of a typical sample was done by taking XRD patterns of the sample at five different azimuthal angles (0° , 45° , 90° , 135° and 180°). A small trace of in-plane anisotropy was detected as shown in the Appendix 2 of the report.

(II) Thickness and Refractive Index measurements: A Metricon Model 2010 prism coupler with ± 0.001 for film index and ± 5 nm for film thickness accuracy was used to characterize thickness and refractive indices of Bi:YIG films. The instrument offers a resolution of ± 0.0005 and $\pm 0.3\%$ in index and thickness, respectively.

The working principle of the prism coupler is as follows [102]. The film to be measured is brought into contact with the high refractive index prism by means of a pneumatically controlled coupling head as shown in Fig. 3.10 (a). The laser beam strikes the base of the prism and is reflected onto the photo detector. The whole assembly, which includes prism, film, coupling head, and photodetector, are mounted on a rotatory table, thus allowing varying the angle of incidence of the laser beam. At certain values of the angle of incidence (θ), the laser beam violates the total internal reflection criterion

and tunnels through the base of the prism into the film and excites propagation modes, causing a sharp drop in the intensity of light reaching the photo detector, as shown in Fig. 3.10 (b). The film thickness and refractive index values are then calculated using a computer program on the basis of the TE and TM modes dispersion relations, using the information on mode angle θ extracted from the measurements, laser wavelength, substrate index, and refractive index of the prism [103].

For Bi:YIG samples index and thickness measurements were done at 632.8nm wavelength. Results showed that all samples are about one μm or less in thickness allowing us to probe film-substrate interface region in the nonlinear studies. Refractive index is used to assess the reflectivity of the films and to analyze optical coupling in waveguide structures fabricated on these films. Dependence of SHG signal on film thickness is discussed in the result/discussion section of the report.

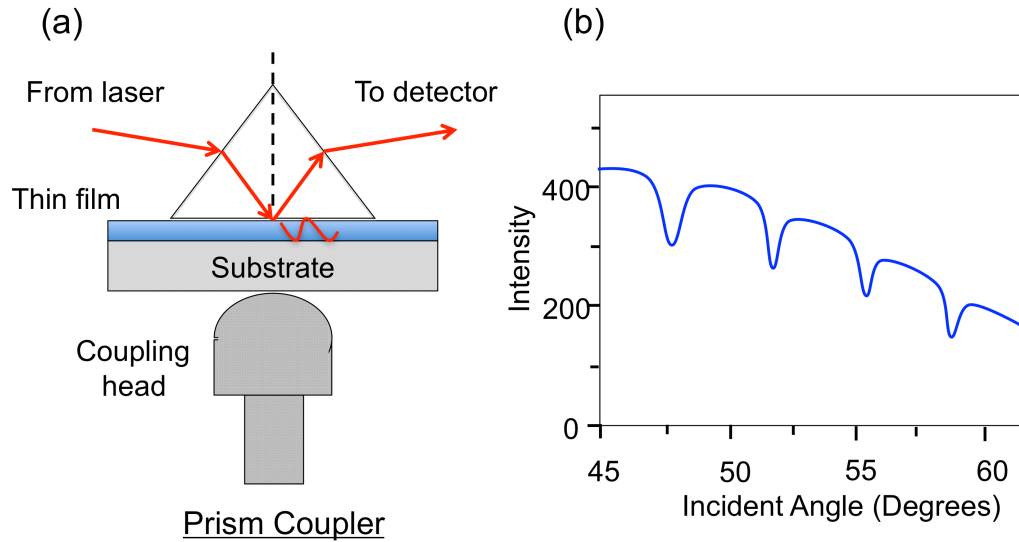


Fig. 3.10. (a) Schematic of a prism coupler, and (b) illustration of measured spectrum showing dips in the intensity at various mode angles.

(III) Faraday rotation (FR) measurements: Magneto-optic quality of the Bi:YIG films was evaluated through FR measurements. The measurements were done in transmission geometry. Polarization rotations up to $3.1^\circ/\mu\text{m}$ were observed at $\lambda = 473\text{nm}$, other wavelength used were 523nm and 632.8nm, showing that our films performed well as

Faraday rotators. The FR measurements of a blank substrate were performed. These were then used to extract the actual FR value of the film.

(IV) Film transmittance measurements: Transmittance of the films was calculated in the range 400nm to 700nm using a spectrophotometer. These spectra were found to agree with typical iron garnet transmittance, with significant absorption below 500 nm and higher than 50% transmittance above 500 nm.

(V) Composition measurements: Normally, epitaxial garnet films undergo compositional change from the stoichiometrically prepared sintered ceramic target of $((\text{Bi},\text{Y})_3(\text{Fe},\text{Ga})_5\text{O}_{12})$ material when deposited using a sputtering process. Obtaining the same stoichiometry, as that of the target is difficult due to the complexity of the garnet structure and the sputtering process itself [104]. The Bi:YIG films' stoichiometry composition was studied using the Rutherford Backscattering Spectrometry (RBS) technique. RBS was done commercially [101], but we analyzed the results at Michigan Tech. The schematic diagram in Fig. 3.11 shows the scattering geometry in a typical RBS experiment.

Scattering Geometry of an RBS Experiment

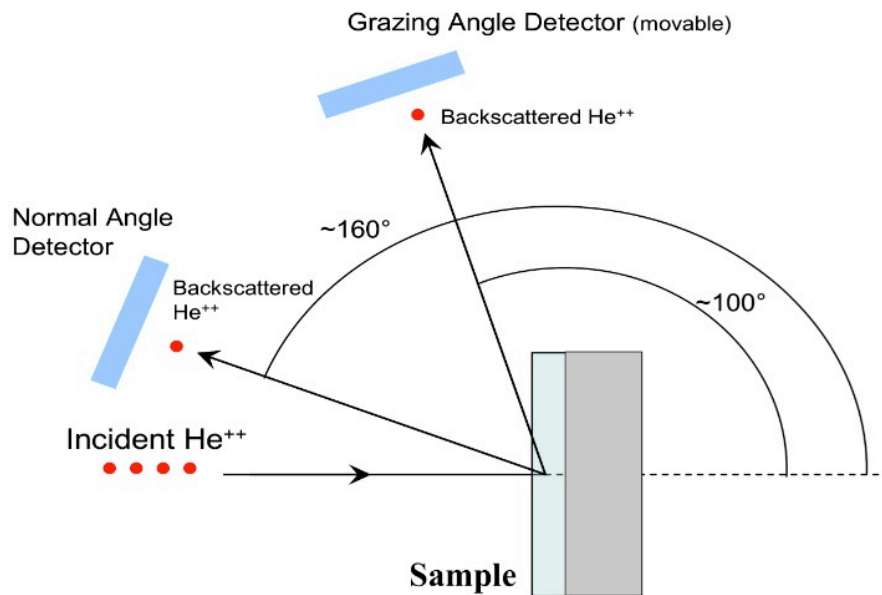


Fig. 3.11. RBS experimental setup.

In an RBS measurement high-energy He^{2+} ions (i.e. alpha particles) are directed onto the sample and the energy distribution and yield of the backscattered alpha particles at a given angle is measured. RBS spectra were acquired at a backscattering angle of 160° and an appropriate grazing angle (with the sample oriented perpendicular to the incident ion beam). The use of different detector angles can significantly improve the accuracy of both, thickness and composition in an RBS measurement. A shallow grazing angle spectrum is used when thin surface layers need to be analyzed. Typical analytical parameters used in the RBS experiment are summarized in Table 3.1.

Table 3.1. Analytical Parameters: RBS experiment.

He^{++} Ion Beam Energy	2.275 MeV
Normal Detector Angle	160°
Grazing Detector Angle	$\sim 118^\circ$

The spectra were fit by applying a theoretical model and iteratively adjusting elemental concentrations and thickness until good agreement is found between the theoretical and the experimental spectra.

3.3.3. Types of strain and their determination

In thin films a major part of the strain is caused by lattice mismatch (also called lattice misfit) between film and substrate. This lattice-mismatch strain (ϵ) in the Bi:YIG films is calculated using the expression $\epsilon = (a_f - a_s)/a_s$, where a_f and a_s are the film- and substrate-lattice constants along the normal to the plane of the film, respectively. Lattice-mismatch strain deforms the cubic geometry of the garnet unit cell under study, lowering its inversion symmetry and producing strain-induced SHG. A second source of SHG response in the Bi:YIG films can be traced to strain and compositional gradients, dislocations and strain fluctuations (collectively denoted as micro-strain). Micro-strain is explored in this work through X-ray line profile analysis. In the XRD graphs film peak broadening and distortions gauge the effect of strain variations and crystallite size

present in the film. Strain variations are usually caused by compositional gradients, strain relaxation across the thickness, and dislocations in the film.

Since the films deposited for this work are very thin compared to the substrate, the crystalline structure of the single-crystal substrate is not deformed much and is used as an internal standard for instrumental resolution. A careful analysis was performed in which distorted film peaks were treated with symmetrical Pearson-VII profiles, as shown for example in Fig. 3.12. The film peak of a typical sample is fitted by two Pearson-VII profiles. To calculate the effect of strain gradients, strain fluctuations, and crystallite size on XRD profile broadening a simplified Williamson-Hall fit was applied to two lattice-plane peaks (444 and 888) parallel to film surface. Note that in Fig. 3.12, the peaks corresponding to (444) planes of the film and substrate are shown; in this figure (888) peaks are not shown. The strain values for each fitted peak are extracted from the slope of the line passing through the origin of a standard $(FWHM) * \cos\theta = 4\varepsilon' \sin\theta$ plot. Here FWHM is the full-width-half-maximum (in radians) of the fitted Pearson-VII profiles, corrected for instrumental resolution, ε' is the micro-strain and θ is the XRD incidence angle. Since only two points (corresponding to 444 and 888 peaks) were accessible to us by XRD for the Bi:YIG thin films, the micro-strain was extracted by a straight-line fit through the origin; hence the form of the simplified expression relating FWHM to ε' given above. This method is equivalent to taking the average of the contributions to the profile broadening for both 444 and 888 profiles, and folds in all contributions to the broadening but folds out instrumental resolution.

Lattice mismatch strain was found to follow an inverse relation to the films' deposition rate, therefore providing a means for strain control during the film deposition process. Of the two targets used in the film deposition in our magnetron sputtering system, those samples grown under a lower target-magnetic-field and larger target-substrate separation evinced higher lattice mismatch strain as compared to films grown under (\sim two times) higher target-magnetic field and lower target-substrate separation. This provides another control for handling strain content in the film via sputter process. In-situ post-annealing of one of the films showed a reduced lattice mismatch strain (least among all the samples).

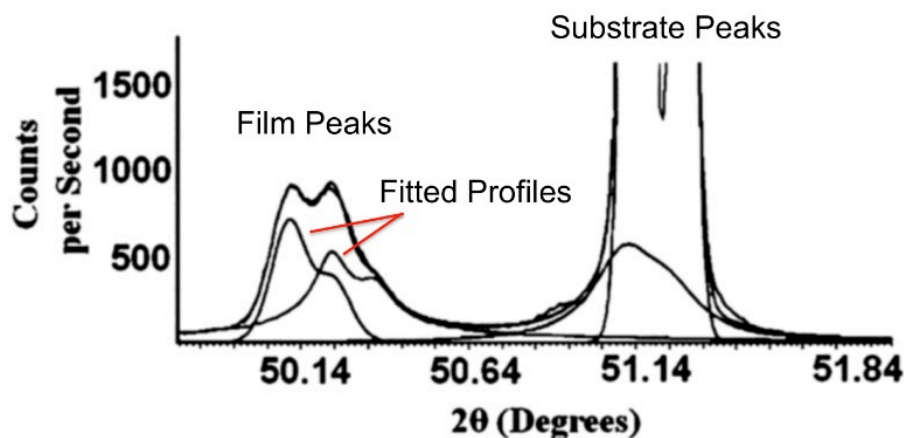


Fig. 3.12. Peak fit of (444) sample peak of a typical Bi:YIG sample using symmetrical Pearson VII profiles. Both film and substrate profiles have two peaks corresponding to XRD K α 1 and K α 2 lines.

3.3.4. Strain measurements

In this section the compositional and crystallographic origin of the lattice mismatch strain and micro-strain in the Bi:YIG film sample are explored. An absolute difference in the film and substrate lattice constants produces lattice mismatch strain in the film, with highest influence in the vicinity of film-substrate interface. To calculate the micro-strain and compositional variations in the film, XRD peak profiles were analyzed and the Bi:YIG films were scanned for depth profiles of the constitutive elements using RBS technique. The compositional analysis of a typical film shows that bismuth concentrations deviate from their stoichiometric value in the target [i.e. (Bi,Y)₃(Fe,Ga)₅O₁₂], as shown in Fig. 3.13. One reason behind this observation is that bismuth has a lower surface binding energy and liable to be preferentially sputtered. The changing Bi concentration causes a gradient/displacement in elemental concentrations across the film thickness. In all the film samples, a lessening trend in Bi concentration towards the surface of the film is observed, as shown in Fig. 3.13; however the concentrations of other elements (Y, Fe, Ga and O) stay more or less constant with depth inside the film. A possible reason for the decreasing Bi concentration towards the surface could be assigned to in-situ annealing of the growing Bi:YIG film. The diffusion of Bi, with relatively larger ionic radius (Bi³⁺), towards the interface brings about an

atomic rearrangement and renders an overall least strained crystallography in the film. This relative displacement of the elements causes local stress/strain generation, which along with various dislocations and stacking faults produces micro-strain across the film thickness.

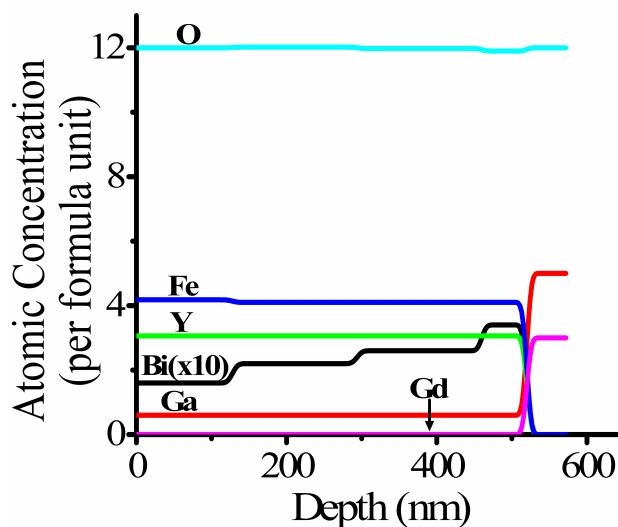


Fig. 3.13. Depth profiles of elemental concentrations in a typical sample

The micro-strain was found to be an order of magnitude smaller than the lattice mismatch strain. The gradient in Bi concentration across the film thickness noted here generates micro-strain, which contributes to the elimination of inversion symmetry in the film and enables the observed SHG. The average elemental concentrations, thickness and the average values of two types of strains corresponding to each Bi:YIG film sample are presented in Table 3.2.

Table 3.2. Elemental concentrations and strain values of the Bi:YIG samples [105].

Bi: YIG Film	Thickness(nm) (Error~ $\pm 10\%$)	Avg. atomic concentration (pfu) ^a					Avg. micro- strain (10^{-4})	Avg. lattice mismatch strain (10^{-4})
		Bi	Y	Fe	Ga	O		
1	687	0.23	3.01	3.95	0.48	12.33	3.6	176.4
2	896	0.27	2.44	4.50	0.64	12.15	12.5	97.5
3	692	0.30	2.70	4.20	0.30	12.50	11.4	133.6
4	453	0.29	2.70	3.80	0.34	12.87	2.6	117.8
5	520	0.25	3.06	4.12	0.60	11.98	1.6	185.6
6	743	0.23	3.08	4.20	0.44	12.05	9.6	182.0
7	552	0.27	2.60	4.60	0.50	12.03	14.3	129.1
8	455	0.21	3.00	3.20	0.30	13.29	17.1	205.9
9	595	0.34	2.84	4.30	0.32	12.20	5.0	131.5
10	345	0.31	2.80	3.70	0.40	12.79	11.4	138.6
11	1204	0.21	3.20	4.34	0.22	12.03	3.9	164.2
12	784	0.31	2.80	4.75	0.52	11.63	15.0	156.2
13	537	0.26	2.70	3.70	0.34	13.00	4.5	122.3
Uncertainty (pfu) $\pm \sim$		0.0003	0.02	0.04	0.002	0.5		

^apfu: per formula unit

3.3.5. SHG measurements

SHG measurements were carried out at Moscow State University by the group of Prof. Aktsipetrov, our collaborator in the project. The output of a femtosecond (pulse duration 80 fs) Ti: Sapphire laser at 800 nm was used as a source of fundamental radiation. The experimental setup consists of two channels, corresponding to signal and reference, as shown in Fig. 3.14. Measurement of the films' second harmonic response was done in reflection geometry in the absence of an external magnetic field. The light goes through a beam splitter, Glan-Taylor polarizer (to allow only a polarization state P), lens (focal length 5 cm), and then through filter- 2ω (to block the second harmonics from the source) before hitting the sample at an angle. The reflected radiation goes through a filter ω (to block the fundamental light at 800nm) and is collected by a lens (focal length 5cm) then going through Glan-Taylor analyzer (to separate out the polarization state of detected light with polarization state P or S). The measured data are normalized through a reference channel to minimize laser power fluctuations during the experiment. Typical analysis parameters used in the SHG measurements are given in Table 3.3.

Table 3.3. Analytical parameters: SHG experiment.

Laser source	Ti: Sapphire
Wavelength	800 nm
Pulse duration	80 femto-sec
Pulse repetition rate	80 MHz
Polarization analysis mode	PP, PS
Beam spot size on sample	20 μm
Measurement technique	Rotational anisotropy method

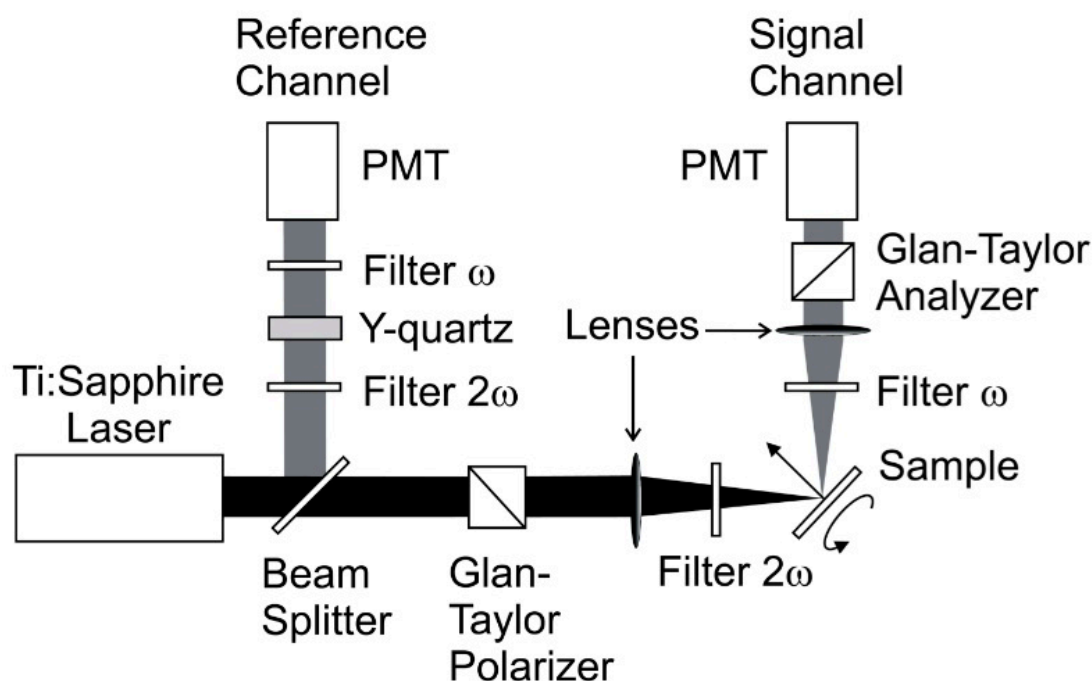


Fig. 3.14. Experimental Setup for SHG measurements.

For the magneto-optical characterization of the films the geometry of the transversal nonlinear magneto-optical Kerr effect (NOMOKe) is used. The azimuthal dependence of the second harmonic signal for a typical sample is shown in Fig. 3.15. As shown in this figure, the sample is illuminated from the film side (graph on left), and from the

substrate side (graph on right). Under both geometrical configurations the measurements show similar SHG, which indicates the important role of film-substrate interface.

The substrate does not deform much from its mono-crystal form due to the sputtering (see XRD graph in Fig. 3.9.) and hence shows a negligible contribution to SHG (see section 3.4.1). Also, there is no significant dependence of SHG signal on film thickness (see section 3.4.4). This leaves the interface region as the main source of SHG in the epitaxially grown film.

The measured SHG data of samples from all sets are summarized in Table A3.1 and Table A3.2 in the Appendix 3. Table A3.1 contains all PP (polarization: P-in and P-out) geometry data while Table A3.2 contains all PS (P-in and S-out) geometry data. Details on important finding of this experiment are given in the Result and Discussion section.

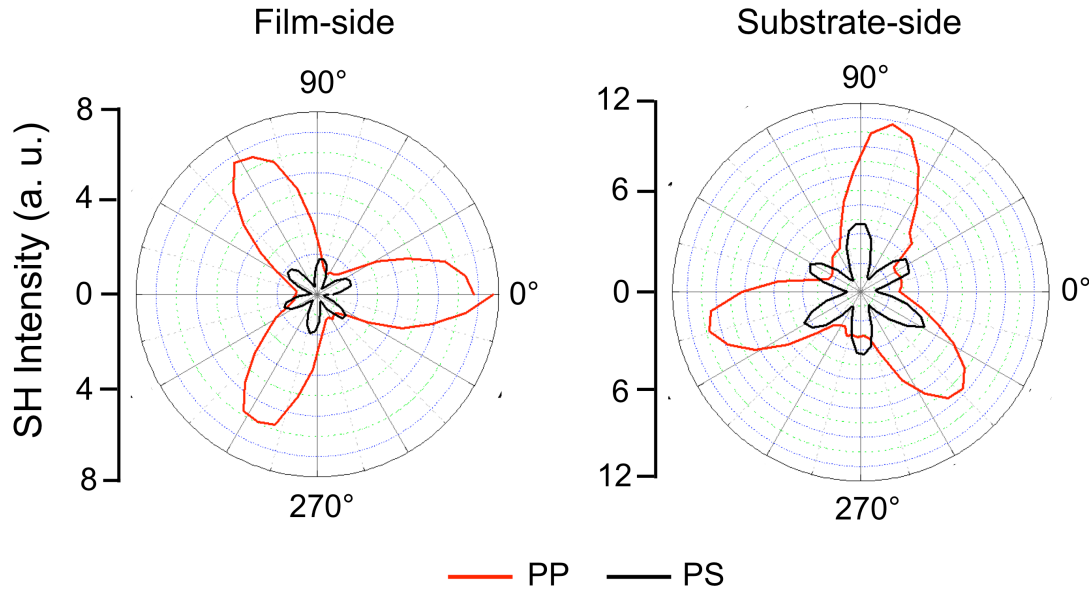


Fig. 3.15. Dependences of SHG signal on azimuthal angle of rotation for a sample shined on from film side (graph on left) and same sample shined on from substrate side (graph on right)

3.4. Results and discussion

All thin film samples were sputter-deposited and characterized for crystallinity, strain, transmittance, thickness, refractive index, and composition. The SHG measurements for all Bi:YIG and Bi:LuIG samples were carried out under the same conditions and both film-side and substrate-side illuminations were examined. The roles of following parameters were studied in detail, and the results are presented under the following headings in this section.

- (i) The role of substrate in SHG
- (ii) The role of oxygen in SHG
- (iii) The role of annealing in SHG
- (iv) The role of film thickness in SHG
- (v) The role of interface in SHG
- (vi) The role of lattice mismatch, micro-strain, and composition in SHG
- (vii) Hyper-Rayleigh scattering (HRS) study
- (viii) Surface effects investigation

3.4.1. The role of substrates in SHG

Since the deposited magnetic garnet films are very thin ($\leq 1\mu\text{m}$) compared to the substrate (0.5 mm), the crystalline structure of the mono-crystal substrate is not deformed much and is used as an internal standard for instrumental resolution. The measured nonlinear response from a blank GGG and CMZ:GGG substrates are shown in Fig. 3.16.

It is clear from Fig. 3.16, that GGG shows negligible SHG while CMZ:GGG bear a good amount of nonlinear signal. To keep the background contribution to the film SHG minimum, we have used GGG substrate for all samples except one.

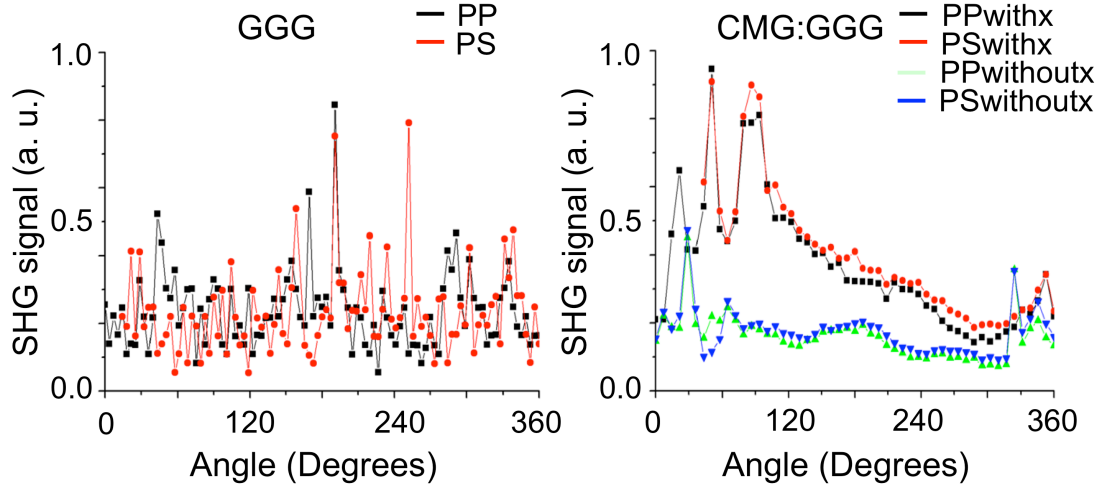


Fig. 3.16. SHG rotational anisotropy of GGG (left graph) and CMG:GGG (right graph) substrates.

3.4.2. The role of oxygen in SHG

We observe that SHG effectiveness strongly depends on the growth parameters and that the samples prepared in the absence of O_2 flow yield significantly stronger SHG response. In particular, we find that samples prepared under non-zero O_2 flow rates (~ 0.1 sccm) result in the degeneration of the crystallographic structure on a subsurface layer. Figs. 3.17(a) and 3.17(b) depict the SHG polar patterns showing azimuthal dependence measured for the P-in, P-out and P-in, S-out combinations of polarizations for the samples. Fig. 3.17(a) shows the pattern for a film prepared in Argon + Oxygen ambient, Fig. 3.17(b) Argon ambient only. We notice that SHG effectiveness strongly depends on the growth parameters and that the sample prepared in the absence of O_2 flow presents significantly stronger SHG response. In Figs. 3.18(a)-(d), we compare the SHG rotational anisotropy of four samples, two of these grown in the presence of oxygen (shown in Figs. 3.18(a) and (b)) and other two grown in the absence of oxygen (shown in Figs. 3.18(c) and (d)).

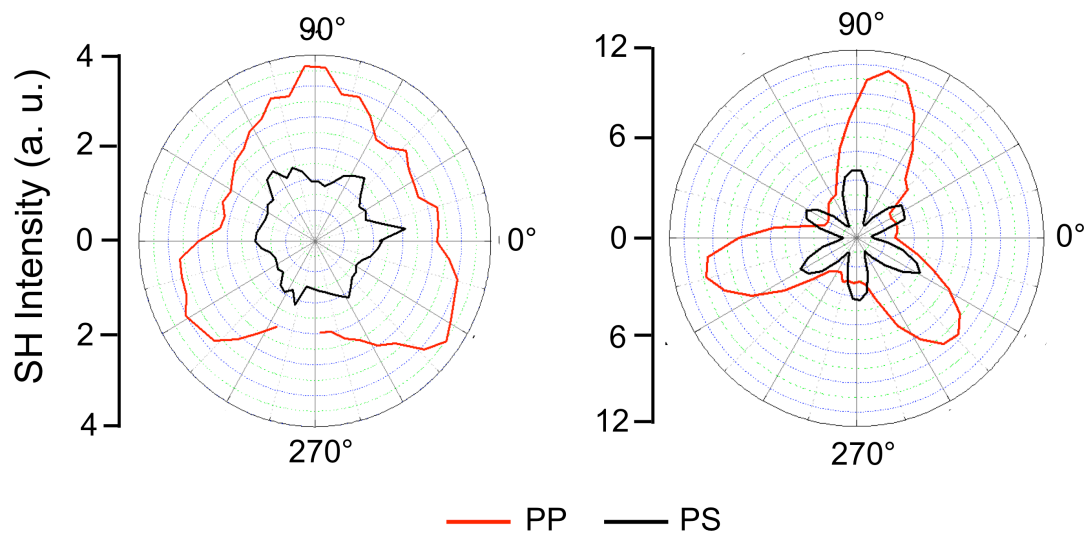
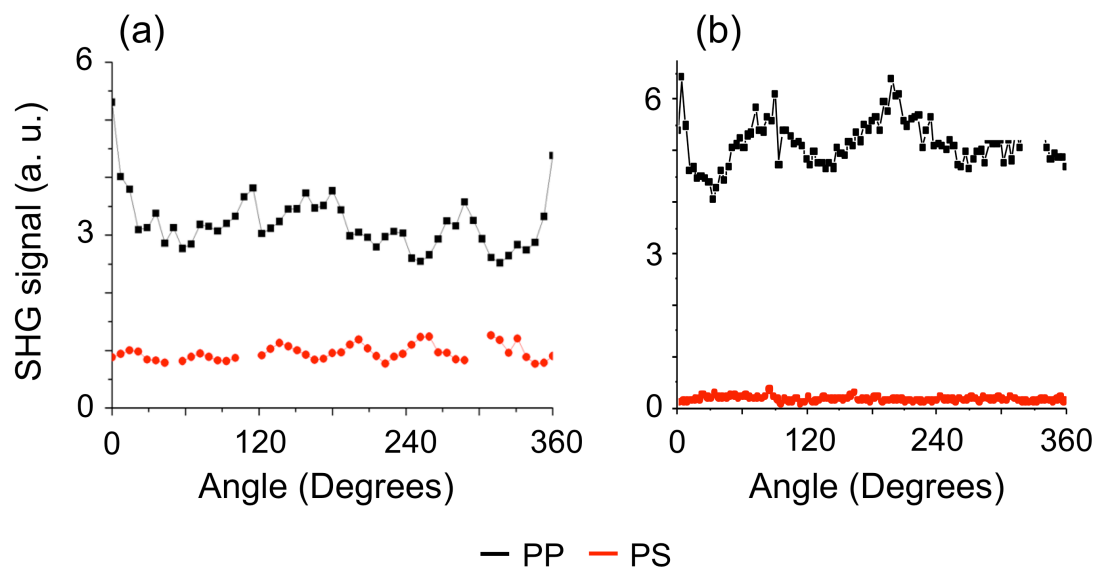


Fig. 3.17. (a) SHG measurement for film prepared with oxygen (in Argon + Oxygen), (b) SHG measurement for film prepared without oxygen (in Argon only).



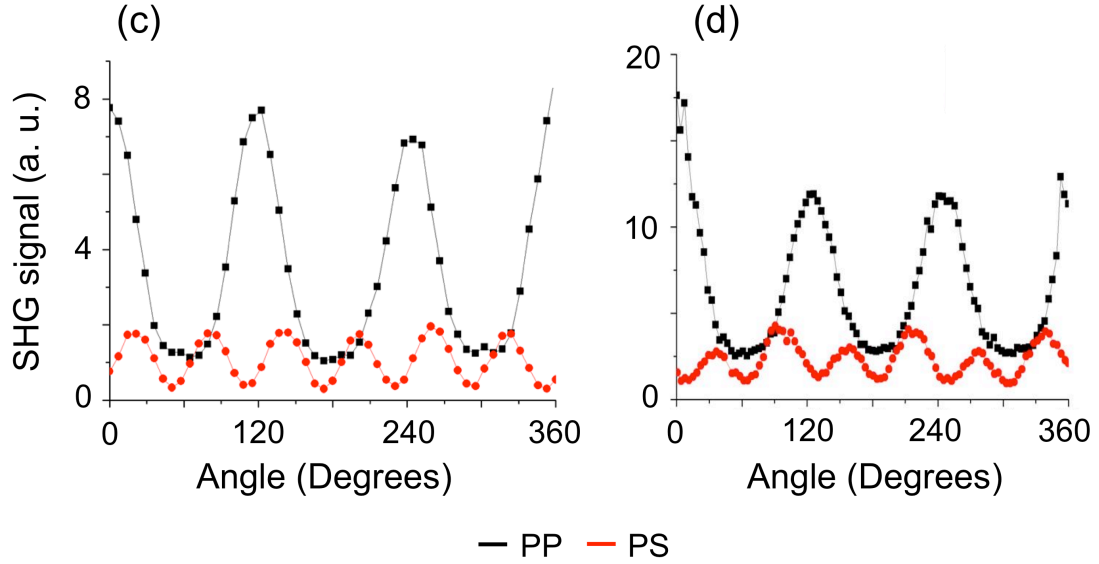


Fig. 3.18. SHG rotational anisotropy of (a) BiYIG111507 (in Ar + O₂), (b) BiYIG021808 (post annealed in O₂), (c) BiYIG072407 (in Ar) and, (d) BiYIG013108 (in Ar), all illuminated on the film side.

From Fig. 3.18(a) and 3.18(b) it is clear that the films grown in an oxygen ambient (or post annealed in O₂) show poor nonlinear response. Also a trace amount of SHG under PS geometry conditions, for the samples grown in an oxygen ambient indicates the presence of atomically flat surfaces with poor crystalline quality. It seems that the oxygen penetrates into the film about few tens of nanometers and destroys the near-surface crystallographic structure. A possible explanation for this is the following: all films are grown at an optimized temperature (550 °C) for best crystalline quality in argon atmosphere; when films are deposited in an Ar + O₂ atmosphere at such high substrate temperatures, degradation of the film near-surface takes place due to the bombardment of energetic oxygen atoms over the growth film surface. The small SHG signal in the presence of oxygen flow can be attributed to the relaxation of internal stress/strain in the grown epitaxial films due to the substitution of oxygen atoms in film lattice. A statistical study (Fig. 3.19) shows that the samples grown in O₂ ambient (green columns in Fig. 3.19) have least lattice mismatch among all the grown samples from set-1 and set-2. The observed stress relaxation is consistent with surface damage and with

the observation (discussed below) that film strain tends to favor a stronger nonlinear response.

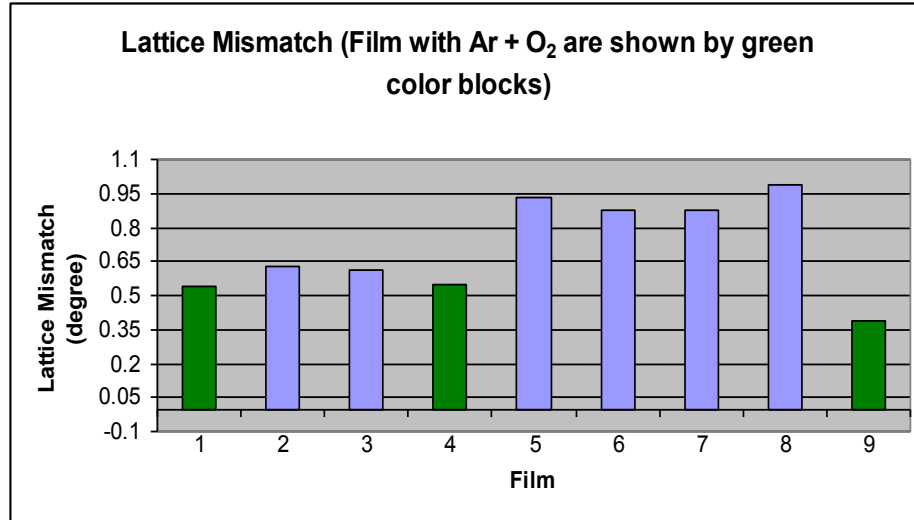


Fig. 3.19. Oxygen effect on Lattice mismatch-A statistical graph drawn for the films from set-1 and set-2

All these facts suggest that oxygen in the chamber induces near-surface damage and reduces lattice mismatch, which in turn degrade the nonlinear response of the films, establishing a direct relation between strain and SHG efficiency.

3.4.3. The role of annealing in SHG

The effect of annealing was studied for selected thirteen samples, as shown in Fig. 3.20, where the annealed data points are shown with closed circles and unannealed data points with open circles. The films were annealed in a furnace in air ambient for 4hrs at 700C. Strain values for annealed and unannealed samples were calculated by analyzing their XRD graphs. Fig. 3.20 shows a strong positive correlation between SHG, and lattice mismatch strain (left graph) for the unannealed samples; whereas for the annealed samples SHG does not correlate with SHG. We observe the opposite effect in annealed samples for micro-strain as shown in Fig. 3.20 (right graph), where SHG signal evinces a strong correlation on micro-strain for the annealed samples and a random behavior for the unannealed ones.

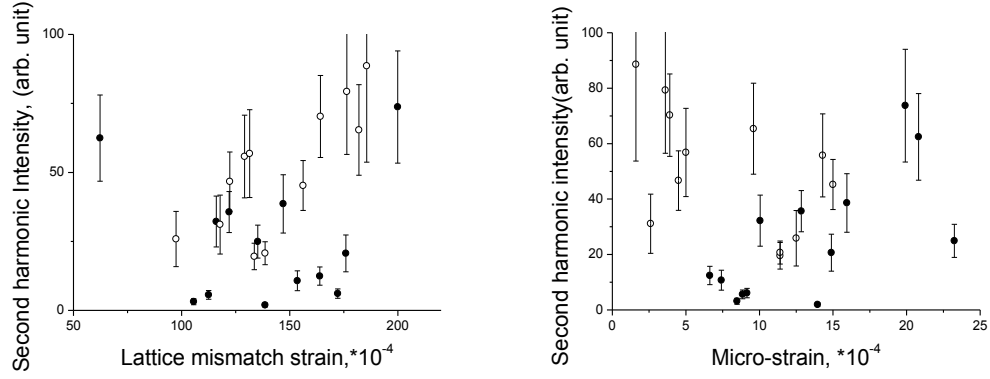


Fig. 3.20. SHG signal dependence on lattice mismatch strain (left graph), and micro-strain (right graph) of the annealed (close circles) and unannealed (open circles) film samples.

Assuming quadratic growth of SHG on strain we suggest that the dominant contribution to the nonlinear response before annealing is coming from lattice-mismatch strain and, after annealing from micro-strain defined by the strain gradient/fluctuations.

3.4.4. The role of film thickness in SHG

In Fig. 3.21, SHG data from samples of three different sets are plotted versus film thickness. It is clear that there is no particular trend between thickness and SHG signal, indicating that submicron changes in film thickness do not have a strong bearing on the nonlinear response of the film. This result also points toward the important role of the interfaces in the nonlinear response of the garnet films. The role of interface in SHG is discussed in detail in the following section 3.4.5.

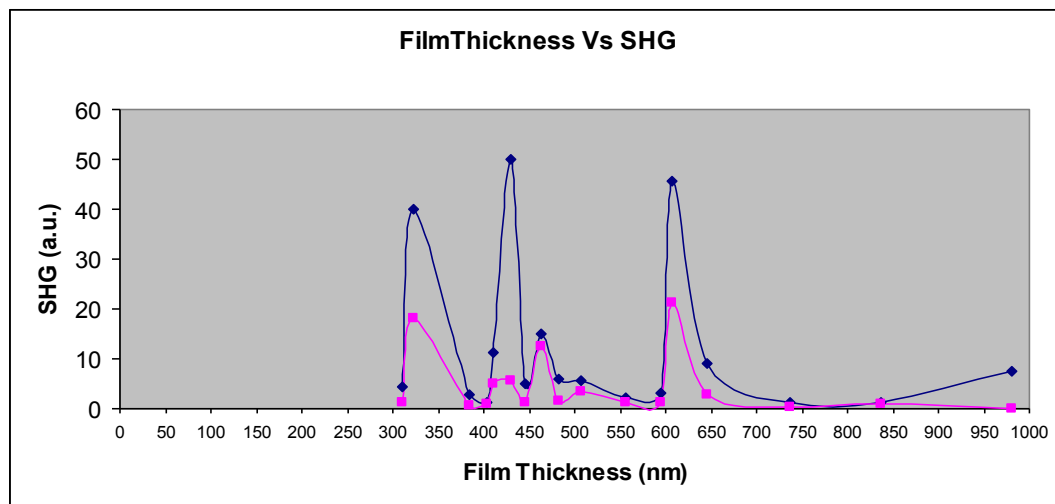


Fig. 3.21. Thickness Vs SHG graph drawn using samples from three different sets, diamonds in blue for PP geometry and square in pink for PS geometry.

3.4.5. The role of interface in SHG

To investigate the role of the interfaces in the nonlinear response of the films, we fabricated a total of eight multilayer films (two in set-3 and six in set-5). These films consisted of different alternating (adjacent) layers sputter-deposited *in-situ* by alternatively facing the sample towards one target or another in the growth chamber. Two targets were used, with compositions $\text{Bi}_{1.5}\text{Lu}_{1.5}\text{Fe}_4\text{Ga}_1\text{O}_{12}$ and $\text{Bi}_{0.8}\text{Y}_{2.2}\text{Fe}_{4.8}\text{Ga}_{0.2}\text{O}_{12}$, yielding adjacent layers under different strain and of different composition. SHG rotational anisotropy plots from four multilayer films are shown in Fig. 3.22.

Almost all multilayer films showed better SHG signal and crystallographic structure compared to single layer films (of larger thickness), deposited under similar conditions. Since each layer in the multilayer films is only ~25 nm thick, a high SHG signal from these thin films strongly indicates that the SHG is coming from the interfaces. We believe that at the interfaces the strain is relatively high due to lattice mismatch between adjacent layers, along with broken crystallographic symmetry and magnetic time reversal symmetry. The role of strain is discussed in detail in the following section 3.4.6.

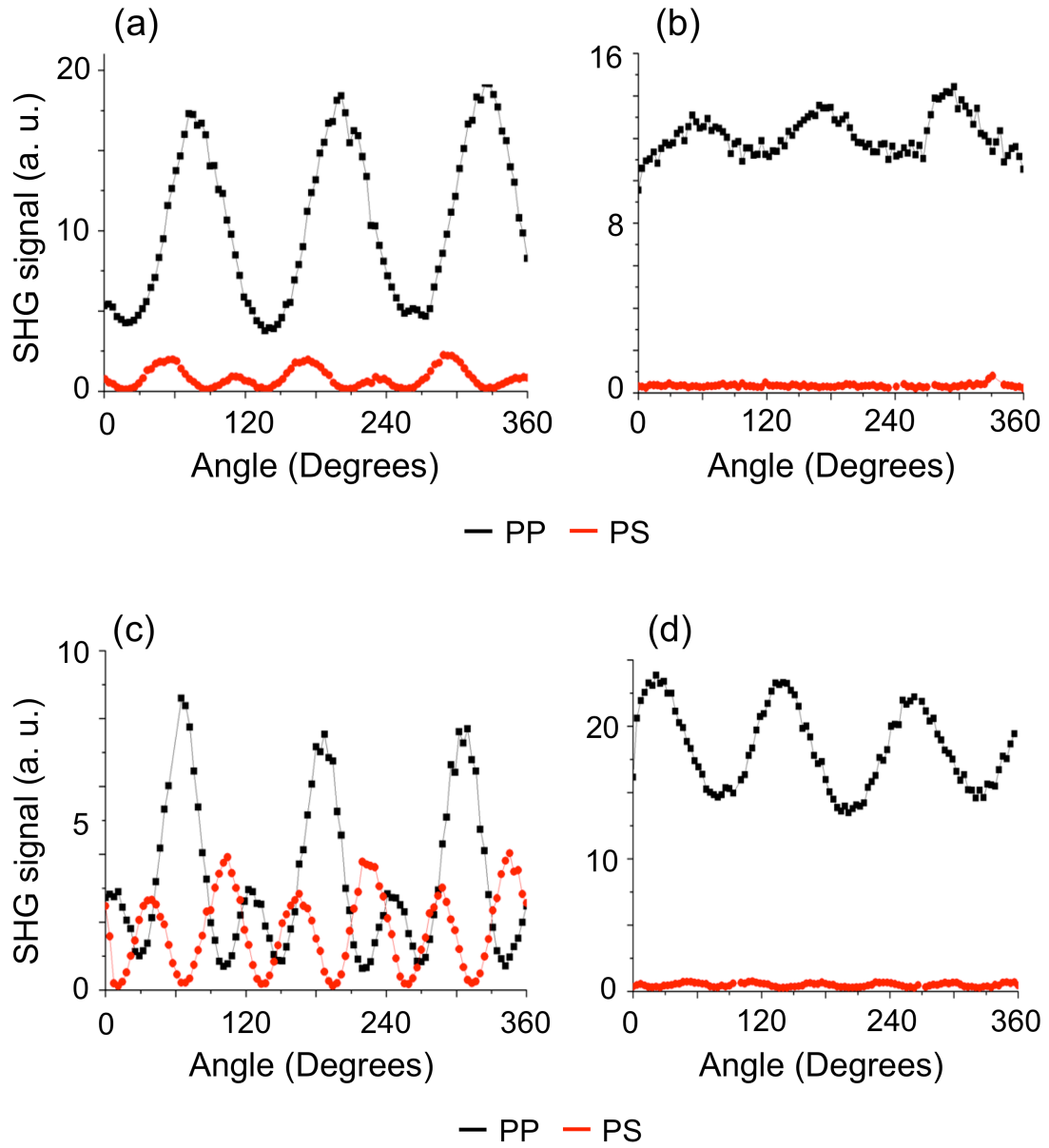


Fig. 3.22. SHG rotational anisotropy of (a) 2-layer, (b) 5-layer, (c) 10-layer, and (d) 15-layer garnet films.

In Fig. 3.23, a comparison between film side illumination and substrate side illumination for a garnet sample is shown. The same level of SHG signal from both sides of the sample strongly indicates that the signal is mostly coming from the interface (since the substrate itself shows negligible SHG as shown in Fig. 3.16).

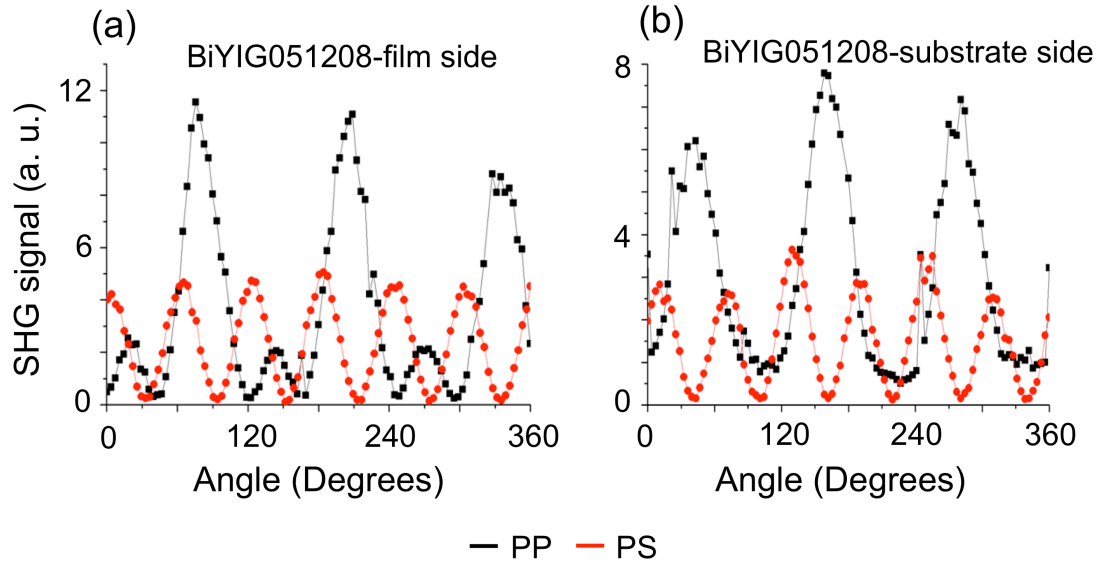


Fig. 3.23. SHG rotational anisotropy measurements of a typical Bi:YIG sample (a) when sample is illuminated from film side, and (b) when sample is illuminated from substrate side.

3.4.6. The role of lattice mismatch, micro-strain, and composition in SHG

In general, sputter deposited films are under strain and subject to stress, mostly controlled by the growth parameters and the lattice mismatch between substrate and film structure. In this section we present results of an in-depth systematic study performed to highlight the role of various strain components, and films' stoichiometric composition in enhancing the SHG response of the magnetic garnet films.

(I) Strain and elemental concentration: - We studied the strain-composition dependence in the Bi:YIG samples. Average elemental concentrations were plotted against the mean micro-strain and lattice mismatch (LM) strain; corresponding plots are shown in Fig. 3.24. It was found that Bi and Y concentrations induce a monotonic relation with LM strain as shown in Fig. 3.24(a), and 3.24(b), while no clear trend with micro-strain is seen in Fig. 3.24(c), 3.24(d). In Figs. 3.25, 3.26 and 3.27, each data point is labeled by its corresponding Bi:YIG sample number as given in column one of Table 3.2.

It was observed that the elements in the dodecahedral sublattice (Bi and Y) of the garnet crystal influence the LM strain. An increase in Bi concentration results in a

decrease in LM strain, while a higher Y concentration strengthens the LM strain, as seen in Fig. 3.24(a), 3.24(b), respectively. Our measurements indicate that the micro-strain value does not show any clear dependence on Bi and Y concentration (see Fig 3.24(c), 3.24(d)).

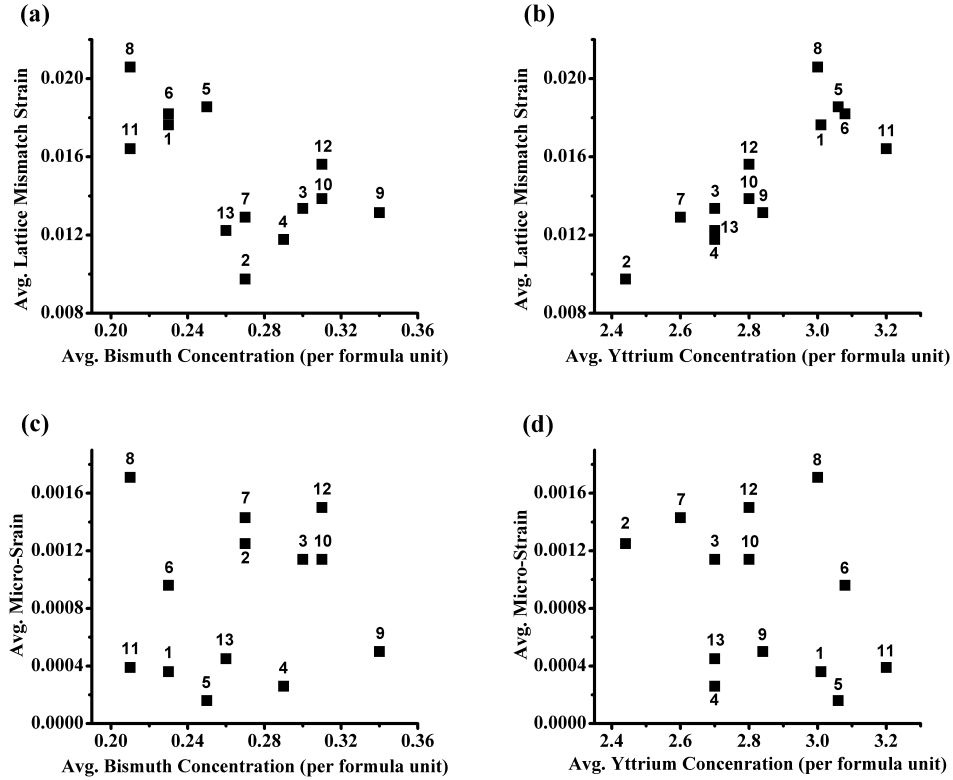


Fig. 3.24. Plot of (a) Bi-concentration Vs LM strain, (b) Y-concentration Vs LM strain, (c) Bi-concentration Vs micro-strain, and (d) Y-concentration Vs micro-strain.

A comprehensive study of the dependence of various elemental compositions on strain value reveals that no interesting trend is seen with gallium, iron and oxygen under the range of elemental concentrations explored in this work. Thus it can be concluded that Bi and Y concentrations from sample to sample produces different LM strain values for each sample; however, variations in these concentrations do not show any orderly influence over the micro-strain value in the film.

(II) SHG and strain: - A detailed theoretical study of the effect of various strain components on SHG in magnetic garnet films has been performed by Lyubchanskii *et al* [21,22]. They predict the contribution of lattice misfit and dislocation strains on SHG, using a nonlinear photoelastic tensor (see Eq. (3.8)). Strain enters into the quadratic nonlinear optical susceptibility tensor via the expression given in Eq. (3.8).

$$\chi_{ijk}^{(2)}(r) = \chi_{ijk}^{(2,0)}(r) + p_{ijklm} u_{lm}(r). \quad (3.8)$$

Where p_{ijklm} and $u_{lm}(r)$ are the nonlinear photoelastic and strain tensors, respectively. The strain tensor $u_{lm}(r)$ is given by Eq. (3.9).

$$u_{lm}(r) = u_{lm}^{(1)}(r)\Theta(h_c - z) + u_{lm}^{(2)}(r)\theta(z - h_c). \quad (3.9)$$

Here $\theta(z)$ is the Heaviside step function; h_c is the critical thickness of the film, it is defined as the thickness above which misfit dislocations will appear and contributes to the nonlinear polarization. $u_{lm}^{(1)}(r)$ and $u_{lm}^{(2)}(r)$ represent the LM and micro-strain components of strain tensor, respectively. Here summation over repeated indices applies.

In this study, the effects of individual strain components as well as of their convolution in the form of sum and product on the film's SHG response were tested experimentally. The Bi:YIG films grown on (111)-oriented GGG substrate are expected to acquire a non-centrosymmetric point group $3m$ (C_{3v}) [23]. This lowering in the symmetry of the film structure is primarily due to the presence of LM strain and Bi concentration gradients in Bi:YIG samples. The non-centrosymmetric structure of the Bi:YIG films manifested by missing inversion centers results in the observed SHG from these samples. Lyubchanskii *et al* proposed theoretically that the p-polarized SHG signal is an indication of the presence of both strain components and depends additively on both contributions [21]. SHG measurements were performed in the absence of an external magnetic field, under near-zero spontaneous magnetization. Under these conditions a crystallographic part to the nonlinear polarization is expected to dominate, as suggested by Eq. (3.7). It was also verified that no significant SHG is produced by the single-crystal GGG and TbGG substrates, so that the measured signal is due to the

presence of the sputtered film only. As seen in Fig. 3.25(a) the SHG response for P-in, P-out polarization combination (PP geometry) for the system of samples in our study shows a monotonic dependence on the average LM strain value, while no obvious dependence on the micro-strain is seen in Fig. 3.25(b). The SHG intensity is normalized to the optical transmittance of the second harmonic wave ($\lambda=400$ nm) in the film, to take into account losses of the SH radiation near film-substrate interface.

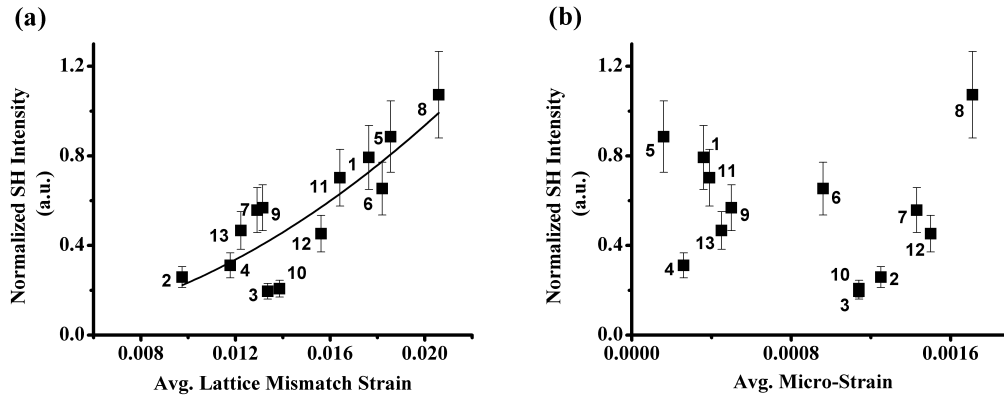


Fig. 3.25. Normalized SHG signal (PP geometry) dependence on (a) the lattice mismatch strain, and (b) the micro-strain. A second power allometric fit to LM strain dependence is plotted in (a) [105].

The clear trend seen in Fig. 3.25(a) implies that the SHG signal strongly correlates with changes in LM strain, while the absence of a monotonic trend with micro-strain in Fig. 3.25(b) suggests that the SHG is less sensitive to strain fluctuations at the level of micro-strain present in the samples under study [105]. The convolution of strain components as their sum shows a slightly degraded but similar trend as that for the lattice-mismatch, with the major contribution coming from the latter. To our knowledge, a strain product convolution is not predicted by theory and does not fit the experimental data well.

Therefore, from Fig. 3.25 it could be said that control of the SHG signal in the set of Bi:YIG samples analyzed in these experiments originates mainly from the lattice mismatch strain. This observation partly abides by the prediction of Ref [21] that both

strain components contribute in SHG. The lower sensitivity of the SHG signal to micro-strain in the film could be attributed to the fact that micro-strain is an order of magnitude smaller than the LM strain. At the same time, the factors engendering micro-strain, such as varying elemental displacement, strain gradients, dislocations, local stresses, etc. might contribute differently and be distributed unevenly in different samples, leading to a random net contribution to the SHG signal.

The plots in Fig. 3.26 give the dependence of SHG on Bi and Y concentration. From the plots it is evident that the normalized SHG signal decreases with increasing Bi concentration, while it increases with an increase in Y concentration.

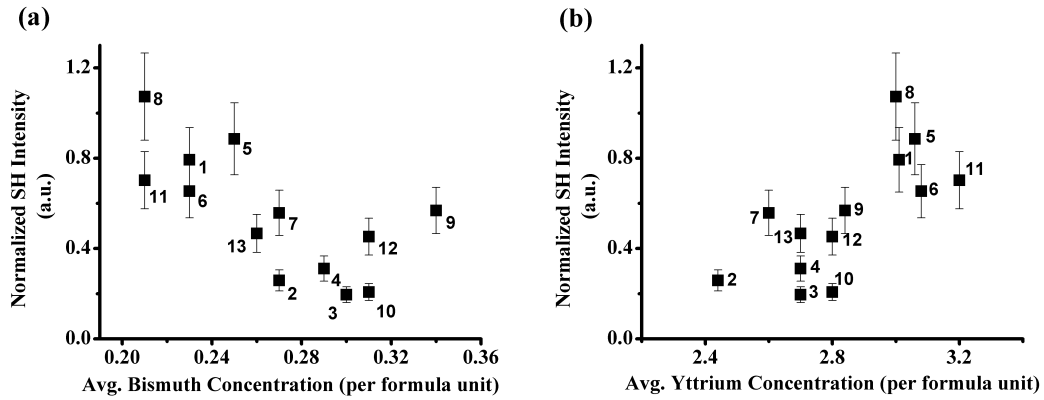


Fig. 3.26. Normalized SHG signal (PP geometry) dependence on (a) the Bi concentration, and (b) the Y concentration.

A clear and strong conclusion can be drawn from Figs. 3.24, 3.25, and 3.26, that the Y concentration in the Bi:YIG film supports the lattice mismatch, which in turn enhances the second harmonic signal in these film, while the Bi concentration acts against the lattice mismatch and results in a weaker nonlinear response in the film. The micro-strain value does not show any interesting trend with the SHG intensity, and neither does it show any dependence on average Bi and Y concentration in the film.

3.4.7. Hyper-Rayleigh scattering (HRS) study

The HRS technique was used here for an experimental study of Bi:YIG films with in-plane inhomogeneities and structural disorders. The experimental setup is shown in Fig. 3.27, where the output of a Ti: Sapphire oscillator with wavelength 800 nm, pulse duration 100 fs, and repetition rate 80 MHz was used as the fundamental radiation. It is focused on a sample at an angle of incidence 45° . The scattered optical radiation passes through a filter, an aperture, a lens, and an analyzer before entering a photo-multiplier tube (PMT). For signal collection at various scattering angles, this detection system could be rotated from 0 to 90 degrees with respect to the sample in the plane of incidence. The scattering polar angle is measured from the normal to the film plane as shown in Fig. 3.27.

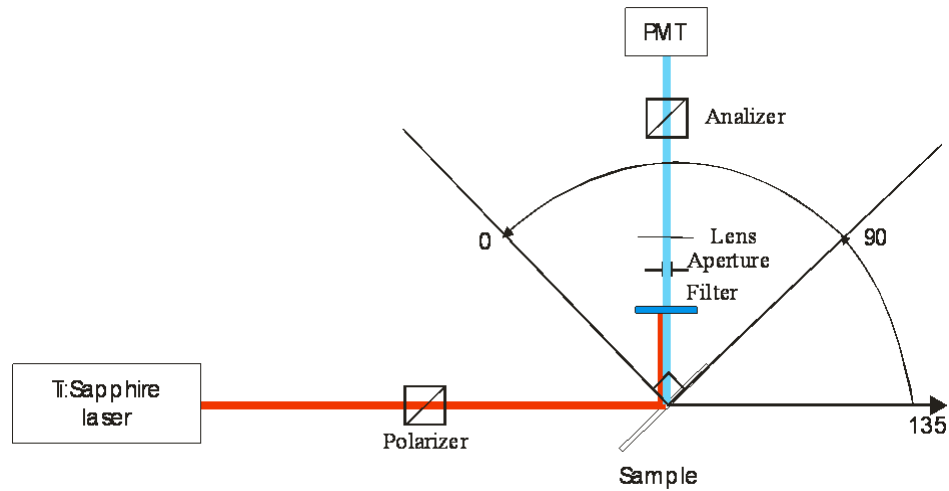


Fig. 3.27. Experimental Setup for HRS measurements

The SHG signal from film consists of coherent (Rayleigh scattering, RS) and incoherent (hyper-Rayleigh scattering, HRS) components [106]. The coherent part of the signal accounts for contributions from the surface/interface roughness and reveals itself in the HRS indicatrix as a narrow specular peak, while the hyper-Rayleigh part which accounts for contribution from the bulk of the film appear as a diffused signal with a broad indicatrix, as shown in Fig. 3.28(a) and 3.28(b), respectively.

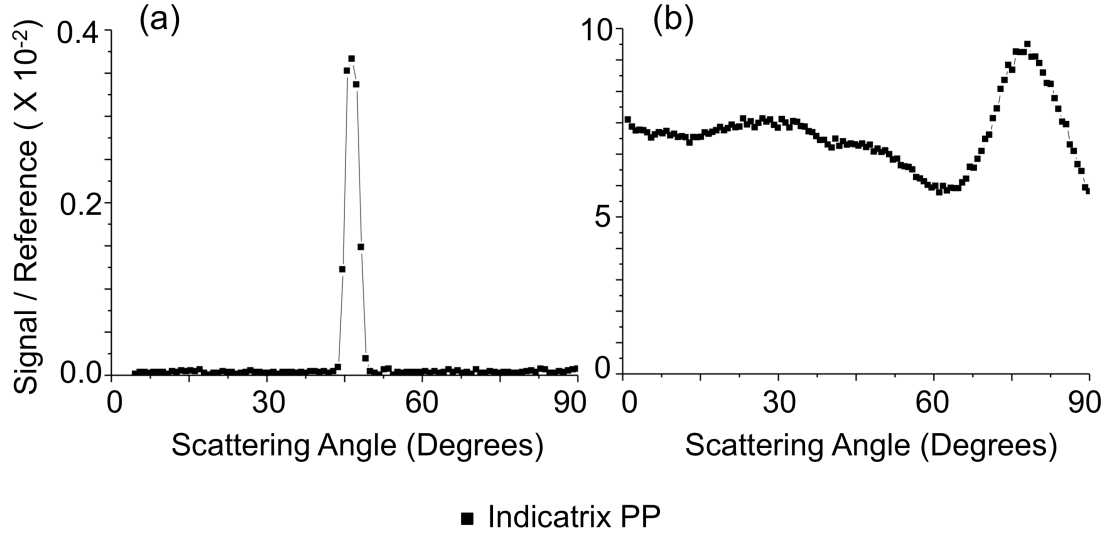


Fig. 3.28. HRS indicatrix of a film with a large lattice mismatch strain (a), narrow RS coherent peak indicate that the SHG signal is mostly coming from the surface/interface. Figure (b) depicts a broad HRS indicatrix for a LPE grown film with zero strain, showing that the film has a strong luminescence and there is no SHG signal.

The HRS study establishes that the lattice mismatch strain drives the SHG signal in the thin garnet films used in the present study, and confirms the role of film-substrate interface studied earlier in this section. The interesting point here is that in our sputtered deposited films there is significant and even dominant non-HRS contributions to the SHG. However, that this does not mean that there is no local inversion symmetry breaking. It only means that the anisotropic dipole quadratic susceptibility does not fluctuate randomly in the film. We know for a fact that the sputtered-deposited samples consist of oriented (epitaxially-grown) crystallites. What this study tells us is that they produce strong non-diffusive SHG, so that there is no (or no significant) random dipole quadratic susceptibility that fluctuates in the plane of the films; and no significant contribution from surface roughness.

3.4.8. Surface effects investigation

As part of our research efforts, and consistent with the goal of this study, we have explored the surface effects as a mean of overcoming the bar against second harmonic generation in Bi:YIG and Bi:LuIG films by patterning the film surface using

photolithography and plasma etching techniques. A schematic of lithograph process steps is shown in Fig. 3.29.

An EVG photolithographic mask-aligner was used to pattern the films surface, followed by an etching process using a Hitachi FB-2000A focused ion beam (FIB) system and a Chemically-Assisted Ion Beam Etching (CAIBE) system. We patterned eleven Bi:YIG samples, two using FIB (see for example Fig. 3.30) and nine using CAIBE. Details of patterned samples is given in Table A1.3 Appendix 1.

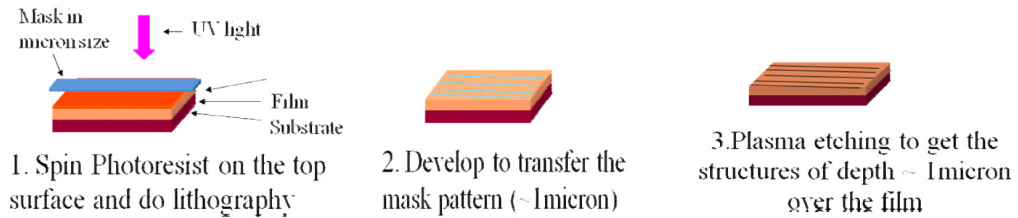


Fig. 3.29. Surface patterning using photolithography and plasma etching techniques.

SHG measurements of these patterned samples were carried out at MSU. It was found that most of the signal got scattered away due to diffraction and scattering of the source light by the patterns (which is of the order of wavelength) and could not be measured.

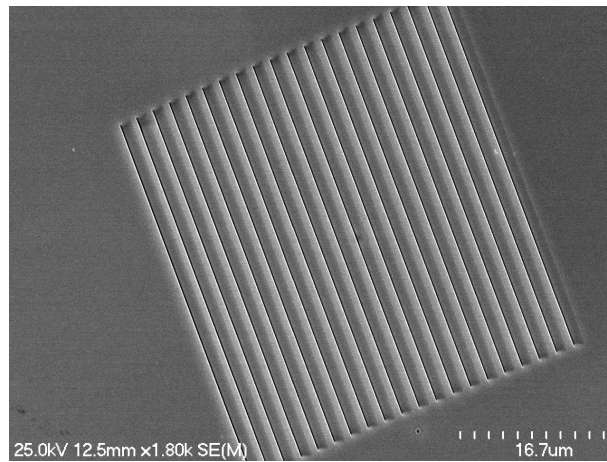


Fig. 3.30. SEM micro-graph of line patterns over Bi:YIG film.

3.5. Summary

- Bi:YIG films were grown with different sputtering parameters and target compositions.
- Films were characterized for crystalline nature using XRD. Index, thickness, transmittance, and Faraday rotation measurements of the films were performed.
- SHG measurements of all the films were done successfully.
- An elaborate study on the role of oxygen, strain, film thickness, substrate, interfaces and annealing process was conducted successfully.
- The SHG signal was found to arise mostly from the interface of the films.
- A detailed study of the second harmonic response as a function of strain in Bi:YIG films shows a strong dependence on lattice mismatch strain. The nonlinear response increases with strain. Bismuth and yttrium concentrations correlate with strain in the material, thus affecting the second harmonic response.
- Sample annealing was found to play an essential role in SHG response. A study performed on a batch of selected samples showed that the dominant contribution to the nonlinear response could be traced to the lattice-mismatch strain for unannealed samples and, to micro-strain for annealed samples.
- Hyper-Rayleigh scattering experiments provided evidence supporting the role of lattice mismatch strain (from film-substrate interface) in the SHG response of garnet thin films and showed a strong non-diffusive SH harmonic contributions from oriented crystallites.
- There is no significant dependence of SHG signal on film thickness.

4. Nonreciprocal and Unidirectional Optical Bloch Oscillations in Asymmetric Waveguide Arrays**

The study of novel nonreciprocal (NR) and unidirectional optical Bloch oscillation (BO) effects constitutes the second major part of this dissertation. These effects were first proposed by Professor Levy and developed by both of us [24,25]. Here we present a detailed analytical study of the NR BO effect in magneto-optic asymmetric waveguide arrays. We extend the idea further and develop the concept of unidirectional BO in technologically important semiconductor substrates with magnetic garnet cover layers. Applications to on-chip isolation and multi-functionality are discussed.

4.1. Introduction and background

We present a rigorous study on a new mechanism for the generation of nonreciprocal and unidirectional optical Bloch oscillations (BOs). Bloch oscillatory motion is a remarkable phenomenon first predicted by F. Bloch and C. Zener in the 1930's consisting of oscillatory trajectories for electrons subject to a uniform electric field in crystal potentials [26,27]. Although optical analogues of electronic BOs have been also observed, as spatial beam oscillations or temporal pulse oscillations [107-112], nonreciprocal and unidirectional photonic BO effects have not been demonstrated experimentally, yet. Their implementation in magneto-optic and hybrid semiconductor media was first proposed and theoretically developed by us [24,25,42].

In recent years, the concept of a discrete optical system exhibiting diffractionless propagation of an optical beam has drawn attention to the possibility of visualizing various intriguing phenomena, such as dynamic localization and Bloch oscillations. The present study provides a comprehensive theoretical basis for the realization of nonreciprocal and unidirectional optical BOs in a chirped waveguide array structure.

** The material contained in this chapter has been published in three *Optics Letters* articles. For detailed citation, see reference [24], [25], and [42].

We develop model systems consisting of one-dimensional photonic crystal waveguide arrays in magnetic garnet and silicon platforms to demonstrate the proposed phenomena. An optical force is introduced into the array via geometrical design diverting the beam sideways. Laterally displaced photons are periodically returned to a central guide by photonic crystal action. The effect leads to novel oscillatory optical phenomena that can be magnetically controlled and rendered unidirectional.

We show that the normal modes (or supermodes) of the coupled one-dimensional waveguide array exhibit nonreciprocal propagation upon transverse magnetization to the propagation direction. The non-reciprocity of these eigenstates of the system leads to nonreciprocal Bloch oscillatory motion, though under conditions of approximate phase matching in opposite propagation directions. By embedding the system in a magneto-optic medium we demonstrate the possibility of optical modes analogous to Wannier-Stark states in electronic BO case [29], but possessing distinct properties upon propagation direction reversal. The presence of non-reciprocity in the array structure allows for nonreciprocal normal-mode dephasing and the possibility of unidirectional BOs.

Beyond fundamental studies, the nonreciprocal and unidirectional BO phenomena offer potential applications in magneto-optically controlled all-optical systems. The unidirectionality of the Bloch oscillatory phenomenon can be used for optical isolation purposes. Isolators are critical components that provide source stability in optical circuits by blocking out back-reflected light. At the same time, through the unidirectional BO effect, the same isolator device can perform as a fast optical switch via magnetization reversal, turning off the forward beam. Routing, a critical function in signal processing, can be performed by adjusting lateral beam spread through electro-optic control [33]. The output of the present dissertation work has the potential to strongly impact optical communications and data processing by enabling compact integration, fast switching, and insertion loss minimization. Moreover, by overcoming serial integration it takes an important step towards cost reductions in photonic circuit technology.

In the following subsections, we provide brief descriptions on some related basic concepts required for a clear understanding of the novel nonreciprocal effects under study. We start with an overview on the Bloch oscillations phenomena and then summarize some basic elements of waveguide theory.

4.1.1. An overview on Bloch oscillation phenomena

Around 1930 F. Bloch and C. Zener originally came up with the intriguing concept of Bloch oscillations (BO), comprising oscillatory motion of quantum particles in a periodic potential subject to constant external force [26,27]. Their analytical study of BO effect consists of electrons driven by an external electric field force in a crystal (see Fig. 4.1). They proposed an unusual dynamics for the electronic motion based on then newly developed quantum mechanics, and emphasized that these elementary charge particles should exhibit a periodic oscillatory motion with period $T_B = h/(eEa)$, where e is electronic charge, E is the electric field amplitude, a is the lattice parameter, and h is the Planck constant, rather than uniform motion. However, this oscillatory motion of electrons had never been observed in natural crystals because the scattering time of the electrons by the crystal defects was much shorter than the Bloch period T_B [28]. As a result, the existence of the BO phenomenon was controversial for a long period of time [28].

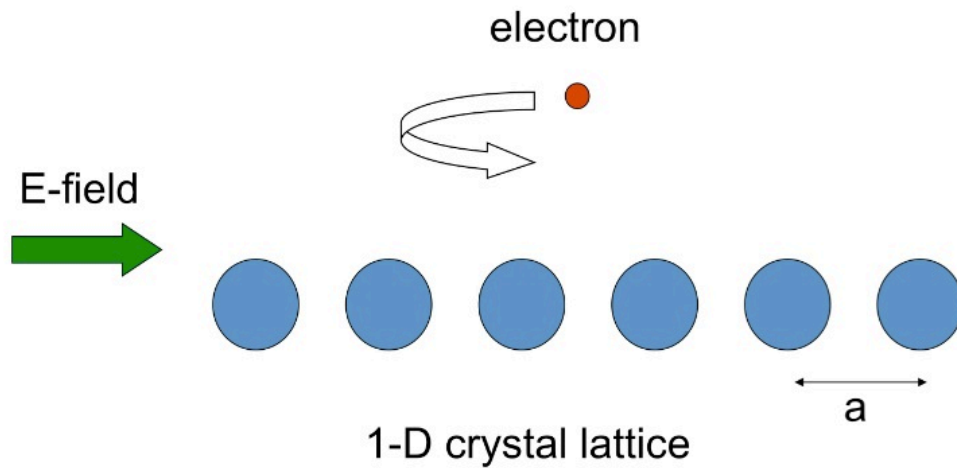


Fig. 4.1. Schematic representation of electronic BO motion in a crystal.

The first experimental proof confirming BO came in 1960 when Chynoweth et. al. observed an evenly spaced discrete energy spectrum, so called Wannier-Stark ladder, for electrons in a crystalline medium placed in an external electric field [29]. Thereafter a number of theoretical and experimental studies showing similar non-classical behavior in different particle systems such as electrons in semiconductor superlattices, cold atoms in optical lattices and electromagnetic waves in periodic dielectric systems have been reported [30-32]. Recently, the concept of a discrete-optical system exhibiting diffraction-less motion of an optical beam has drawn attention to the possibility of visualizing the oscillatory motion in the spatial domain with controlled beam dynamics [33-38].

To understand the BO effect, one must realize that in a periodic potential the motion of a particle, such as an electron in a regular crystal or a photon in a photonic crystal, is governed by a dispersion law that relates the wave-vector and the energy of the particle (see Fig. 4.2). Under the application of a uniform and time-constant force, such as the force induced by a constant electric field on an electron in a crystal or propagation-constant gradient on a photon in a photonic crystal, the wave-vector and the kinetic energy of a (collision-less) particle increase in magnitude along the band, as shown in Fig 4.2. In contrast to free-space accelerated motion, under the influence of this force, the particle in an energy band is first accelerated and then slowed down as it reaches the top of the energy band. Under the continued influence of the original force, i.e. without a reversal in the direction of the force, the particle would then reach the boundary of the first Brillouin zone and reverse direction as its group velocity (the slope of the curve) changes sign, retracing its steps and reaching the bottom of the energy band.

Over the last decade there has been a strong interest in Bloch oscillations, particularly in optical systems. Bloch oscillations become effective for particles in accelerating periodic potentials and are therefore also observable for photons in optical lattices with linearly varying effective mode indices. The first experimental observation of optical Bloch oscillations was done in an array of coupled waveguides [33]. Since then a significant number of publications have reported on both classical and non-classical optical Bloch oscillations in waveguide arrays [35-38]. However, these studies were

restricted to the reciprocal BO effects. S. Longhi has explored nonreciprocal Bloch oscillations in active media [113], while K. G. Makris and co-workers have studied the nonreciprocity of Floquet-Bloch modes in PT symmetric optical lattices with the help of gain and loss [114]. We were the first to propose and demonstrate theoretically nonreciprocal and unidirectional optical BO in passive gain-less media, as well as in magneto-optic media [24,25].

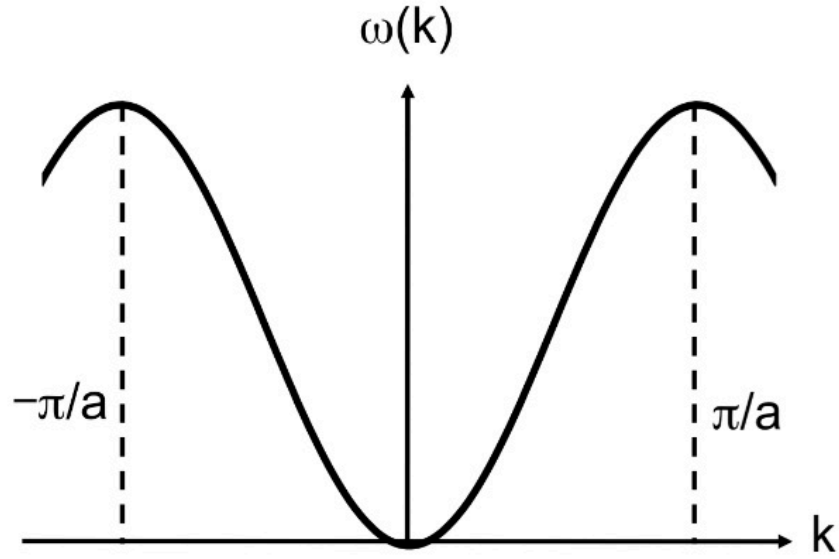


Fig. 4.2. Dispersion curve for a particle in a periodic potential.

4.1.2. Beam dynamics in a dielectric waveguide

In this section, the concept of optical modes in a dielectric waveguide structure is discussed, and key results of waveguide theory are presented.

Dielectric waveguides serve as the basic building blocks in modern integrated optics. They carry the optical signals from one part to another part in a photonic circuit. Optical signals in these structures travel in the form of distinct modes. A mode describes the spatial distribution of optical energy in one or more dimensions that remains constant in time [103].

A planar dielectric waveguide comprises three layers, namely, substrate, core, and cover, as shown in Fig. 4.3. For waveguiding in the structure, material indices of three layers should satisfy the following relation (Eq. (4.1)):

$$n_f > n_s > n_c \quad (4.1)$$

Additionally, the guiding (core) layer thickness (T) should be above a critical thickness, which is generally of the order of the optical wavelength (λ).

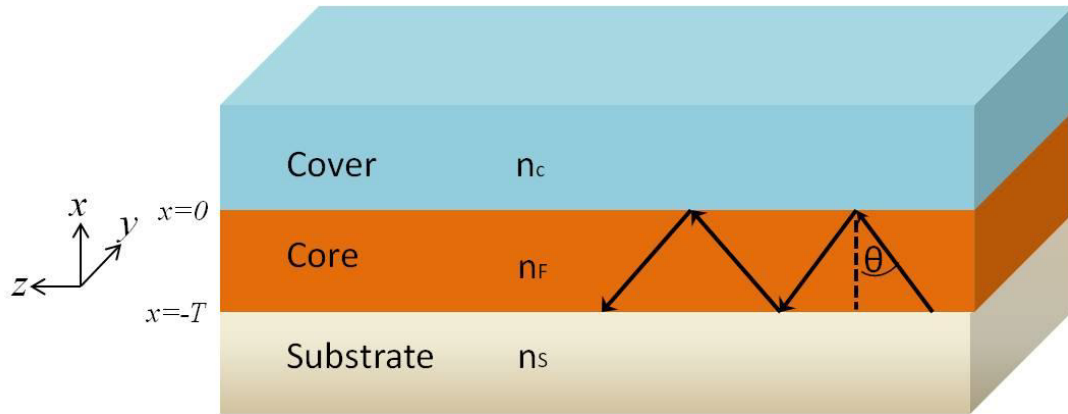


Fig. 4.3. Schematic of a planar (slab) waveguide structure.

The optical beam is mostly confined in the core layer of the waveguide, by total internal reflection phenomenon, with infinitesimal evanescent tails in the cover and substrate regions. Schematic in Fig. 4.3 represents a two-dimensional (2-D) optical slab waveguide, where the light is restricted only in the x -direction. Since the light is bounded in one direction only, the propagating modes of slab waveguide undergo diffraction in the lateral (y) direction. A 2-D slab waveguide provides an excellent platform for qualitative understanding of the waveguide concept, but it finds very limited device applications. These waveguides can be fabricated by depositing a thin-film on a slightly low index substrate (e.g. Bi:YIG on GGG).

More efficient confinement can be achieved in a three-dimensional (3-D) ridge waveguide structure, where the light is bounded from two sides (i.e. in both x -, and y -directions), as shown in Fig. 4.4. In a ridge waveguide, optical modes are mostly confined in the ridge part of the waveguide, defined by the width W and thickness T (see

Fig. 4.4). These structures are generally used as interconnects in optical circuits; additionally, they serve as the basic elements for building various on-chip optical devices, such as directional coupler, switches, modulators, and isolators. Typically, micro-fabrication techniques are used to fabricate 3-D ridge waveguide structures.

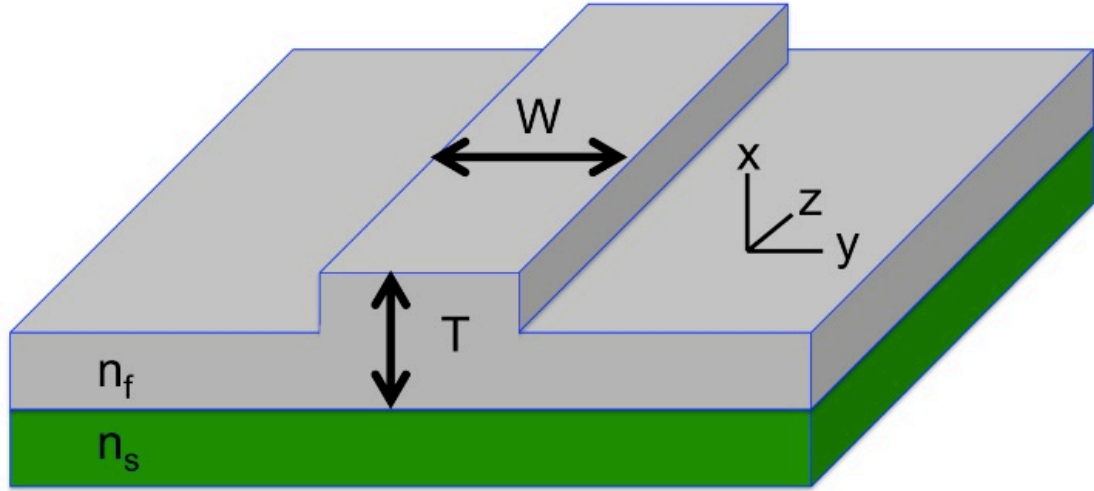


Fig. 4.4. Schematic of a ridge waveguide with air cover.

(I) Guided modes [103]:

Consider the simple three-layer planar waveguiding structure of Fig. 4.3. Now, using the ray-optics method we calculate the guided modes of this structure. For a beam propagating in the waveguide, the critical angles at core-cover (θ_c) and core-substrate (θ_s) interfaces can be given by,

$$\theta_c = \sin^{-1}(n_c / n_f) \quad (4.2)$$

$$\theta_s = \sin^{-1}(n_s / n_f) \quad (4.3)$$

For an optical beam profile to become the guided mode of the waveguide, the incidence angle (θ) of the beam should satisfy the following condition,

$$\theta_s < \theta < 90^\circ \quad (4.4)$$

The light is confined in the guiding layer by total internal reflections at the two interfaces. When $\theta_c < \theta < \theta_s$, light remains bounded from cover side, however it leaks into the substrate following the Snell's law.

From the wave-optical point of view, the propagation constants along the longitudinal (k_z), and transverse (k_x) directions are given by (see Fig. 4.5),

$$k_z = k_0 n_f \sin \theta = \beta \quad (4.5)$$

$$k_x = k_0 n_f \cos \theta \quad (4.6)$$

Where $k_0 = 2\pi / \lambda$, is the free space wavenumber.

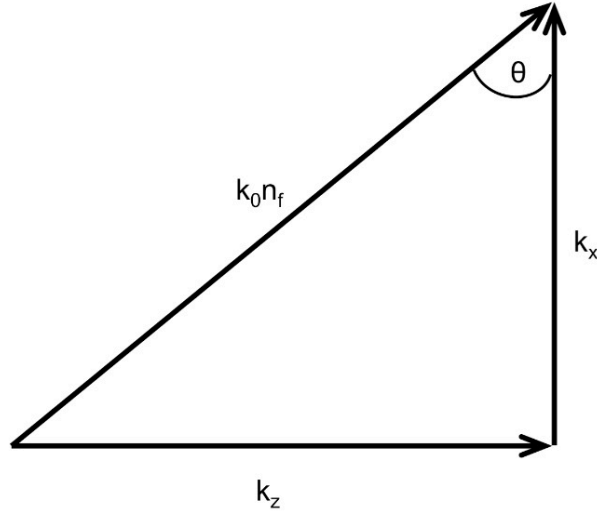


Fig. 4.5. Wave-vector representation, showing the wave-vector in longitudinal (k_z), and transverse (k_x) directions.

In terms of effective indices (N), the propagation constant is defined as,

$$\beta = k_0 N, \text{ where } N = n_f \sin \theta \quad (4.7)$$

The guided mode condition (Eq. (4.4)) in terms of N becomes,

$$n_s < N < n_f \quad (4.8)$$

The substrate and clad (cover) radiation modes exist when $N < n_s$.

(II) Wave Equations:

Wave equation in an isotropic, lossless dielectric medium can be derived from the following Maxwell's equations:

$$\nabla \times \bar{E} = -\mu_0 \frac{\partial \bar{H}}{\partial t} \quad (4.9)$$

$$\nabla \times \bar{H} = \epsilon_0 \epsilon \frac{\partial \bar{E}}{\partial t} \quad (4.10)$$

Here, ϵ_0 = Dielectric permittivity of free space.

μ_0 = Magnetic permeability of free space.

ϵ = Dielectric permittivity of the medium.

$\bar{E}, \bar{H} \rightarrow$ Electric field and Magnetic field components of the optical beam, respectively.

The simplest kinds of modes in free space or in an optically homogeneous medium are described by the plane waves. Consider, a uniform plane wave propagating in the z direction in the slab waveguide of Fig. 4.3, i.e.

$$\bar{E} = \bar{E}(x, y). \exp[(\omega t - \beta z)j] \quad (4.11)$$

$$\bar{H} = \bar{H}(x, y). \exp[(\omega t - \beta z)j] \quad (4.12)$$

Here, $\omega = 2\pi c / \lambda$ = Angular frequency of the optical wave.

c = Velocity of the light in free space. $j = \sqrt{-1}$.

The solutions of Maxwell's wave equation give the optical field profiles supported by the waveguide structure; these transverse field patterns are called the normal modes (or eigenstates) of the structure. On solving Eq. (4.9) and (4.10), one obtains two different types of modes with mutually perpendicular polarizations, namely, the transverse electric (TE) and transverse magnetic (TM) modes.

(III) TE mode equation:

The TE mode equation is given by,

$$\frac{\partial^2 E_y}{\partial x^2} + (k_0^2 n^2 - \beta^2) E_y = 0. \quad (4.13)$$

Here the nonzero components of the fields are E_y , H_x , and H_z

$$H_x = -\frac{\beta}{\omega \mu_0} E_y, \quad H_z = -\frac{1}{j\omega \mu_0} \frac{\partial E_y}{\partial x}. \quad (4.14)$$

(IV) TM mode equation:

The TM mode equation is given by,

$$\frac{\partial^2 H_y}{\partial x^2} + (k_0^2 n^2 - \beta^2) H_y = 0. \quad (4.15)$$

Here the nonzero components of the fields are E_x , H_y , and E_z

$$E_x = \frac{\beta}{\omega \epsilon \epsilon_0} H_y, \quad E_z = \frac{1}{j\omega \epsilon \epsilon_0} \frac{\partial H_y}{\partial x}. \quad (4.16)$$

(V) Dispersion relations: Now let us look at the dispersion behavior of TE and TM modes in a slab waveguide. The field solutions of wave equation for the TE modes (Eq. (4.13)), in three different layers (i.e. cover, core, and substrate) of the waveguide can be given by,

$$\begin{aligned} E_y &= E_c \cdot \exp(-\gamma_c x), & x > 0, & \quad (\text{cover}) \\ E_y &= E_f \cdot \cos(k_x x + \phi_c), & -T < x < 0, & \quad (\text{core}) \\ E_y &= E_s \cdot \exp\{\gamma_s (x + T)\}, & x < -T, & \quad (\text{substrate}) \end{aligned} \quad (4.17)$$

Where $k_x = k_0 \sqrt{n_f^2 - N^2}$, $\gamma_s = k_0 \sqrt{N^2 - n_s^2}$, and $\gamma_c = k_0 \sqrt{N^2 - n_c^2}$

The boundary conditions at the interface at $x = 0$, (i.e. E_y and H_z are continuous), gives,

$$E_c = E_f \cos \phi_c, \quad \tan \phi_c = \gamma_c / k_x \quad (4.18)$$

And at $x = -T$, gives,

$$E_s = E_f \cos(k_x T - \phi_c), \tan(k_x T - \phi_c) = \gamma_s / k_x \quad (4.19)$$

Using the Eqs. (4.18) and (4.19), the TE mode dispersion relation can be given by,

$$k_x T = (m + 1)\pi - \tan^{-1}(k_x / \gamma_s) - \tan^{-1}(k_x / \gamma_c) \quad (4.20)$$

In a similar way, the following TM mode dispersion relation can be obtained from the Eq. (4.15),

$$k_x T = (m + 1)\pi - \tan^{-1}\left\{(k_x / \gamma_s)(n_s / n_f)^2\right\} - \tan^{-1}\left\{(k_x / \gamma_c)(n_c / n_f)^2\right\} \quad (4.21)$$

In the two dispersion relations, $m = 0, 1, 2, \dots$, represents the mode number.

For a given material system the dispersion characteristics of the TE and TM mode modes can be calculated from Eqs. (4.20), and (4.21).

(VI) An example of TE and TM mode calculation: Consider a Ce:YIG thin film on a GGG substrate with following parameters: film index (n_f) = 2.22, substrate index (n_s) = 1.95, wavelength = 1550 nm. Using the TE and TM dispersion relations, we obtain the thickness versus effective modes graph, shown in Fig. 4.6. From the graph, we find that a micron thick Ce:YIG will support one TE and one TM mode. When the film thickness is increased to three microns, the number of guided modes becomes eight (four TE and four TM).

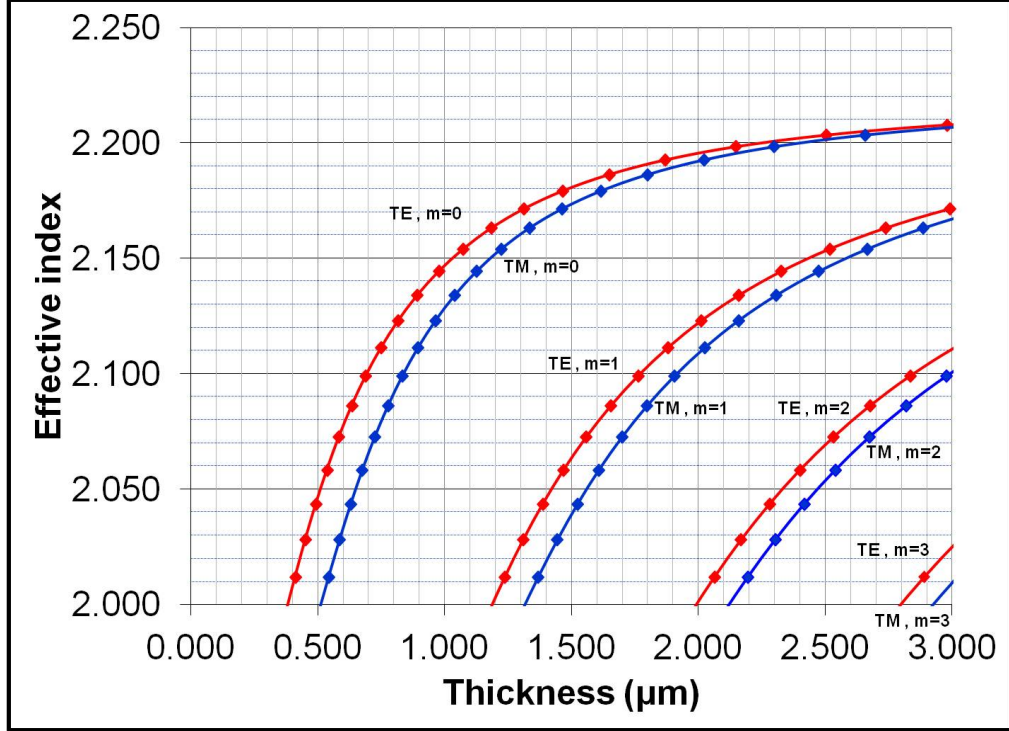


Fig. 4.6. Calculated TE and TM modes for Ce:YIG/GGG slab structure. The graph shows that a micron thick film supports only one TE and one TM mode.

4.2. Analytical study

This section comprises an analytical proof of the existence of nonreciprocal and unidirectional optical BO in an asymmetric waveguide array. A key role is played by the TM mode nonreciprocal phase shift (NRPS) effect, which is due to the confinement of light in transversely magnetized asymmetric waveguides lacking spatial inversion symmetry. This NRPS effect critically depends on the introduction of unequal spatial gradients in both the gyrotropy parameter and the material index across dissimilar waveguide interfaces [115]. A brief background on the origin of NRPS effect in waveguides is provided in section (4.2.1). Nonreciprocal and unidirectional optical Bloch oscillations are induced in one-dimensional photonic crystal waveguide arrays; a thorough study of these two topics is compiled in section (4.2.2) and (4.2.3), respectively. We show that the unidirectionality of the optical BO phenomenon achievable in a magneto-optic asymmetric waveguide array can be used to achieve on-chip optical isolation, a technologically important function in photonic integrated

circuits. This novel technique of on-chip isolation, along with potential multifunctional capabilities is described in section (4.2.4).

4.2.1. Nonreciprocal phase shift (NRPS) effect

Upon transverse magnetization in magneto-optic waveguides an interesting phenomenon arises, known as the nonreciprocal phase shift (NRPS) effect [116,117]. This effect is due to light confinement in magnetized waveguides lacking in spatial inversion symmetry. In an in-plane transversely-magnetized waveguide structure, the propagation constant or wave-vector acquires different values in the forward (FW) and backward (BW) propagation directions, as described schematically in Fig. 4.7 [118,119].

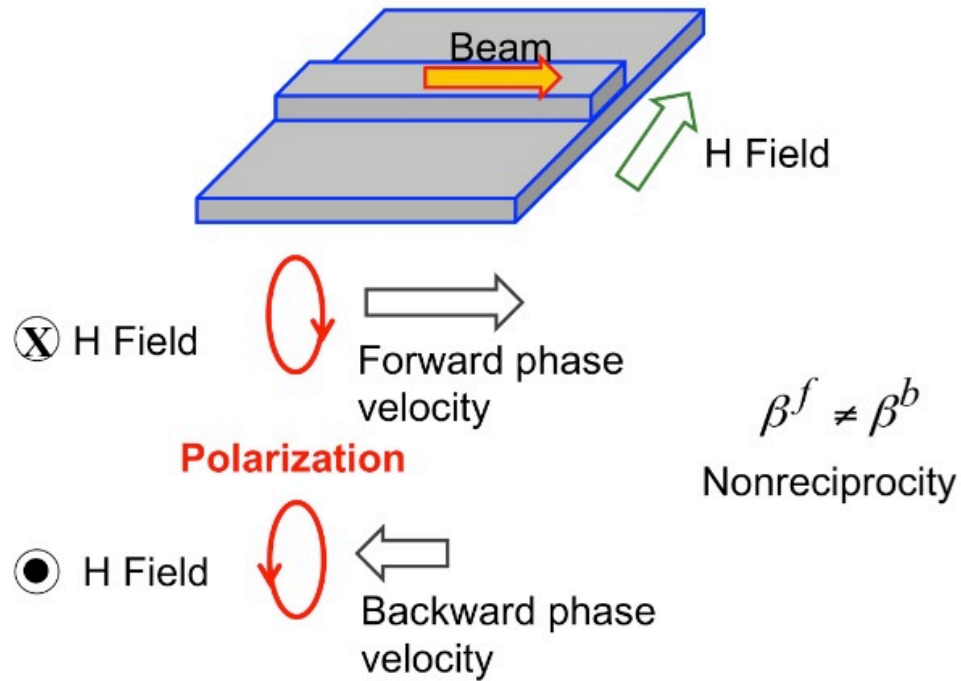


Fig. 4.7. Schematic demonstration of the nonreciprocity for TM waves.

This nonreciprocal effect is unique to waveguide magnetic media: it does not occur in the bulk. It is induced by the coupling between transverse and longitudinal optical electric field components of the polarization caused by the magneto-optic gyrotropy. In a

waveguide a longitudinal component of the optical electric field is allowed, as for example in transverse-magnetic (TM) modes.

This effect has been widely explored for optical isolator applications in waveguide media [118-120]. Recent work by other authors has focused on the NRPS effect in silicon-on-insulator (SOI) waveguides with magnetic cover layers [59,60]. These structures induce a stronger NRPS than magnetic-garnet-core waveguides, making them extremely appealing for integrated optics applications. The enhancement results from the higher refractive index contrast between core and cladding in SOI, a parameter that affects the magnitude of the NRPS [59,60]. A more extensive discussion of the NRPS effect as it applies to structures of interest to this study is provided in the following sections.

4.2.2. Nonreciprocal BO in magneto-optic waveguide arrays

Unlike recent treatments of optical BOs in PT symmetric optical lattices that consider nonreciprocal phenomena as a result of gain, loss, or gain-loss modulation [30-32], in this study we show that it is possible to achieve nonreciprocity without gain or loss in magneto-optic waveguide arrays with asymmetric vertical gradients in the gyrotropy parameter. Unequal propagation constants (spectral asymmetry) and different Bloch oscillatory periods in opposite propagation directions are analytically demonstrated for in-plane transversely-magnetized asymmetric waveguide arrays with linearly growing effective index.

To acquire a deep understanding of the subject, this section is divided in to following three parts:

- (I) TM mode propagation in a gyrotropic waveguide
- (II) TM mode propagation in an asymmetric waveguide array
- (III) Numerical and simulation results of nonreciprocal BO effect

(I) TM mode propagation in a gyrotropic waveguide:

Nonreciprocal devices, such as isolators, either rely on TE-TM mode conversion (result of the Faraday effect) or on differential NRPS effect of TM mode. While the former technique requires precise phase matching in TE and TM modes, the latter method calls for a rather large differential NRPS for practical applications. Recent efforts have moved in the direction of finding schemes to enhance the strength of the TM mode NRPS effect [121,122]. In the present study, we utilize TM mode NRPS to observe nonreciprocal and unidirectional BO phenomena.

We now derive TM mode equation in a gyrotropic medium. Consider the ridge waveguide structure of Fig. 4.8. The dielectric tensor of the guiding layer (made of gyrotropic material e.g. Bi:YIG or Ce:YIG) is given by,

$$\hat{\epsilon} = \begin{pmatrix} \epsilon & 0 & ig \\ 0 & \epsilon & 0 \\ -ig & 0 & \epsilon \end{pmatrix}, \quad (4.22)$$

where ϵ is the isotropic dielectric constant and g is the gyrotropy parameter.

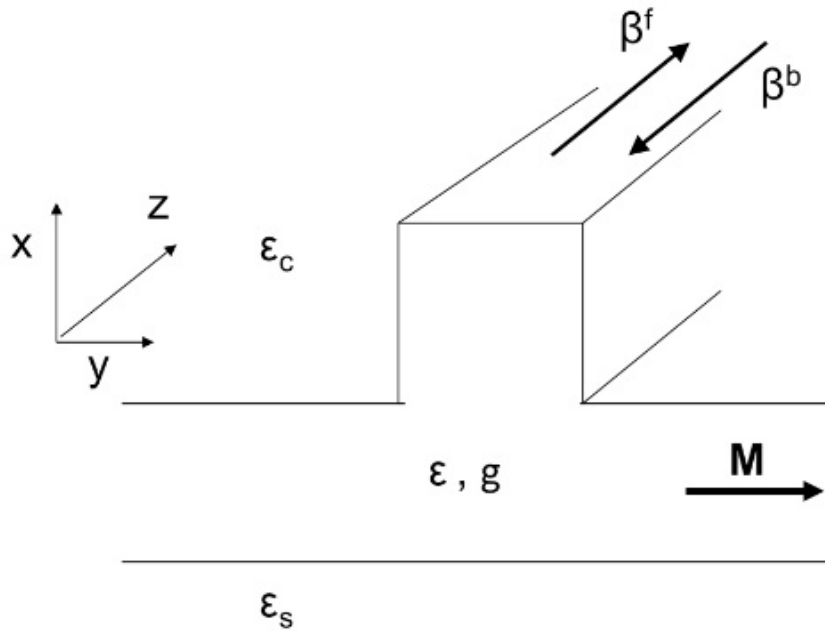


Fig. 4.8. Schematic of a ridge waveguide.

Assuming a time dependent plane wave propagation, and $\mu = 1$ at optical frequencies, Maxwell's equations for this system can be given by [116],

$$\nabla \times \bar{E} = -\omega\mu_0\bar{H}, \quad \nabla \cdot \hat{\epsilon}\bar{E} = 0 \quad (4.23)$$

$$\nabla \times \bar{H} = i\omega\epsilon_0\hat{\epsilon}\bar{E}, \quad \nabla \cdot \bar{H} = 0 \quad (4.24)$$

Taking one more time curl of the above equations gives the wave equations for electric (\bar{E}) and magnetic field (\bar{H}) components of the optical field.

$$\nabla^2 \bar{E} - \nabla(\nabla \cdot \bar{E}) + \omega^2\mu_0\epsilon_0\hat{\epsilon}\bar{E} = 0 \quad (4.25)$$

$$-\hat{\epsilon}\nabla \times (\hat{\epsilon}^{-1}\nabla \times \bar{H}) + \omega^2\mu_0\epsilon_0\hat{\epsilon}\bar{H} = 0 \quad (4.26)$$

Since we are interested in the TM mode only, we will continue the rest of the formulation with the wave equation for TM mode i.e. Eq. (4.26). Note that the dielectric tensor $\hat{\epsilon}$ and gyrotropy g are spatially-dependent along the x-direction. In the next equation we give the final form of the TM mode equation, for intermediate steps see Appendix 4. Specializing to modes that propagate in the z-direction ($\sim \exp(i\beta z)$) and assuming quasi-TM modes ($H_y \gg H_x, H_z$), one obtains the following partial differential equation for TM modes:

$$\left(\epsilon \frac{\partial}{\partial x} \frac{1}{\epsilon} \frac{\partial}{\partial x} + \frac{\partial^2}{\partial y^2} - \beta^2 + \omega^2\mu_0\epsilon_0\epsilon - \beta \frac{g}{\epsilon} \frac{\partial}{\partial x} + \beta\epsilon \frac{\partial}{\partial x} \frac{g}{\epsilon^2} \right) H_y = 0 \quad (4.27)$$

Notice the presence of linear terms in the propagation parameter β in Eq. (4.27). These linear terms add up to $\beta\epsilon H_y \frac{\partial}{\partial x} \frac{g}{\epsilon^2}$ yielding a net nonreciprocal effect if the vertical gradients $\frac{\partial}{\partial x} \frac{g}{\epsilon^2}$ at the substrate/core and core/cover interfaces are different. The change in propagation constant between forward and backward directions ($\Delta\beta^{(nr)} = \beta^f - \beta^b$) for waveguide modes is given in perturbation theory by,

$$\Delta\beta^{(nr)} = \frac{2 \operatorname{Re} \iint dx dy (\partial_x H_y) H_y^* (ig / \epsilon^2)}{\iint dx dy |H_y|^2 \epsilon^{-1}}. \quad (4.28)$$

Where the superscript *nr* stands for non-reciprocal [115].

This kind of optical response is observable in magnetic garnet waveguides, such as bismuth- and/or rare-earth-substituted iron garnets (Bi:IG, RE:IG) films over gadolinium gallium garnet (GGG) substrates. Normally micron-scale-thick films of these materials are fabricated by liquid-phase-epitaxy or RF sputter-deposition on GGG substrates. Refractive index values can be tuned by controlling the bismuth and rare-earth substitution levels, and by partial gallium or aluminum ion-substitution of the iron ions in the garnet tetrahedral site. The strength of the nonreciprocal phase shift effect and its thickness dependence can be regulated by the index contrast between film and substrate and film and cover layer. Fig. 4.9 shows a calculated nonreciprocal propagation constant difference between forward and backward directions as a function of ridge-waveguide thickness for a gyrotropic slab waveguide structure.

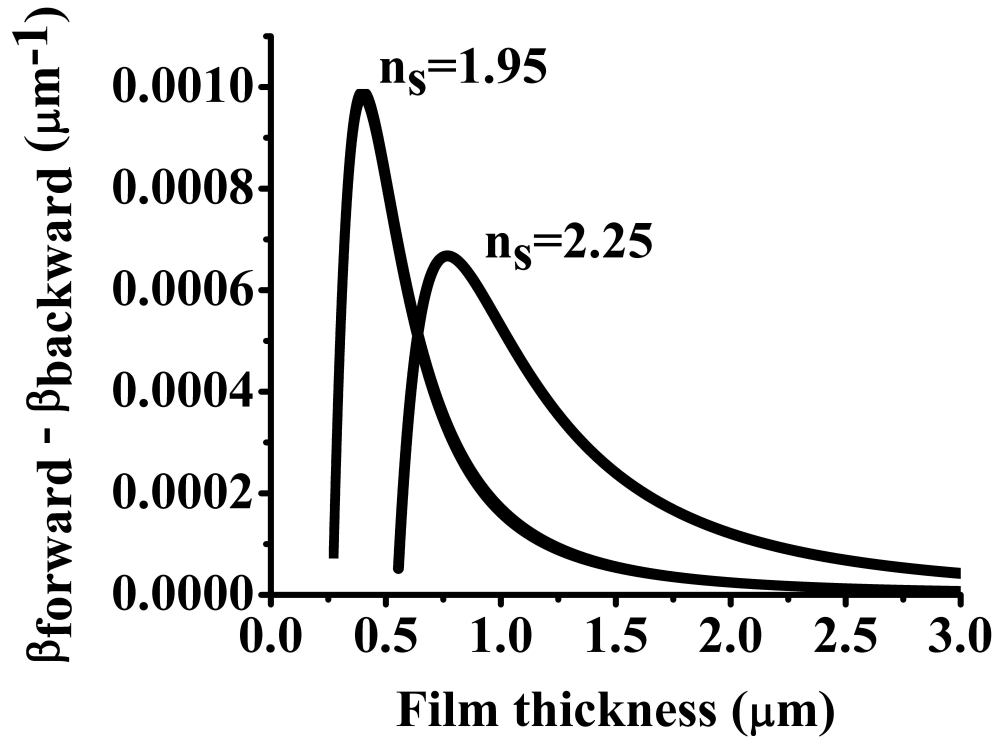


Fig. 4.9. Calculated $\Delta\beta = \frac{2\pi}{\lambda} \Delta n$ between FW and BW directions as a function of ridge-waveguide thickness. The figure displays plots for two substrate indices n_s (1.95, 2.25) and the same waveguide film index of 2.35. Note the shift in peak position and height with substrate index.

A comparison study between NRPS effect of ridge structure with corresponding planar waveguide structure for Ce:YIG over SOI material system is shown in Fig. 4.10. Ce:YIG/SOI waveguide schematic and a table containing the $\Delta\beta^{nr}$ for slab and ridge structures is given in Fig. 4.11. A MATLAB code used for the calculation of differential NRPS of Fig. 4.10 is attached in Appendix 5.

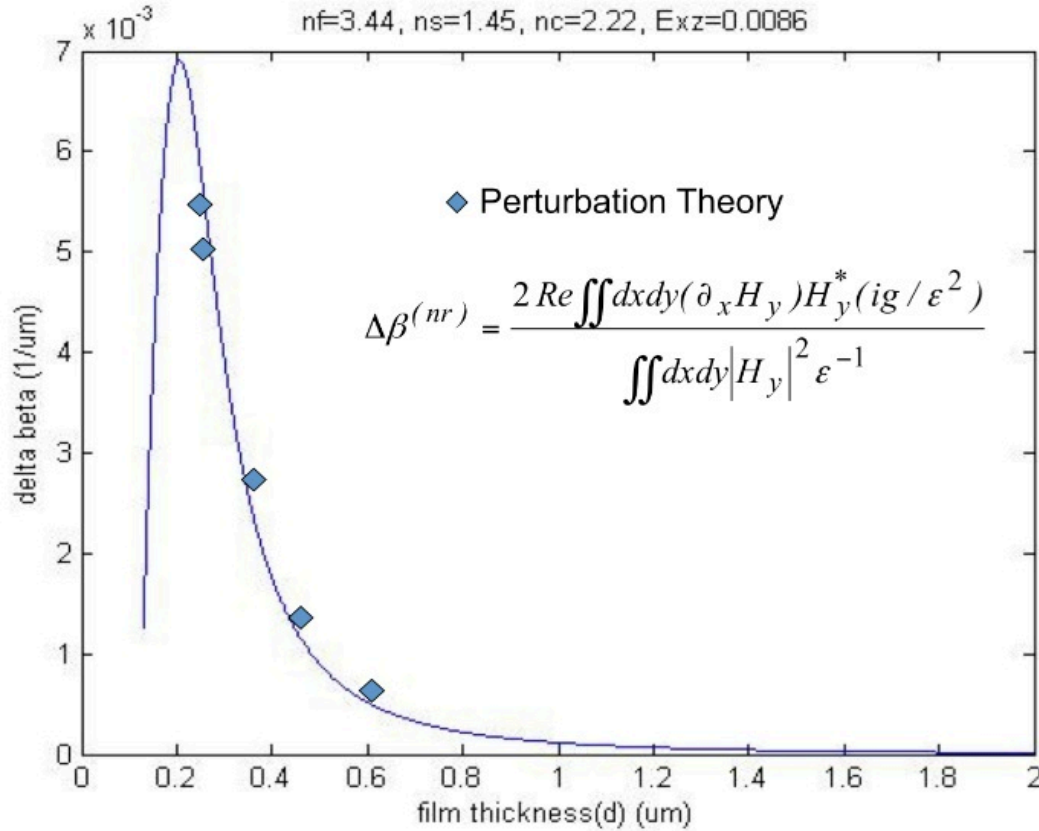


Fig. 4.10. $\Delta\beta^{nr}$ as a function of silicon layer thickness in a Ce:YIG/SOI waveguide. In the graph diamond points are for ridge-waveguides and continuous curve is for corresponding planar waveguides. Graph indicates that the finite widths of the ridges have negligible effect on $\Delta\beta^{nr}$.

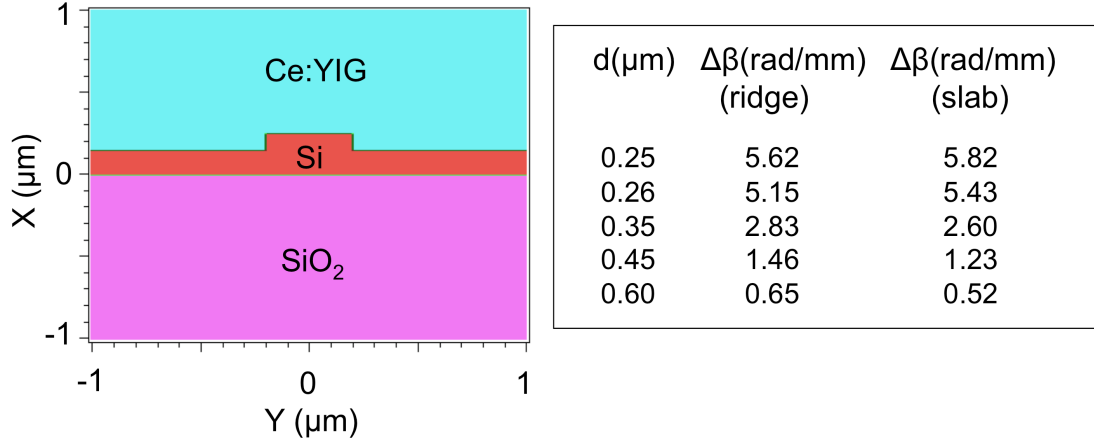


Fig. 4.11. A ridge waveguide of Ce:YIG/Si/SiO₂ (on left). $\Delta\beta^{nr}$ for slab and ridge structures are tabulated on right.

(II) TM mode propagation in an asymmetric waveguide array:

Now let us look at the evanescently coupled ridge waveguide array structure of Fig. 4.12. We assume that NRPS effect in the waveguides is not the same. A gradient in the NRPS can be achieved by systematically changing the waveguide thickness in a transversely magnetized magneto-optic system [115]. The thickness dependence of the NRPS effect is shown in Fig. 4.10.

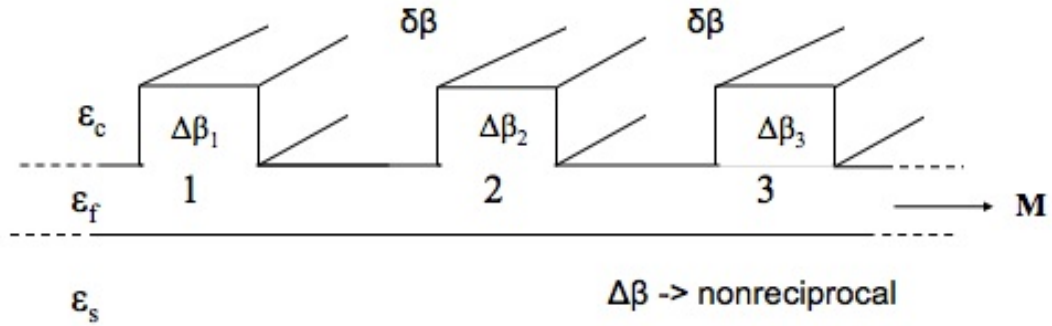


Fig. 4.12. Schematic of a ridge waveguide array highlighting the mode index ramp of $\delta\beta$ between the adjacent waveguides.

When a TM wave is launched in the array the difference in inter-modal propagation constant between forward and backward directions is given by,

$$\delta\beta_{m+1,m}^f - \delta\beta_{m+1,m}^b = \beta_{m+1}^f - \beta_m^f - (\beta_{m+1}^b - \beta_m^b) = \Delta\beta_{m+1}^{(nr)} - \Delta\beta_m^{(nr)} = \Delta(\Delta\beta^{(nr)})_{m+1,m}. \quad (4.29)$$

Where m labels the normal mode. A detailed derivation for Eq. (4.29) is given in Appendix 6. This nonzero nonreciprocal propagation constant $\Delta(\Delta\beta^{(nr)})_{m+1,m}$, plays the key role in the observation of nonreciprocal Bloch oscillations as described below.

(III) Numerical and simulation results of nonreciprocal BO effect:

Here we present a comprehensive analytical treatment of the problem and show that in the absence of gain or loss, normal modes of the waveguide array can exhibit different phase coherence lengths in opposite directions and even significantly different coherence and decoherence characteristics in the two directions. This work extends previous treatments for two coupled-NR identical-waveguides to the case of coupled-multiple-waveguide arrays with different propagation constants in individual waveguides [115]. By imposing a uniform propagation-constant step between adjacent waveguides we make contact with BO and extend previous treatments to passive NR systems and different system-mode coherence effects in opposite directions.

Consider wave propagation in uniformly chirped waveguides in the presence of an in-plane transverse magnetic field. A schematic of waveguide array is show in Fig. 4.13. Using the nearest-neighbor tight binding approximation and assuming continuous wave propagation with no absorption, coupled-mode theory yields the following equation of motion for the modal amplitude $a_n^{f,b}$ of the n^{th} waveguide [33].

$$i \frac{da_n^{f,b}}{dz} + \delta\beta^{f,b} n a_n^{f,b} + \kappa^{f,b} (a_{n-1}^{f,b} + a_{n+1}^{f,b}) = 0. \quad (4.30)$$

Here f and b denote the forward and backward directions. Note that in Eq. (4.30) the wavenumber ($\beta = (2\pi/\lambda) \cdot n_{\text{eff}}$) of the $n=0$ waveguide has been separated out [33]. λ is the wavelength in vacuum, n_{eff} is the waveguide-mode index, $\delta\beta^{f,b}$ is the difference in waveguide-mode wavenumber between adjacent waveguides, and $\kappa^{f,b}$ are the inter-waveguide coupling constants in the forward and backward directions. The simultaneous

constancy of parameters $\delta\beta^{f,b}$, hence the possibility of BO in opposite directions, is investigated below.

In a normal mode formulation the light coupled into the central waveguide of the array at the input facet can be described as a linear combination of normal modes, the m^{th} mode propagation constant given by $\beta_0 + m\delta\beta$. Here β_0 is the propagation constant of the zeroth normal mode. Refocusing (periodic Bloch oscillations) occurs when the normal modes recover an integer multiple of their initial phases. The Bloch period of oscillation (L_B) depends on the propagation constant difference $\delta\beta = (2\pi/\lambda)\Delta n$ and the optical wavelength λ through the relation $L_B = 2\pi/\delta\beta = \lambda/\Delta n$ for a modal refractive index difference Δn . A lateral spread of about $\pm 4k/\delta\beta$ waveguides from the center is predicted for the Bloch wave by analyzing the field dynamics and Bessel function solutions for the amplitude of the transverse wave upon excitation of a single central waveguide [33,35]. A detailed derivation for the field dynamics in the coupled array structure is given in Appendix 7.

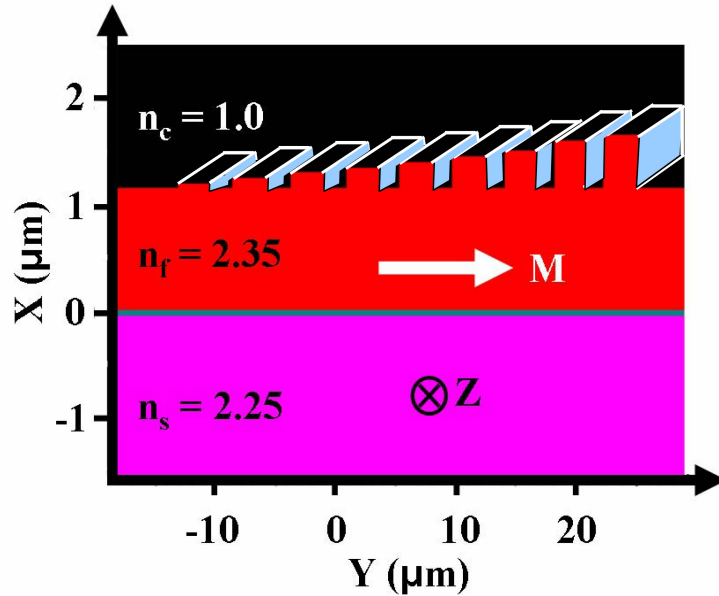


Fig. 4.13. Schematic depiction of the waveguide array highlighting the effective index progression between adjacent waveguides.

The difference in propagation constant between adjacent waveguides can be tuned by tailoring the dimensions (height or width) of the ridge. These dimensional changes result in a change in effective refractive or modal index of the waveguide mode. However, over and above these changes common to all ridge waveguides whether reciprocal or not, an additional change between adjacent waveguides can be induced by the NRPS effect, resulting in a nonreciprocal periodicity for the Bloch oscillations.

The difference between forward and backward propagation constants for adjacent waveguides is equal to the difference in nonreciprocal propagation constants between adjacent waveguides. Letting β_n^f and β_n^b be the propagation constants for forward and backward propagation for waveguide n , respectively, then

$$\begin{aligned}\delta\beta^f - \delta\beta^b &= \beta_{n+1}^f - \beta_n^f - (\beta_{n+1}^b - \beta_n^b) = (\beta_{n+1}^f - \beta_{n+1}^b) - (\beta_n^f - \beta_n^b) \\ &= \Delta\beta_{n+1}^{(nr)} - \Delta\beta_n^{(nr)} = \Delta(\Delta\beta^{(nr)})\end{aligned}\quad (4.31)$$

Here $\Delta\beta_n^{(nr)}$ stands for the nonreciprocal propagation constant difference for waveguide n . In other words, the phase matching that produces Bloch oscillatory motion in a given direction is affected by the difference in the steps in nonreciprocal propagation constant $\Delta(\Delta\beta^{(nr)})_{m+1,m}$. Assuming that Bloch oscillation conditions are satisfied in the forward direction, then using Eq. (4.31) we obtain the following expression for backward propagation:

$$i\frac{da_n^b}{dz} + (\delta\beta^f - \Delta(\Delta\beta_n^{(nr)}))na_n^b + \kappa^b(a_{n-1}^b + a_{n+1}^b) = 0. \quad (4.32)$$

Here $\delta\beta^f$ and $\Delta(\Delta\beta_n^{(nr)})$ refer to differences between adjacent waveguides in the array. For an array of coupled waveguides the propagation constant difference $\delta\beta$ between individual waveguides coincides with those for the normal modes [33].

Fig. 4.14 plots the calculated nonreciprocal propagation constant difference $\Delta\beta^{(nr)}$ for each normal mode of the system using the perturbation Eq. (4.28). Inset figure displays the power distribution for the first normal mode of the array. There is a near

linear relation between these parameters, showing that $\Delta(\Delta\beta^{(nr)})_{m+1,m}$ is approximately constant, with a deviation from linearity of less than 2%. Under these conditions backward propagation yields Bloch oscillatory motion, with Bloch period given by

$$\frac{2\pi}{\delta\beta^f - \Delta(\Delta\beta^{(nr)})}.$$

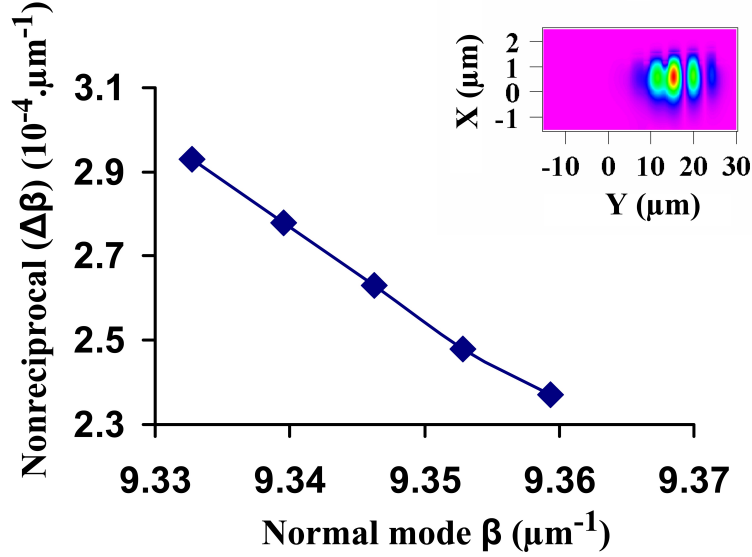


Fig. 4.14. Plot of nonreciprocal $\Delta\beta^{(nr)}$ versus normal mode β showing a nearly uniform $\Delta(\Delta\beta^{(nr)})$ between consecutive normal modes. The insets show the power distribution of the first normal mode of the array.

In designing the waveguide array we choose to vary the ridge waveguide thickness because the nonreciprocal response in transversely-magnetized systems is most sensitive to thickness changes. In Fig. 4.13 the thickness has been adjusted ($1.25 \mu\text{m}$ to $1.7 \mu\text{m}$) to yield a constant $\delta\beta^f$ of about 6650 m^{-1} between adjacent ridge waveguides. Ridge separations have also been selected to give a constant inter-waveguide coupling parameter $k \sim 3650 \text{ m}^{-1}$, with constant ridge width of $3 \mu\text{m}$. The ensuing $\delta\beta^f$ produces a spatial Bloch period of $\sim 945 \mu\text{m}$ and a lateral beam spread of less than 5 waveguides (~ 2.5 on each side) for light coupled into the center waveguide. The systematic change in ridge height introduces a nonreciprocal change in propagation

constant $\Delta(\Delta\beta^{(nr)})$ of about 14 m^{-1} between forward and backward directions between normal modes, for a typical value of $g \sim 0.004$ at $\lambda = 1.55 \text{ }\mu\text{m}$ for Bi:YIG films. Beam-propagation simulations (Fig. 4.15) show that a one- μm -wide beam launched into the center waveguide spreads out in both lateral directions but then returns to the center waveguide after a distance of about $945 \text{ }\mu\text{m}$. An excellent agreement between the calculated Bloch period ($2\pi / \delta\beta^{f,b}$) and the simulated Bloch period is obtained, with an error bar below 1%.

Upon modification of the inter-waveguide $\delta\beta$ by the nonreciprocal $\Delta(\Delta\beta^{(nr)}) \sim 14 \text{ m}^{-1}$, a change in BO period of $2 \text{ }\mu\text{m}$ is observed in the backward direction. The figure (Fig. 4.15) shows a simulated propagation with different BO period in the backward direction. We point out that the nonreciprocal effect has been artificially enlarged by a factor of 20 to make the effect visible in the scale of the figure. The simulation yields the expected Bloch oscillation in the “reverse” direction with an accuracy of about 1%. The correctness of the nonreciprocal effect discussed above was verified independently by magneto-optic full-wave finite-difference-time-domain (FDTD) method (see Appendix 8).

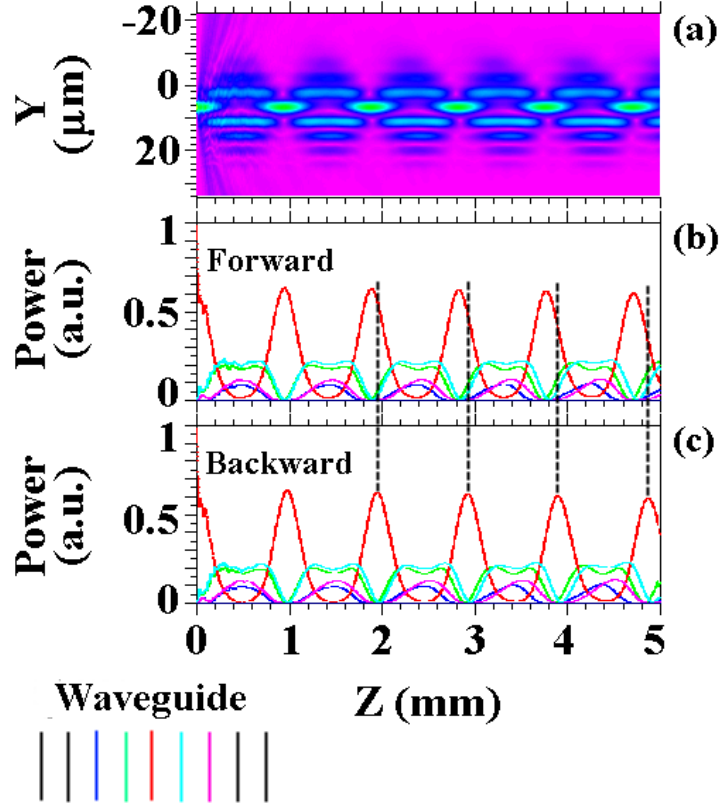


Fig. 4.15. BPM simulation results of (a) Bloch mode oscillations for the waveguide array with film index 2.35 and substrate index 2.25, showing a BO period of $\sim 945 \mu\text{m}$ for a $1 \mu\text{m}$ -wide input beam. (b) Simulated BO in FW, and (c) BW directions. The strength of $\Delta(\Delta\beta^{(nr)})$ has been artificially enhanced by a factor of twenty to highlight the difference in BO period shown with dashed lines.

However, it is also possible to violate the conditions for Bloch oscillatory motion in one direction while maintaining a uniform wavenumber step in the opposite. In the previous example the inter-modal wavenumber difference $\delta\beta^f$ is much larger than the nonreciprocal wavenumber shift $\Delta(\Delta\beta^{(nr)})$. A comparable magnitude in these two parameters is important to construct a system where the wavenumber step $\delta\beta^b$ is either cancelled out or changes value significantly across the waveguide array. It is theoretically possible to attain a unidirectional breakdown in BO if the condition $\Delta(\Delta\beta^{(nr)}) = \delta\beta^f$ is satisfied throughout the array. This possibility, which leads to the

observation of unidirectional BO in garnet/SOI hybrid material system, is discussed in detail in the next section.

Applications of the nonreciprocal BO phenomena discussed above are expected to be rather general. These could include the juncture of normal optical effects with nonreciprocity, such as magneto-optically-controlled bi-directional signal steering and switching, all-optical nonreciprocal switching, rerouting and channel reconfiguring. A related application concerns the unidirectional operation of the Bloch oscillator. Localization of the supermodes in an optical Bloch oscillator has been suggested as a means for diffraction-less beam propagation in a waveguide array [33]. Extension of the nonreciprocal BO effect to semiconductor materials is also possible. In next section we analytically show that an array can be constructed with a constant wavenumber step in one direction that simultaneously violates the conditions for standard Bloch oscillatory motion in the opposite.

4.2.3. Unidirectional BO in garnet/SOI waveguide arrays

In this section we extend the BO phenomenon to unidirectional propagation in optical media. Recently, Longhi et. al. [113] predicted unidirectional BO as a result of gain and/or loss in pseudo-Hermitian systems of complex optical lattices. Here we demonstrate theoretically that in the absence of gain or loss it is possible to attain cancellation of Bloch oscillatory motion in the optical regime unilaterally in one propagation direction while preserving this phenomenon in the opposite direction. We consider wave propagation in optical media characterized by gyrotropic dielectric permittivity tensors that although possessing imaginary off-diagonal components are strictly Hermitian in character. This study is realized for silicon platforms, in a semiconductor-dielectric hybrid material system, where we examine a nontrivial case for a waveguide array structure exhibiting unidirectional optical BO.

The array structure used in the present study consists of ridge waveguides in silicon-on-insulator (SOI) with a bonded or sputter-deposited cerium-substituted yttrium iron garnet (Ce:YIG) cover [83]. An SOI based garnet structure with a high index contrast and a large NRPS effect is best suited for the proposed unidirectional BO phenomenon.

In the following we analytically establish the unidirectional character of optical BO in the garnet/SOI material system.

We consider an asymmetric one-dimensional waveguide array as shown in Fig. 4.16. This array serves as a periodic potential system to the optical beam, while a transverse index ramp acts as a lateral driving force on the photons. The index ramp is introduced through a constant difference in mode index between adjacent waveguides, which can be tuned by tailoring the width and/or height of the ridges [24,25,33,35]. In the present analysis of unidirectional BO we utilize the basic theory developed in the previous section (4.2.2), in particular Eq. (4.28) through (4.31).

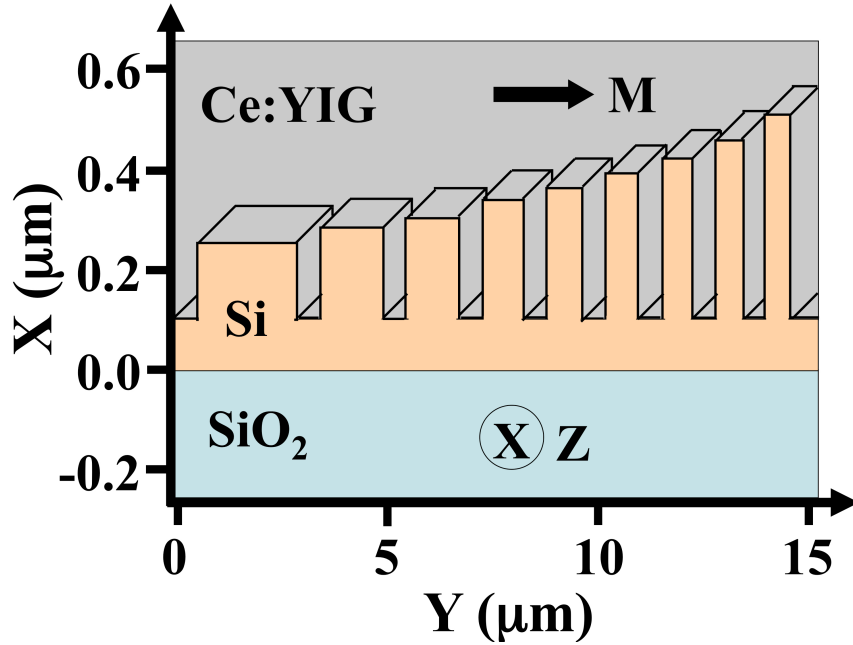


Fig. 4.16. Schematic of Ce:YIG/SOI waveguide array, note that the widths are scaled up and separations scaled down four times to fit in the sketch.

Assuming no optical absorption, we treat the array system as optically lossless. For a planar waveguide made of a SOI substrate with magnetic garnet cover layer, the TM mode dispersion relation is given by [123],

$$k_x \cdot d = \tan^{-1} \left[\frac{\epsilon_f}{k_x} \left(\frac{\gamma_{eff}}{\epsilon_{eff}} + \frac{\beta g}{\epsilon \epsilon_{eff}} \right) \right] + \tan^{-1} \left[\frac{\epsilon_f}{k_x} \left(\frac{\gamma_s}{\epsilon_s} \right) \right], \quad (4.33)$$

where $\gamma_{eff,s} = (\beta^2 - k_0^2 \epsilon_{eff,s})^{1/2}$, $k_x = (k_0^2 \epsilon_f - \beta^2)^{1/2}$, $\epsilon_{eff} = \epsilon - g^2 / \epsilon$, k_0 is the vacuum wavenumber ($2\pi / \lambda$), ϵ_s is the dielectric constant of the substrate, d is the thickness and ϵ_f is the dielectric constant of the core layer. Eq. (4.33) gives a linear dependence in β , producing different solutions for forward and backward propagating waves, with propagation constant β^f and β^b , where $\Delta\beta^{nr} = \beta^f - \beta^b$ is the NRPS per unit length. Here β^b can be calculated by reversing the sign of g through magnetization reversal. For all nine ridge waveguides in the array an initial estimate of propagation constant and film thickness was made using Eq. (4.33). We note that this equation is only strictly valid for an infinite slab waveguide with the same substrate, film and cover indices as the ridge waveguides considered here. However, finite ridge-width effects were taken into account through a perturbation theory approach using Eq. (4.28).

We use a three-dimensional semi-vectorial beam-propagation method based on a finite difference algorithm to simulate the array model [24]. Mode indices and mode field profiles are obtained using the correlation method. For each normal mode the calculated NRPS values were found to be varying approximately linearly with the propagation constants as shown in Fig. 4.17. The plot depicts nearly equally spaced β and $\Delta\beta^{nr}$ values, representing the Wannier-Stark ladder in waveguide array system [33].

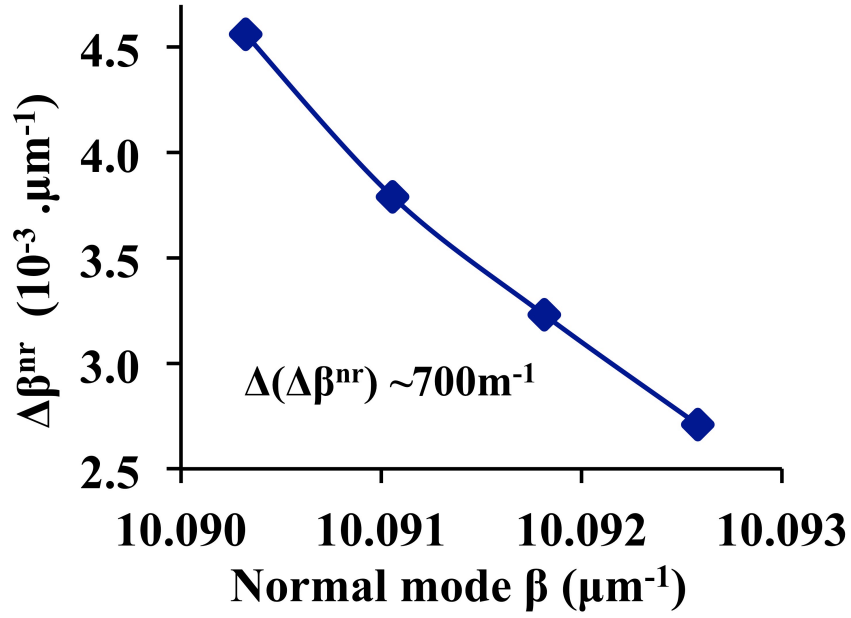


Fig. 4.17. Plot showing nearly equally spaced NRPS $\Delta\beta^{nr}$ and propagation constant β for adjacent normal modes.

From Eq. (4.31) it is clear that in adjacent waveguides the difference between the propagation constants for forward and backward propagating waves is equal to the difference in nonreciprocal propagation constants. Eq. (4.31) suggests that if one can design an array structure with inter-modal wavenumber difference $\delta\beta^f = \Delta(\Delta\beta^{nr})$, it is possible to have Bloch oscillatory motion in the forward direction with period $2\pi / \Delta(\Delta\beta^{nr})$, a characteristic feature of a discrete optical system [33]. In the BW direction the effect of $\delta\beta^b$ is completely cancelled out by nonreciprocal $\Delta(\Delta\beta^{nr})$ i.e. $\delta\beta^b = \delta\beta^f - \Delta(\Delta\beta^{nr}) = 0$, resulting in a diffractive beam spread, analogous to the behavior of a homogenous array [33]. Precise tuning of the index gradient and NRPS allows unidirectional BO. A large $\Delta(\Delta\beta^{nr})$ is critical for practical realizations.

In the FW direction each normal mode maintains a constant amplitude and width ($\sim 10 \mu\text{m}$), whereas in the BW direction it diffracts out (see Appendix 9). The supermodes themselves do not exhibit BO motion. It is their superposition that does. Our designed array consists of nine waveguides (see Fig. 4.16) made of a Si ($n_f = 3.44$) core

on a SiO_2 ($n_s = 1.45$) substrate with a Ce:YIG ($n_c = 2.22$) cover layer, wherein the thickness ($0.26 \mu\text{m}$ to $0.5 \mu\text{m}$) and the width ($0.6 \mu\text{m}$ to $0.15 \mu\text{m}$) have been adjusted to yield a constant $\delta\beta^f$ of about 700 m^{-1} in the forward direction. For a given design the wavelength tolerance is 4 nm and the tolerances in ridge height and width are 4% and 2%, respectively. The inter-waveguide separation is selected ($\sim 2 \mu\text{m}$) to produce a constant coupling parameter $k \sim 605 \text{ m}^{-1}$. The ensuing $\delta\beta^f$ produces a spatial Bloch period (L_B) of about 9 mm and a lateral beam spread of less than 7-waveguides ($\sim 11 \mu\text{m}$) for light propagating in the forward direction. Thus, an array of nine coupled waveguides is enough to demonstrate the effect. A $0.2\text{-}\mu\text{m}$ -wide beam is launched into the center waveguide and the beam is allowed to propagate through the array. As expected the beam exhibits BO motion with a period close to 9 mm and lateral spread $\sim 11 \mu\text{m}$, as shown in Fig. 4.18(a). When a $6\text{-}\mu\text{m}$ -wide beam is launched at the input facet of the array, similar BO motion ($L_B \sim 9 \text{ mm}$) is observed largely confined to the high index side with lateral spread ~ 4 -waveguides (see Fig. 4.18(c)).

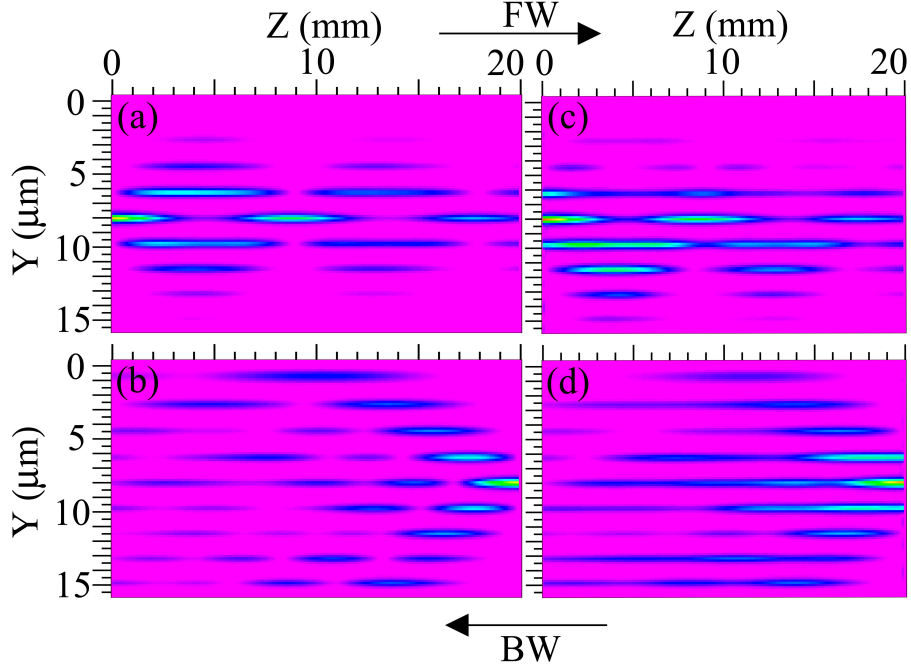


Fig. 4.18. (a) Beam evolution for single-guide excitation in the forward (FW) direction showing BO motion, (b) backward (BW) direction, showing diffractive beam spread. A 6- μm -wide beam excitation (c) in FW direction shows BO motion with the beam mostly confined to the high index side. (d) Diffractive beam spread in BW direction.

A large NRPS is introduced by adjusting the material index of each guide to create a $\Delta(\Delta\beta^{nr})$ about 700 m^{-1} . This is calculated using the perturbation method of Eq. (4.28) for a typical value of $g \sim 0.0086$ at $\lambda = 1.55 \text{ }\mu\text{m}$ for Ce:YIG. The large index contrast between Si film and Ce:YIG cover plays a critical role to realize this strong NRPS. In the backward direction, the modification of inter-waveguide $\delta\beta$ by the nonreciprocal $\Delta(\Delta\beta^{nr})$ counters $\delta\beta^f$ and induced a $\delta\beta^b \sim 0$. Therefore the index ramp vanishes and an unlimited lateral beam spread is observed in the backward direction, for both single guide excitation ($0.2\text{-}\mu\text{m}$ -wide) and broad beam ($6\text{-}\mu\text{m}$ -wide) excitation, as expected ($L_B = 2\pi / (\delta\beta^f - \Delta(\Delta\beta^{nr})) \sim \infty$) and shown in Figs. 4.18(b) and 4.18(d), respectively.

We note here that the typical value of the NRPS effect for the garnet based waveguides (e.g. Bi or rare-earth substituted YIG over $\text{Gd}_3\text{Ga}_5\text{O}_{12}$ substrate) is very small ($\sim 1.4 \text{ rad/mm}$) [115], and would require a very long array ($\sim 5 \text{ cm}$) to demonstrate the proposed unidirectional effect. However, Si based hybrid structures with magnetic

garnet cover layers can offer an NRPS effect as large as ~ 7.0 rad/mm, as demonstrated in recent work by Mizumoto and co-workers [83]. Our model system has a similar garnet/SOI composition, making possible the observation of the proposed unidirectional optical BO phenomenon within an array length of less than 1cm. Moreover, recent theoretical studies suggest NRPS values up to 100 rad/mm can be achieved by including a magneto-optical slot [121] or nano-scale air gap [122] in garnet/SOI waveguide designs. Such structures, yielding a high NRPS effect, would make a good choice for practical realization of unidirectional BO phenomenon within micron-scale array lengths.

4.2.4. On-chip optical isolation via unidirectional Bloch oscillations

Recently intense research efforts have been devoted towards the design and fabrication of fully functional integrated optical circuits [39-41]. One step that needs to be taken in scaling down optical systems to integrated circuit dimensions is the development of efficient silicon-platform-compatible on-chip optical isolators. Isolators are critical components that protect signal stability in optical circuits by blocking out back-scattered light. Thus, an on-chip isolation function would be very useful in improving optical information processing.

Research on waveguide-based isolators for integrated optical circuits bears a long history; these were already envisioned around 1972, based on a mode conversion technique [124]. Among the early published experimental works, Levy and coworkers reported an integrated isolator with sputter-deposited thin film magnets with isolation ratio 29 *dB* [80]. Over the last decade a variety of techniques have been reported, for isolation up to 30 *dB* [83-85,125]. Recently, Shoji et. al. [126], and Yu et. al. [127] have proposed schemes towards isolation ratios exceeding 30 *dB*; their fabricated isolators reaching 21 *dB* [128], and 3 *dB* [129], respectively. In the absence of a widely accepted on-chip isolation technique, the search for an optimal isolation component for photonic integrated circuits is still being actively pursued.

In the previous section, we developed the concept of unidirectional BOs in garnet/SOI waveguide array structure. Here we present a waveguide-array-based silicon-

compatible on-chip isolation technique based on unidirectional optical BOs. The isolation technique we present avoids some of the difficulties found in other schemes. It sidesteps the anti-parallel magnetic field requirement of a Mach-Zehnder interferometer design [125], and functions over a much wider band of wavelengths than is achievable with ring resonator configurations [83]. Our simulation results show that the isolation ratio between forward and backward propagating waves is as high as 36 *dB*, and it remains above 30 *dB* in a 0.7 nm wavelength range, at the telecommunication wavelength 1.55 μm .

To our knowledge, the only fabricated waveguide isolator device of comparable isolation efficiency is that produced at Bell Labs by Wolfe and coworkers based on a Faraday rotation mechanism [51]. However, a significant disadvantage of that approach is the need to zero out the geometrical birefringence in the waveguide, a tedious and costly process and the reason why researchers in optical isolator technology have moved away from Faraday rotation schemes.

The proposed isolator consists of a Bloch oscillator array and a set of identical waveguide channels that we label damping channels, placed on either sides of the array as shown in Fig. 4.19. These damping channels play a crucial role in achieving a high isolation ratio by reducing reflections of the backward propagating light from the array boundary. A taper is employed at input facet of the central waveguide to reduce insertion losses. Implementation of the array is achievable with existing tools such as electron-beam lithography, plasma etching, and focused ion beam milling (for details see section 4.3).

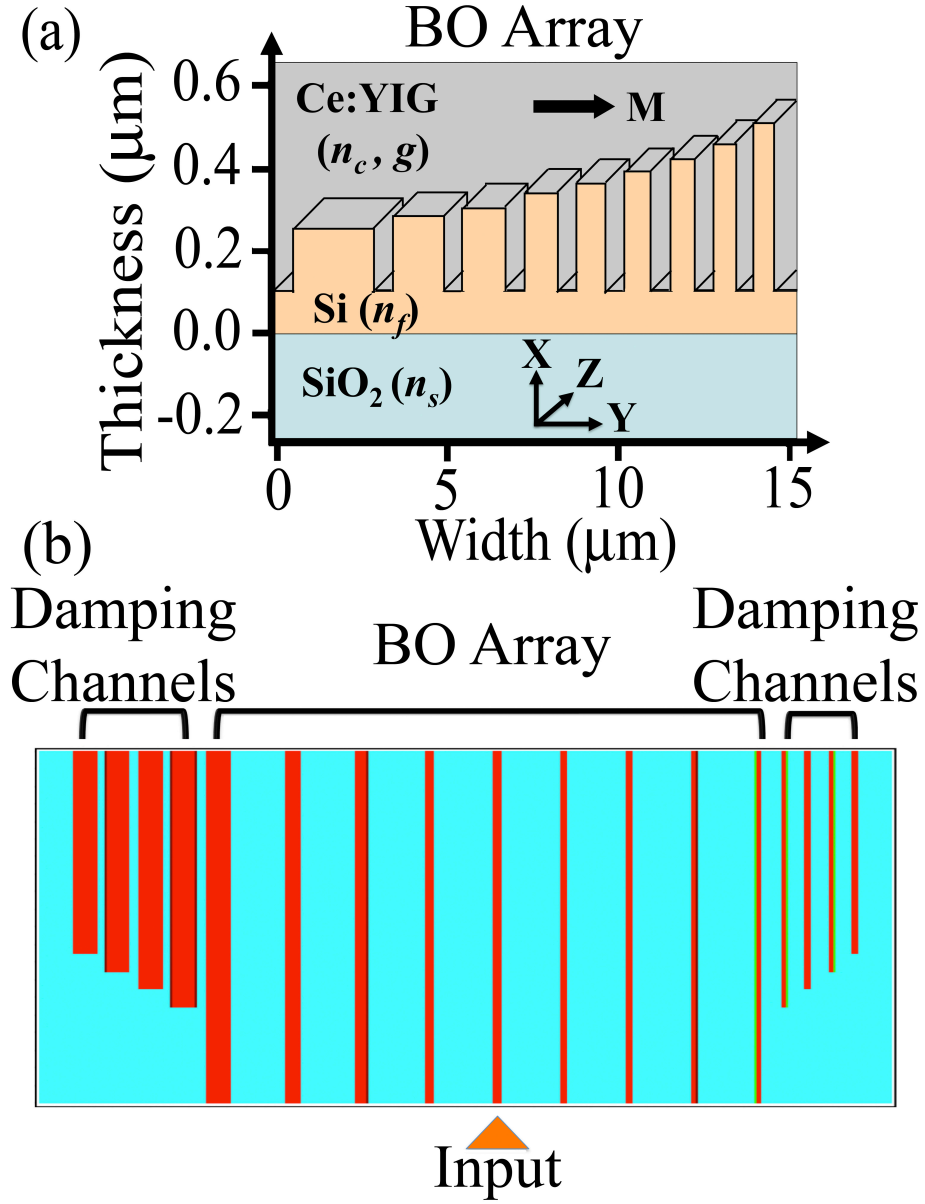


Fig. 4.19. (a) Bloch oscillator waveguide array (widths are scaled up and separations scaled down 4 times to fit in the sketch), (b) unidirectional BO based isolator design showing the BO array with damping channels on each side.

Our isolation scheme relies upon a one-way Bloch oscillatory motion of photons. In previous section we demonstrated theoretically that it is possible to attain a cancellation of Bloch oscillatory motion in the optical regime unilaterally for one propagation direction while preserving this phenomenon in the opposite direction in gyrotropic media [25]. Unidirectional BO was demonstrated for silicon platforms with magnetic garnet

cover layers. These structures have the advantage that they are compatible with existing silicon technology. Here we show how the unidirectionality of the Bloch oscillatory motion can be used for an on-chip isolator.

Eq. (4.31) indicates that the index gradient in the BW direction can be completely canceled out by designing an array structure with inter-modal wavenumber difference $\delta\beta^f = \Delta(\Delta\beta^{nr})$ i.e. $\delta\beta^b = \delta\beta^f - \Delta(\Delta\beta^{nr}) = 0$. In such structure the beam exhibits BO motion with period $2\pi / \Delta(\Delta\beta^{nr})$ in the forward direction, and a diffractive spread in the backward direction [33]. This unidirectional character of the Bloch oscillatory motion forms the working principle for our array-based on-chip isolator device.

The isolator design comprises a unidirectional Bloch oscillator and a set of damping channels in SOI substrate with Ce:YIG cover layer. The damping channels consist of tightly coupled waveguides identical to the nearest (outermost) ridge-waveguides of the Bloch oscillator array, forming a strong coupling region, as shown in Fig. 4.20. This design controls the light reaching the outmost waveguides in order to carry away unwanted light in a double return-channel circulator action, thus helping to improve the isolation ratio in the central waveguide. An inverted taper is employed at the input facet of the central waveguide to reduce coupling losses. The length of the array is one Bloch period in the forward direction. Forward-propagating light is thus refocused into the central input channel. A three-dimensional semi-vectorial beam-propagation method was used to simulate the isolator performance of our design. Field profiles of the normal modes of the array were calculated using the correlation method, and NRPS per unit length were calculated by a perturbation method technique.

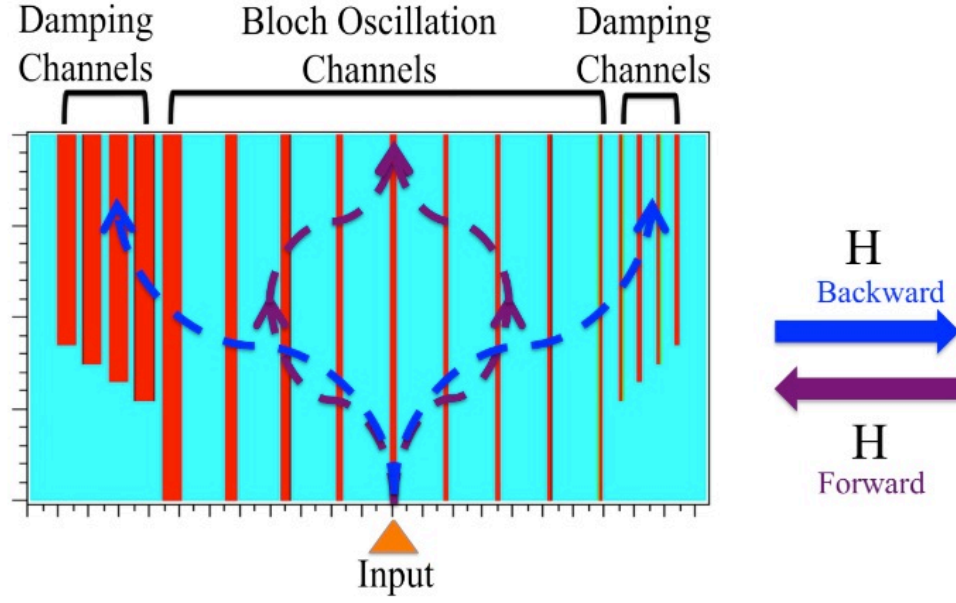


Fig. 4.20. Schematic showing working principle of the unidirectional BO based optical isolator.

Here all the waveguide array parameters are same as used for unidirectional BO study in section (4.2.3). A fiber mode is launched into a 60 nm-wide taper perfectly matched to the dimensions of the central guide of the array. Simulation results are shown in Fig. 4.20. In the forward direction, the beam exhibits BO propagation with period $(2\pi / \delta\beta) \sim 9 \text{ mm}$ and lateral spread about $11 \text{ } \mu\text{m}$, as shown in Fig. 4.21(c). Four strongly coupled channels, with coupling constant $k \sim 10^5 \text{ m}^{-1}$, are employed on each side of the nine-waveguide BO array to capture the divergent light in the backward direction, that would otherwise degrade the isolator performance to 11 dB due to reflections from the finite-width array.

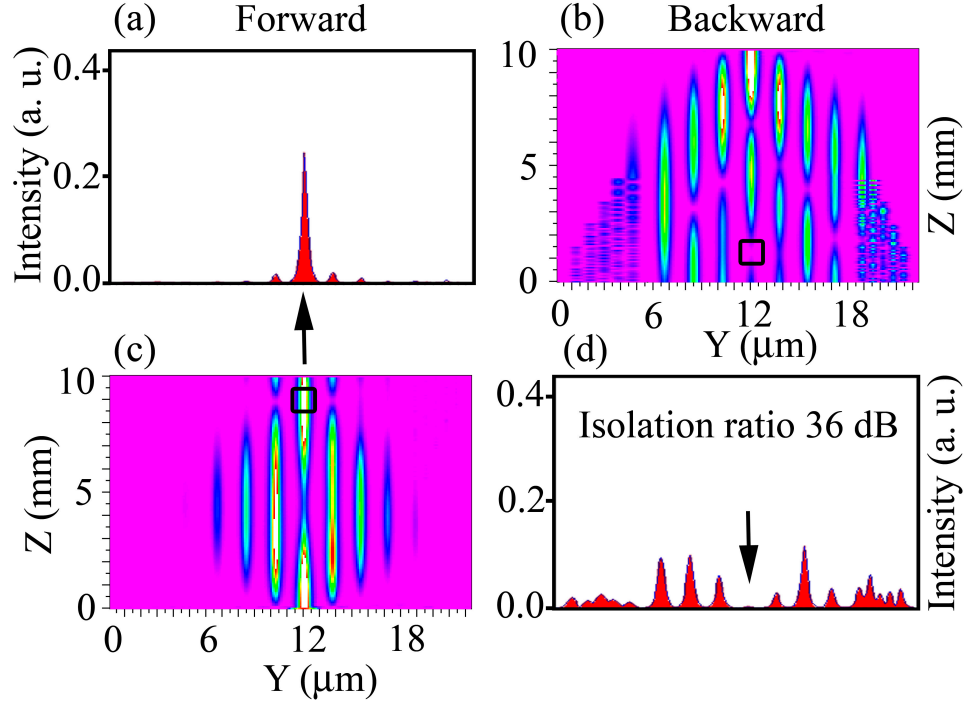


Fig. 4.21. In the FW direction the beam returns to the central channel after travelling one Bloch period as shown by the intensity plot in (a), and the simulation plot in (c); in the BW direction a diffractive beam spread occurs with the beam reaching the damping channels as depicted by simulation plot in (b), and the corresponding intensity plot in (d). The intensity plots (a) and (d) show the slice output at the Bloch period (highlighted with square boxes in (c) and (b)) in FW and BW direction, respectively.

A large NRPS ($\Delta(\Delta\beta^{nr}) \sim 700 \text{ m}^{-1}$) is introduced by adjusting the mode indices of the guides; as a result the index ramp vanishes ($\delta\beta^b \sim 0$) and an unlimited lateral beam spread is observed in the BW direction $L_B = 2\pi / (\delta\beta^f - \Delta(\Delta\beta^{nr})) \sim \infty$, as shown in Fig. 4.21(b). An isolation ratio, defined as the intensity ratio exiting the central channel in the forward and backward directions, of 36 dB was observed for 1.55 μm wavelength (Fig. 4.21(a), (d)). The isolation ratio stays higher than 30 dB in a 0.7 nm wavelength range around 1.55 μm . The footprint of the proposed device is 9 mm in length and 21 μm in width. The device supports a 400 μm length tolerance for 30 dB and higher isolation performance. For a given design, the tolerances in ridge height and width are 10 nm and 3 nm, respectively. Insertion losses, including $\sim 3 \text{ dB}$ fiber mode to input coupling, are estimated at $\sim 6 \text{ dB}$.

The isolation is observed for the central guide of the Bloch oscillator array only; the other waveguides in the array are required to activate the BO effect. At the same time, the same isolator device can perform as a fast optical switch via magnetization reversal, turning off the forward beam. Modifications in the damping channel design allow achieving isolation as high as 55 dB; schematic of the modified design is shown in Fig. 4.22.

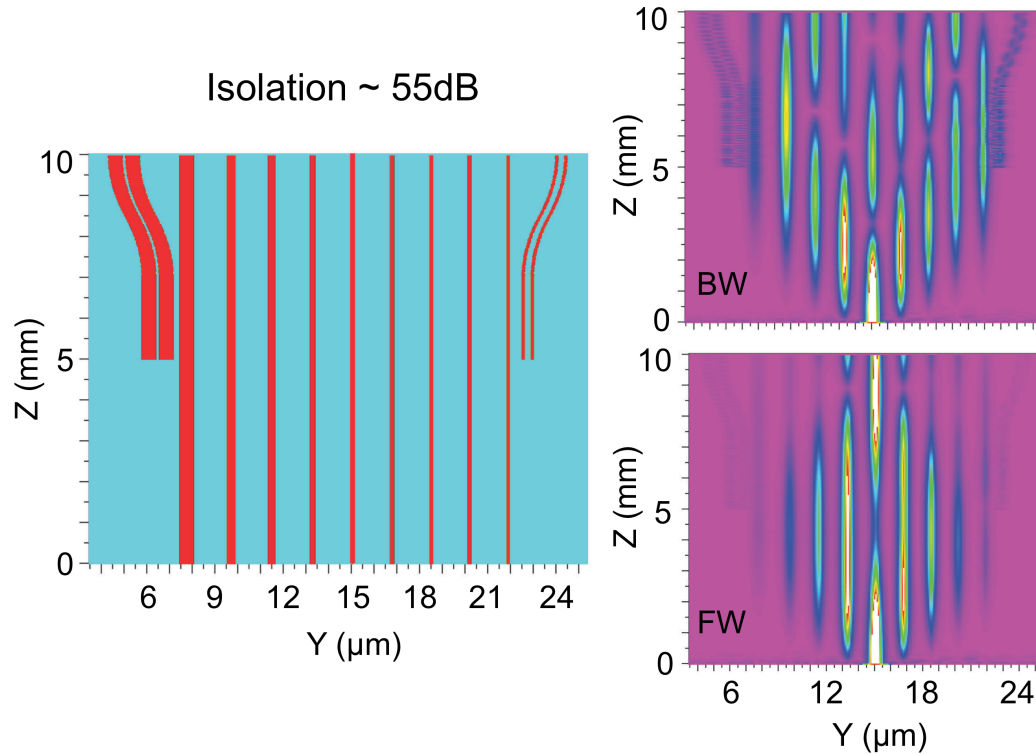


Fig. 4.22. Isolator schematic with modified damping channel design. This design gives isolation of ~ 55 dB.

The presented unidirectional BO based technique offers high isolation ratio and large bandwidth with the prospect of enhancing these features further by incorporating judicious modifications in the structure design and material system. Recent analytical studies have predicted NRPS values up to 100 rad/mm for garnet/SOI waveguides using a magneto-optical slot [121] or nano-scale air gap [122]. Such structures would allow reduced-footprint on-chip isolators in the hundreds of microns-scale based on the proposed unidirectional BO scheme. Furthermore, the fabrication complexity due to

ridge height variation could be alleviated through array-designs relying on the width-dependence of the NRPS effect.

In summary, we analytically demonstrated an on-chip isolation technique based on the unidirectional optical BO effect. We predict an optical isolation of 36 *dB* in a model design consisting of ridge waveguides in a garnet/SOI material system. Moreover, the proposed waveguide-array-based device offers multi-functional applications, such as optical switching with embedded isolation function, well suited for photonic integrated circuits.

4.3. Array designs, performance and fabrication

Figure 4.23 shows a SEM micrograph of a test structure fabricated to the specifications of the proposed on SOI device via electron-beam (e-beam) lithography in collaboration with Professor T. Mizumoto of the Tokyo Institute of Technology. Test samples for this work were patterned by e-beam lithography and plasma etching techniques for the purpose of analyzing fabrication tolerances.

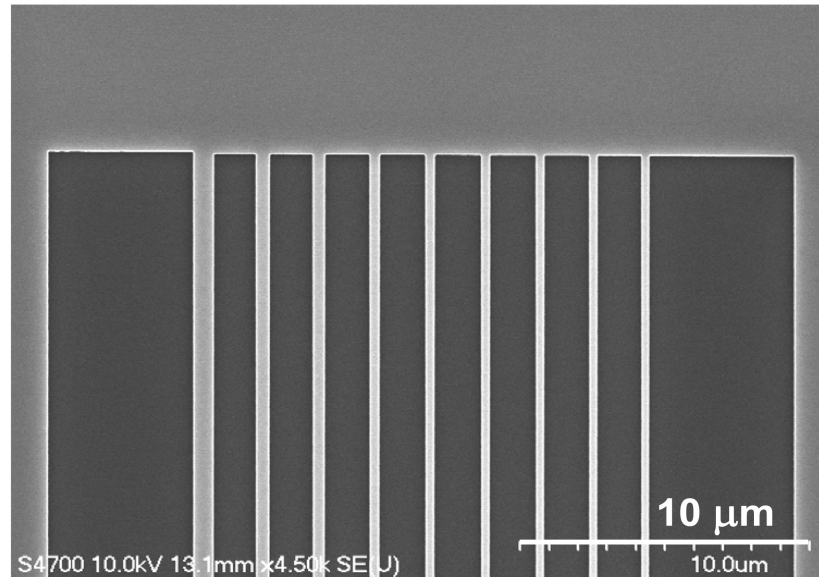


Fig. 4.23. SEM image of a test structure fabricated in SOI via e-beam lithography for the design parameters simulated in Fig. 4.19(a).

Focused-ion-beam milling equipped with a Nanopattern Generation System (NPGS) [Nabity] is used to introduce the required thickness gradient (steps) in the array. FIB is a mask-less, high-precision nano fabrication technique that has been widely used to produce nanoscale devices. It has a similar operation principal to a SEM. However, the FIB system consists of an ion beam for writing patterns instead of an electron beam. Gallium is the most-commonly used ion-species the FIB system. A schematic of the FIB is given in Fig. 4.24.

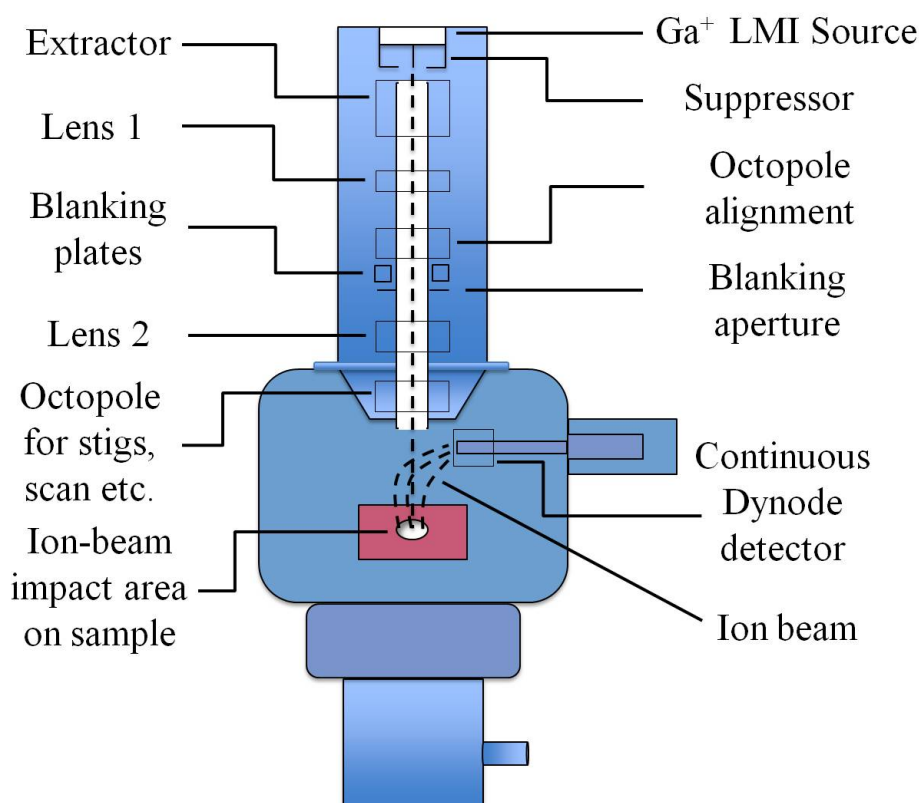


Fig. 4.24. Schematic of a typical focused-ion-beam (FIB) column.

Our strategy is to start with a slab thickness comparable to that of the thickest ridge, pattern the array by e-beam lithography and plasma etching, and then form ridge-height steps by thinning down the ridges. Tests have already been performed by our research group here at Michigan Tech to accurately mill down thicknesses by 15 nm to $\sim 100\text{ nm}$, as shown in Fig. 4.25, with $\pm 5\text{ nm}$ thickness tuning control. In addition, the surface-quality of the ridge tops is sufficiently smooth for our optical studies since the FIB can produce surfaces with a roughness of less than 5 nm (see Fig. 4.26).

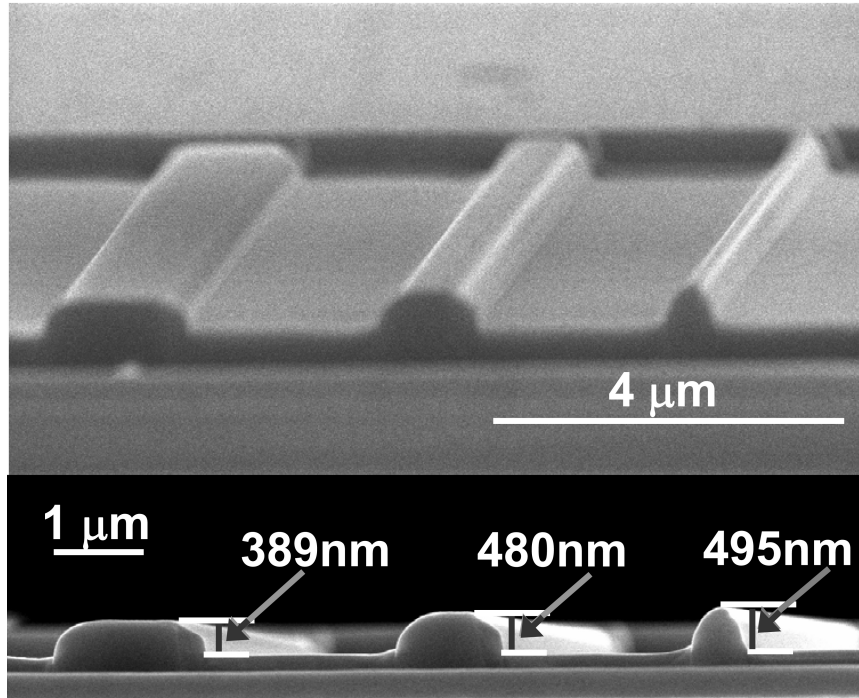


Fig. 4.25. Scanning-electron-micrographs of FIB-fabricated ridges of different heights in SOI.

There are other advantages to FIB milling as it allows producing a nonlinear gradient in thickness giving us more flexibility in the array design. Our FIB system allows us to mill down a 9-mm long array in less than 10 hours. Our plan is to commercially acquire or fabricate SOI slab waveguides of thickness equal to or slightly larger than the thickest ridges in the array and to mill down the other ridges according to the corresponding design thicknesses.

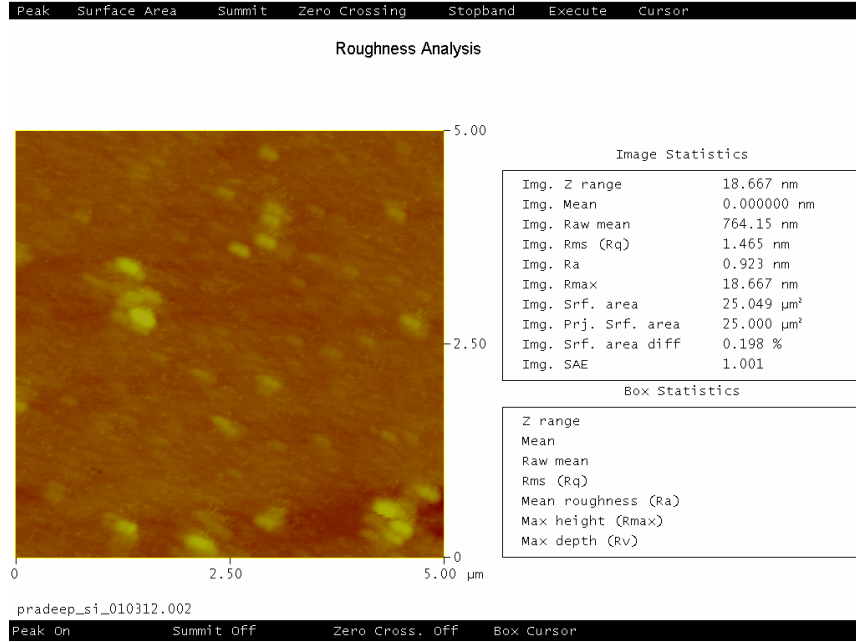


Fig. 4.26. Atomic force microscope (AFM) image of the milled surface on Si (beam M0-50, beam current= 20 pAmp)

We have fabricated wide ridge waveguides in Si with waveguide dimensions 2-mm long and about 8 μm wide for test purposes. A standard lithography process followed by plasma etching was used to transfer ridge patterns on a commercial SOI wafer (Si/SiO₂/Si : 2 μm / 1 μm / 500 μm). Initial optical tests on wide ridge Si waveguides were successful, shown in Fig. 4.27.

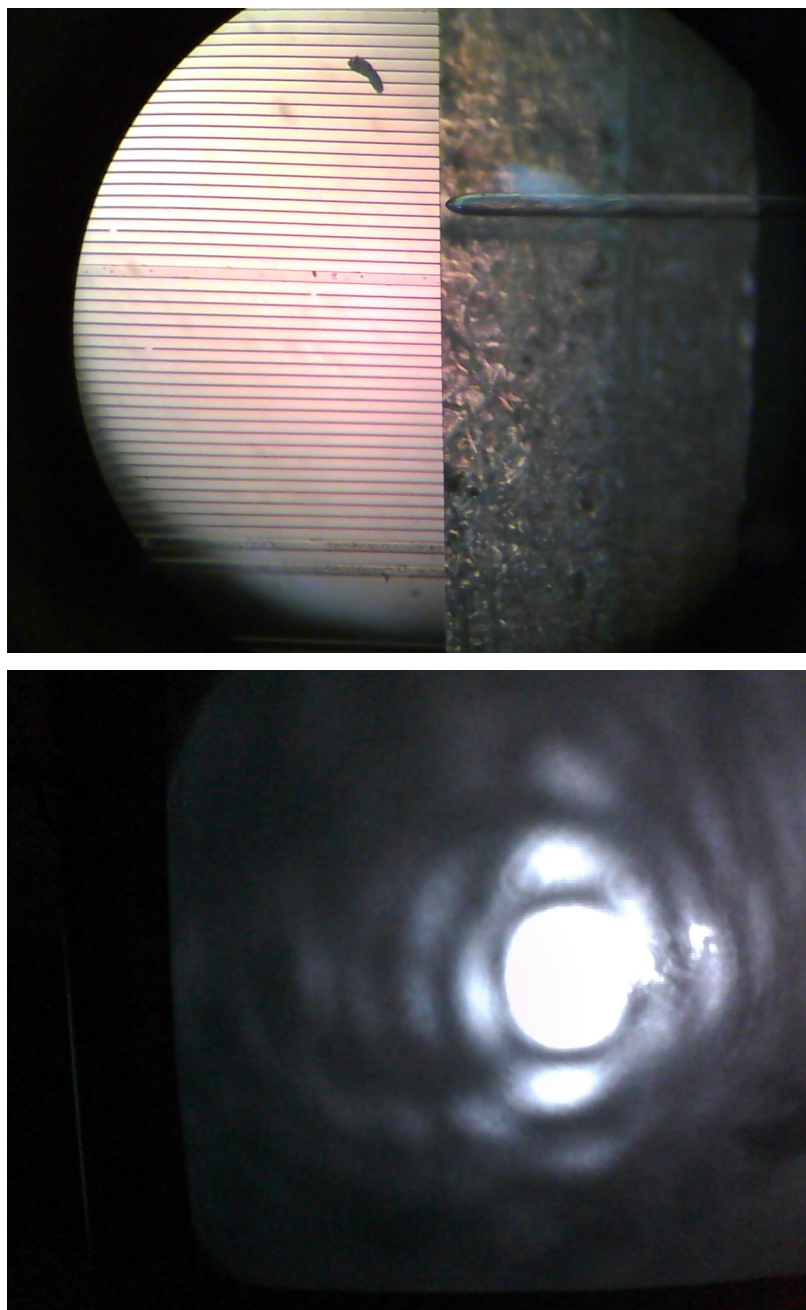


Fig. 4.27. Optical test results of a wide Si waveguide. Upper picture shows the end-fire coupling to the waveguide input. Lower picture is showing an optical mode of the waveguide.

Previous work in our group has already realized sputter-deposition of bismuth-substituted iron garnet films (Bi-YIG) of good quality on silicon substrates and has tested conformal deposition onto ridge waveguide structures.

4.4. Summary

In the present chapter, we provide an analytical proof of the existence of novel nonreciprocal BO effects in asymmetric gyrotropic waveguide arrays with transverse magnetization. A nonzero phase coherence length difference between counter-propagating normal modes of the array is obtained through numerical calculations and is demonstrated using a beam propagation method.

We extend the idea of nonreciprocal BO to silicon platforms and demonstrate the existence of unidirectional BO in garnet/SOI waveguide media. It is shown that the counter-propagating waves behave completely differently, exhibiting Bloch oscillatory motion in one direction and unlimited beam spreading in the opposite, by taking advantage of the TM mode NRPS effect.

Beyond fundamental studies, the unidirectional BO phenomenon offers potential applications in on-chip optical isolation and magneto-optically-controlled one-way beam steering in all-optical integrated photonic devices. Furthermore, this effect could be employed for nonsaturated signal amplification in discrete array structures without disturbing the stability of the light source due to back reflection. Isolation capability of the unidirectional BO based isolator device is studied in detail in garnet/SOI material system.

Initial test experiments include designing of a three-waveguide array with varying ridge height and width, using the FIB technique. Also, ridge waveguide arrays were fabricated using the e-beam and plasma etching techniques in collaboration with Prof. Mizumoto. Optics experiment results on wide silicon waveguides are encouraging and a more rigorous investigation is in progress to demonstrate the nonreciprocal and unidirectional BO effects, and to design a prototype device based on unidirectionality of the BO motion.

5. Conclusions and Future Work

5.1. Conclusions

This dissertation encompasses work done in two projects, which include a comprehensive experimental exploration of the crystallographic origin of nonlinear effects in magnetic garnet films, and an analytical investigation of novel nonreciprocal and unidirectional optical Bloch oscillatory phenomena in asymmetric waveguide arrays.

(I) The nonlinear study highlights the lattice-imperfection and compositional origins of the second harmonic response in bismuth-substituted iron garnet (Bi:YIG) films. In particular the roles of lattice mismatch strain and micro-strain on SHG in $(\text{Bi,Y})_3(\text{Fe,Ga})_5\text{O}_{12}$ films are elucidated based on experimental findings. An exhaustive study of the second harmonic response as a function of strain in Bi:YIG films shows a strong dependence on lattice mismatch strain. It is found that SHG signal strength increases with strain in Bi:YIG films. Broken spatial inversion symmetry near film-substrate interfaces plays a crucial role in the observation of SHG in these films. Bismuth and yttrium concentrations correlate with strain in the material, thus affecting the SHG response. An in-depth analysis of the film's stoichiometrical composition shows that an increase in yttrium atomic concentration in the dodecahedral sublattice of the $(\text{Bi,Y})_3(\text{Fe,Ga})_5\text{O}_{12}$ garnet film leads to an enhancement in SHG, while an increase in bismuth concentration engenders an adverse effect. Inversion centers in the structure of Bi:YIG film grown over GGG substrate are prevented by the combined effects of lattice-mismatch strain and compositional gradients. Films' growth parameters were explored. In our study we found that lattice mismatch strain shows an inverse relation to the films' deposition rate, thus providing a means for strain control during the deposition process.

(II) This dissertation also addresses novel nonreciprocal and unidirectional Bloch oscillatory phenomena. We analytically show the existence of nonreciprocal BO in passive magneto-optic waveguide arrays with linearly growing effective index, in the absence of optical gain or loss mechanisms. A key role is played by the TM mode nonreciprocal phase shift effect. This effect can be tuned by adjusting the gyrotropy

parameter, as well as the index contrast between film, substrate and cover. A nonzero phase difference between counter-propagating waves is obtained. It is shown that an array can be constructed with a constant waveguide mode-index ramp in one propagation direction that simultaneously violates the conditions for standard Bloch oscillatory motion in the opposite.

We extend the idea of nonreciprocal BO further and demonstrate the existence of unidirectional BO in technologically important silicon platforms. It is shown that the counter-propagating waves behave completely differently, showing Bloch oscillatory motion in one direction and unlimited beam spreading in the opposite. Beyond fundamental studies, the unidirectional BO phenomenon offers potential applications in magneto-optically-controlled one-way beam steering in integrated photonic circuits. Furthermore, this effect could be employed for nonsaturated signal amplification in discrete array structures without disturbing the stability of the light source due to back reflection.

An on-chip optical isolator was designed based on the unidirectionality of the magneto-optic Bloch oscillatory motion. The proposed device delivers an isolation ratio as high as 36 dB that remains above 30 dB in a 0.7 nm wavelength bandwidth, at the telecommunication wavelength 1.55 μm . Slight modifications in isolator design allow one to achieve an even more impressive isolation ratio ~ 55 dB, but at the expense of smaller bandwidth.

5.2. Future work

This dissertation addresses an important technological need, namely the development of integrated multifunctional devices for optical communications and data processing. The beauty of unidirectional optical Bloch oscillations is that it allows the implementation of several important functionalities in a single integrated optical device, thus boosting compactness and minimizing insertion losses in highly integrated optical systems. Optical isolation, fast switching, routing and amplification may be combined in multifunctional on-chip devices.

The present dissertation work has successfully developed the working principle for on-chip isolator devices. However, further research efforts are required to demonstrate experimentally the optical isolation and multifunctional capability of unidirectional Bloch oscillatory motion. The objective of the future activity can be to develop compact multifunctional photonic crystal devices on chip merging together several functionalities into a single device in order to circumvent serial integration. Boosting device compactness and minimizing insertion losses in a loss intolerant environment can be the key steps in the future work plan. Array configurations that optimize optical isolation by minimizing backscattered power and stray light into the input channel can also be the part of further study.

Development of these multifunctional on-chip devices poses special challenges, such as requirement of a material system offering high NRPS effect. A number of innovations have been proposed in the literature to enhance the nonreciprocal magneto-optic effect for transverse magnetization in optical waveguides [121,122]. The future activity needs to put effort on how to incorporate these innovations into unidirectional Bloch oscillator arrays to produce ultra-compact devices.

Reference List

1. L. B. Freund and S. Suresh, Thin Film Materials (Cambridge University Press, 2003).
2. M. Ohring, Materials Science of Thin Films (Academic Press, 2001).
3. H. S. Nalwa, Handbook of Thin Film Materials (Academic Press, 2002).
4. Image Sources:
 Silicon wafer
<http://www.zdnet.com/after-silicon-what-will-power-computing-for-the-next-10-years-and-beyond-3040153697/>
 Cell Phone
<http://www.androidauthority.com/samsung-galaxy-s3-free-canada-118727/>
 Satellite
http://www.spacetoday.org/images/Sats/MilSats/DSCS_SatInSpaceLockheedMartin.jpg
 Medical electronics
<http://www.jetmedical.com/>
 Solar panel
http://www.bizjournals.com/columbus/morning_call/2012/09/springfield-insurer-to-utilize-solar.html
5. P. A. Franken, A. E. Hill, C. W. Peters, and G. Weinreich, "Generation of Optical Harmonics". Phys. Rev. Lett. **7** (4), 118-119 (1961).
6. Y. R. Shen, "Surface nonlinear optics: A historical perspective" IEEE J. Sel. Topics Quantum Electron **6** (6), 1375-1379 (2000).
7. R. W. Boyd, Nonlinear Optics (Academic Press, 2008).
8. N. Bloembergen, Nonlinear Optics (World Scientific, 1996).
9. A. Yariv, and P. Yeh, "Optical Waves in Crystals: Propagation and Control of Laser Radiation," (Wiley-Interscience, 2002).
10. V. N. Gridnev, V. V. Pavlov, R. V. Pisarev, A. Kirilyuk and Th. Rasing, "Second harmonic generation in anisotropic magnetic films," Phys. Rev. B **63**, 184407 (2001).
11. Th. Rasing, "Nonlinear magneto-optical probing of magnetic interfaces," Appl. Phys. B: Laser Opt. **68**, 477-484 (1999).
12. O. A. Aktsipetrov, V. A. Aleshkevich, A. V. Melnikov, T. V. Misuryae, T. V. Murzina, and V. V. Randoshkin, "Magnetic field induced effects in optical

- second harmonic generation from iron-garnet Films,” *J. Magn. Magn. Mater.* **165**, 421-423 (1997).
13. T. F. Heinz, *Nonlinear Surface Electromagnetic Phenomena*, edited by H.-E. Ponath and G. I. Stegeman (North Holland, Amsterdam, 1991).
 14. P. P. Ho, and R. R. Alfano, “Optical Kerr effect in liquids”, *Phys. Rev. A* **20**, 2170-2187 (1979).
 15. G. Dixit, O. Vendrell, and R. Santra, “Imaging electronic quantum motion with light” *PNAS* **109** (29), 11636-11640 (2012).
 16. Ru-Pin Pan, H. D. Wei, and Y. R. Shen, “Optical second-harmonic generation from magnetized surfaces,” *Phys. Rev. B* **39**, 1229 (1989).
 17. W. Hubner and K. H. Bennemann, “Nonlinear magneto-optical Kerr effect on a nickel surface,” *Phys. Rev. B* **40**, 5973 (1989).
 18. V. Jahnke, J. Gudde and E. Matthias, “Growth and magnetic ordering of Ni and Co films on Rh(0 0 1) investigated with second-harmonic generation,” *J. Magn. Magn. Mater.* **232**, 27-35 (2001).
 19. F. Hansteen, O. Hunderi, T. H. Johansen, A. Kirilyuk and T. Rasing, “Selective surface/interface characterization of thin garnet films by magnetization-induced second-harmonic generation,” *Phys. Rev. B* **70**, 094408 (2004).
 20. J.-W. Jeong, S.-C. Shin, N. N. Dadoenkova, I. L. Lyubchanskii, V. K. Valev and Th. Rasing, “Direct observation of controlled strain-induced second harmonic generation in a $\text{Co}_{0.25}\text{Pd}_{0.75}$ thin film on a $\text{Pb}(\text{ZrTi})\text{O}_3$ substrate,” *Appl. Phys. Lett.* **90**, 044108 (2007).
 21. I. L. Lyubchanskii, J.-W. Jeong, S.-C. Shin, N. N. Dadoenkova, M. I. Lyubchanskii and Th. Rasing, “Influence of lattice mismatch on magnetization-induced optical second harmonic generation from a magnetic film on a nonmagnetic substrate,” *J. Appl. Phys.* **87**, 6794-6796 (2000).
 22. I. L. Lyubchanskii, N. N. Dadoenkova, and M. I. Lyubchanskii, “Second-harmonic generation from realistic film–substrate interfaces: the effects of strain,” *Appl. Phys. Lett.* **76**, 1848-1850 (2000).
 23. R. V. Pisarev, B. B. Krichevtsov, V. N. Gridnev, V. P. Klin, D. Frohlich and Ch. Pahlke-Lerch, “Optical second-harmonic generation in magnetic garnet thin films,” *J. Phys.: Condens. Matt.* **5**, 8621-8628 (1993).
 24. M. Levy and P. Kumar, “Nonreciprocal Bloch oscillations in magneto-optics waveguide arrays,” *Opt. Lett.* **35**, 3147-3149 (2010).
 25. P. Kumar and M. Levy, “Unidirectional optical Bloch oscillations in asymmetric waveguide arrays,” *Opt. Lett.* **36**, 4359-4361 (2011).
 26. F. Bloch, *Z. Phys.* **52**, 555 (1929).
 27. C. Zener, “A theory of the electrical breakdown of solid dielectrics,” *Proc. R. Soc. A* **145**, 523 (1934).

28. S. Longhi, "Quantum-optical analogies using photonic structures," *Laser & Photon. Rev.* **3**, No. 3, 243–261 (2009).
29. A. G. Chynoweth, G. H. Wannier, R. A. Logan, and D. E. Thomas, "Observation of Stark splitting of energy bands by means of tunneling transitions," *Phys. Rev. Lett.* **5**, 57-58 (1960).
30. C. Waschke, H. G. Roskos, R. Schwedler, K. Leo, H. Kurz, and K. Kohler, "Coherent submillimeter-wave emission from Bloch oscillations in a semiconductor superlattice," *Phys. Rev. Lett.* **70**, 3319-3322 (1993).
31. T. Dekorsy, P. Leisching, K. Köhler, and H. Kurz, "Electro-optic detection of Bloch oscillations," *Phys. Rev. B* **50**, 8106–8109 (1994).
32. M. Ben Dahan, E. Peik, J. Reichel, Y. Castin, and C. Salomon, "Bloch oscillations of atoms in an optical potential," *Phys. Rev. Lett.* **76**, 4508-4511 (1996).
33. U. Peschel, T. Pertsch and F. Lederer, "Optical Bloch oscillations in waveguide arrays," *Opt. Lett.* **23**, 1701-1703 (1998).
34. A. Guo, G. J. Salamo D. Duchesne, R. Morandotti, M. Volatier-Ravat, V. Aimez, G. A. Siviloglou, and D. N. Christodoulides, "Observation of PT-Symmetry Breaking in Complex Optical Potentials," *Phys. Rev. Lett.* **103**, 093902 (2009).
35. R. Morandotti, U. Peschel, J. S. Aitchison, H. S. Eisenberg and Y. Silberberg, "Experimental observation of linear and nonlinear optical Bloch oscillations," *Phys. Rev. Lett.* **83**, 4756-4759 (1999).
36. T. Pertsch, P. Dannberg, W. Elflein, A. Bräuer, and F. Lederer, "Optical Bloch Oscillations in Temperature Tuned Waveguide Arrays," *Phys. Rev. Lett.* **83**, 4752-4755 (1999).
37. G. Monsivais, M. del Castillo-Mussot, and F. Claro, "Stark-ladder resonances in the propagation of electromagnetic waves," *Phys. Rev. Lett.* **64**, 1433-1436 (1990).
38. M. de Sterke, J. Sipe, and L. Weller-Brophy, "Electromagnetic Stark ladders in waveguide geometries," *Opt. Lett.* **16**, 1141-1143 (1991).
39. Y. Vlasov, W. M. J. Green, and F. Xia, "High-throughput silicon nanophotonic wavelength-insensitive switch for on-chip optical networks," *Nature Photonics* **2**, 242 - 246 (2008).
40. L. Tsybeskov, D. J. Lockwood, and M. Ichikawa, "Silicon photonics: CMOS going optical," *Proceedings of the IEEE* **97**, no.7, 1161-1165 (2009).
41. D. Dai, J. Bauters, and J. E. Bowers, "Passive technologies for future large-scale photonic integrated circuits on silicon: polarization handling, light non-reciprocity and loss reduction," *Light: Science & Applications* **1**, 1-12 (2012).
42. P. Kumar and M. Levy, "On-chip optical isolation via unidirectional Bloch oscillations in a waveguide array," *Opt. Lett.* **37**, 3762-3764 (2012).

43. A. Paoletti, "Physics of magnetic garnets", Proceedings of the international school of physics (North-Holland, 1978).
44. T. Okuda, N. Koshizuka, H. Hayashi, H. Taniguchi, K. Satoh, and H. Yamamoto, "Synthesis of new magneto-optical material, bismuth iron garnet," IEEE Translation J. Magn. Jpn. **3**, 483-484, (1988).
45. M. Gomi, K. Satoh, and M. Abe, "New garnet films with giant Faraday rotation," Proceedings ICF-5, India, page 919 (1989).
46. A. H. Bobeck, et. al., "Uniaxial magnetic garnets for domain wall "bubble" devices," Appl. Phys. Lett. **17**, 131-134 (1970).
47. N. A. Spaldin, Magnetic Materials: Fundamentals and Device Applications (Cambridge University Press, 2003).
48. G. B. Scott, D. E. Lacklison, H. I. Ralph, and J. L. Page, "Magnetic circular dichroism and Faraday rotation spectra of $\text{Y}_3\text{Fe}_5\text{O}_{12}$," Phys. Rev. B **12**, 2562-2571 (1975).
49. Source: http://www.isowave.com/pdf/materials/Yttrium_Iron_Garnet.pdf
50. M Inoue, R Fujikawa, A Baryshev, A Khanikaev, P B Lim, H Uchida, O Aktsipetrov, A Fedyanin, T Murzina and A Granovsky, "Magnetophotonic crystals", J. Phys. D: Appl. Phys. **39**, R151–R161 (2006).
51. R. Wolfe, E. M. Gyorgy, R. A. Lieberman, V. J. Fratello, S. J. Licht, M. N. Deeter, and G. W. Day, "High frequency magnetic field sensors based on the Faraday effect in garnet thick films," Appl. Phys. Lett. **60**, 2048 (1992).
52. Reprinted with permission from [Z. Wu, Miguel Levy, V. J. Fratello and A. M. Merzlikin, "Gyrotropic Photonic Crystal Waveguide Switches," Appl. Phys. Lett. **96**, 051125 (2010)]. Copyright [2010], American Institute of Physics. For permission details see Appendix 10.
53. M. Gomi, T. Tanida and M. Abe, "RF sputtering of highly Bi-substituted garnet films on glass substrates for magneto-optic memory," J. Appl. Phys. **57** (1), 3888 (1985).
54. M. Gomi, K. Satoh and M. Abe, "Improvement in optical and magnetic properties of Bi-substituted garnet sputtered films for magneto-optical recording," J. Appl. Phys. **63** (8), 3642 (1988).
55. M. Gomi, H. Furuyama and M. Abe, "Strong magneto-optical enhancement in high Ce-substituted iron garnet films prepared by sputtering," J. Appl. Phys. **70** (11), 7065 (1991).
56. H. Yang, PhD Dissertation (2005), Material Science and Engineering, Michigan Technological University.
57. A. E. Morgan, J. Cryst. Growth **27**, 266 (1974).

58. S. Mino, M. Matsuoka, A. Take, A. Shibukawa and K. Ono, "Complete Bi-substituted iron garnet (BIG) films prepared by electron cyclotron resonance (ECR) sputtering", *Jpn. J. Appl. Phys.* **31**, (1), No. 6A, 1786 (1992).
59. T. Tepper, and C.A. Ross, "Pulsed laser deposition and refractive index measurement of fully substituted bismuth iron garnet films," *J. Cryst. Growth* **255**, 324-331 (2003).
60. M.-Y. Chern , F.-Y. Lo , Da-Ren Liu , K. YANG and J.-S. Liaw, "Red Shift of Faraday Rotation in Thin Films of Completely Bismuth-Substituted Iron Garnet $\text{Bi}_3\text{Fe}_5\text{O}_{12}$," *Jpn. J. Appl. Phys.* **38**, (1), 6687-6689 (1999).
61. B. Vertruyen, R. Cloots, J. S. Abell, T. J. Jackson, R. C. da Silva, E. Popova, and N. Keller, "Curie temperature, exchange integrals, and magneto-optical properties in off-stoichiometric bismuth iron garnet epitaxial films," *Phys. Rev. B* **78**, 094429 (2008).
62. M. Inoue and T. Fujii, "A theoretical analysis of magneto-optical Faraday effect of YIG films with random multilayer structures," *J. Appl. Phys.* **81**(8) (1997).
63. S. Wittekoek, T. J. A. Popma, J. M. Robertson and P. F. Bongers, "Magneto-optic spectra and the dielectric tensor elements of bismuth-substituted iron garnets at photon energies between 2.2-5.2eV," *Phys. Rev. B*, **12**, (7), 2777 (1975).
64. W. Zhao, "Magneto-optic properties and sensing performance of garnet YbBi:YIG ," *Sensors and Actuators A* **89**, 250-254 (2001).
65. V. J. Fratello, I. Mnushkina, S. J. Licht and R. R. Abbott, "Growth and Characterization of Magneto-optic Garnet Films with Planar Uniaxial Anisotropy," *Mater. Res. Soc. Symp. Proc.* Vol. 834 (2005).
66. C. Leycuras, H. Le Gall, J. M. Desvignes, M. Guillot, and A. Marchand, "Magnetic and magneto-optical properties of a cerium YIG single crystal," *IEEE Trans. Magn.*, **MAG-21**, 1960 (1985).
67. T. Shintaku, T. Uno and M. Kobayashi, "Magneto-optic channel waveguides in Ce-substituted yttrium iron garnet," *J. Appl. Phys.* **74** (8), 4877 (1993).
68. H. Dotsch, N. Bahlmann, O. Zhuromskyy, M. Hammer, L. Wilkens, R. Gerhardt, P. Hertel, and A. F. Popkov, "Applications of magneto-optical waveguides in integrated optics: review," *J. Opt. Soc. Am. B* **22**, 240-253 (2005).
69. R. Wolfe, R. A. Lieberman, V. J. Fratello, R. E. Scotti, and N. Kopylov, "Etch-tuned ridged waveguide magneto-optic isolator," *Appl. Phys. Lett.* **56**, 426 (1990).
70. H. Kidoh, A. Morimoto and T. Shimizu, "Synthesis of ferromagnetic Bi-substituted yttrium iron garnet films by laser ablation," *Appl. Phys. Lett.* **59** (2), 237 (1991).

71. S. A. Campbell, *The Science and Engineering of Microelectronic Fabrication* (Oxford University Press, 2001).
72. Source: http://www.jawoollam.com/vase_home.html
73. Reprinted with permission from [N. Dissanayake, M. Levy, A. Chakravarty, P. A. Heiden, N. Chen, and V.J. Fratello, "Magneto-photonic crystal optical sensors with sensitive covers," *Appl. Phys. Lett.* **99**, 091112 (2011)]. Copyright [2011], American Institute of Physics. For permission details see Appendix 10.
74. N. Sugimoto, H. Terui, A. Tate, Y. Katoh, Y. Yamada, A. Sugita, A. Shibukawa and Y. Inoue, "A hybrid integrated waveguide isolator on a silica-based planar lightwave circuit", *J. Lightwave Technol.*, **14**, (11), 2537 (1996).
75. M. Inoue, K. Arai, T. Fujii, M. Abe, "One dimensional magnetophotonic crystals," *J. Appl. Phys.*, **85** (8), 5768 (1999).
76. R. W. Hansen, L. E. Helseth, A. Solovyev, E. Il'Yashenko and T. H. Johansen, "Growth and characterization of (100) garnets for imaging," *J. Magn. and Magn. Mat.* **272**, 2247-2249 (2004).
77. R. M. Grechishkin, M. Yu. Goosev, E. Il'Yashenko, and N. S. Neustroev, "High-resolution sensitive magneto-optic ferrite-garnet films with planar anisotropy," *J. Magn. Magn. Mat.* **157**, 305 (1996).
78. H. Ferrari, V. Bekeris, and T. H. Johansen, "Direct observation of magnetic patterns in audio tapes," *Physica B* **354**, (2004).
79. I. Nistor, PhD Dissertation (2006), University of Maryland, College Park.
80. M. Levy, R. M. Osgood, Jr., H. Hegde, F. J. Cadieu, R. Wolfe, and V. J. Fratello, *IEEE Phot. Technol. Lett.* **8**, 903-905 (1996).
81. <http://www.ioffe.ru/SVA/NSM/Semicond/GaAs/basic.html>
82. H. Yokoi, "Calculation of nonreciprocal phase shift in magneto-optic waveguides with Ce:YIG layer," *Optical Materials* **31**, 189-192 (2008).
83. M. -C. Tien, T. Mizumoto, P. Pintus, H. Kromer and J. E. Bowers, "Silicon ring isolators with bonded nonreciprocal magneto-optic garnets," *Opt. Express* **19**, 11740-11745 (2011).
84. L. Bi, J. Hu, P. Jiang, D. H. Kim, G. F. Dionne, L. C. Kimerling, and C. A. Ross, "On chip optical isolation in monolithically integrated nonreciprocal optical resonators," *Nat. Photon.* **5**, 758-762 (2011).
85. T. Mizumoto, Y. Shoji, and R. Takei, "Direct wafer bonding and its application to waveguide optical isolators," *Materials* **5**, 985-1004 (2012).
86. M. Fiebig, D. Fröhlich, K. Kohn, St. Leute, Th. Lottermoser, V. V. Pavlov and R. V. Pisarev, "Determination of the magnetic symmetry of hexagonal manganites by second harmonic generation," *Phys. Rev. Lett.* **24**, 5620-5623, (2000).

87. M. Fiebig, D. Fröhlich, and Th. Lottermoser, "Spin-angle topography of hexagonal manganites by magnetic second-harmonic generation," *Appl. Phys. Lett.* **77**, 4401-4403, (2000).
88. O. A. Aktsipetrov, A. A. Fedyanin, A. V. Melnikov, E. D. Mishina, and T. V. Murzina, "Second harmonic generation as a nondestructive readout of optical (photo(electro)chromic and magnetic) memories," *Jpn. J. Appl. Phys.* **37**, 122-127 (1998).
89. F. Hansteen, Ola Hunderi, T. H. Johansen, A. Kirilyuk and Theo Rasing, "Selective surface/interface characterization of thin garnet films by magnetization-induced second-harmonic generation" *Phys. Rev. B* **70**, 094408 (2004).
90. Jae-Woo Jeong, Sung-Chul Shin, N. N. Dadoenkova, I. L. Lyubchanskii, V. K. Valev and Th. Rasing, "Direct observation of controlled strain-induced second harmonic generation in a $\text{Co}_{0.25}\text{Pd}_{0.75}$ thin film on a $\text{Pb}(\text{ZrTi})\text{O}_3$ substrate", *Appl. Phys. Lett.* **90**, 044108 (2007).
91. HANDBOOK OF OPTICS, Editor in Chief: M. Bass (McGraw-Hills, 1995).
92. Nonlinear Optics, Lecture notes by Prof. W. UBACHS, LASER CENTRE VRIJE UNIVERSITEIT AMSTERDAM DEPARTMENT OF PHYSICS AND ASTRONOMY: <http://www.nat.vu.nl/~wimu/NLO-2001.pdf>
93. <http://oer.physics.manchester.ac.uk/AQM2/Notes/Notes-3.2.html>
94. O.A. Aktsipetrov, Tatyana V. Murzina, Evgeniya M. Kim, Ruslan V. Kapra, and Andrey A. Fedyanin, "Magnetization-induced second- and third-harmonic generation in magnetic thin films and nanoparticles," *J. Opt. Soc. Am. B* **22**, 138-147 (2005).
95. Jae-Woo Jeong, Sung-Chul Shin, I. L. Lyubchanskii and V. N. Varyukhin, "Strain-induced three-photon effects," *Phys. Rev. B.* **62**, 13455-13463 (2000).
96. Y.R. Shen, "Surface second harmonic generation," *Ann. Rev. Mater. Sci.* **16**, 69-86 (1986).
97. H. W. K. Tom, T. F. Heinz, and R. Shen, "Second-harmonic reflection from silicon surfaces and its relation to structural symmetry," *Phys. Rev. Lett.* **51**, 1983-1986 (1983).
98. M. Fiebig, Th. Lottermoser, V. V. Pavlov, and R. V. Pisarev, "Magnetic second harmonic generation in centrosymmetric CoO , NiO , and KNiF_3 ," *J. Appl. Phys.* **93**, 6900-6902 (2003).
99. J. Reif, J. C. Zink, C. M. Schneider, and J. Kirschner, "Effects of surface magnetism on optical second harmonic generation," *Phys. Rev. Lett.* **67**, 2878-2881, (1991).

100. O. A. Aktsipetrov, O. V. Braginskii, and D. A. Esikov, "Nonlinear optics of girotropic media: second harmonic generation in rare-earth iron garnets," *Sov. J. Quantum Electron.* **20**, 259-263, (1990).
101. Rutherford Backscattering Spectroscopy measurements were performed by EVANS Analytical Group.
102. <http://www.metricon.com/basic.html>
103. H. Nishihara, M. Haruna, T. Suhara, *Optical Integrated Circuits* (McGraw-Hill, New York, 1987).
104. A. Furuya, C. Baubet, H. Yoshikawa, T. Tanabe, S. Hirono and M. Yamamoto, "Controlling garnet film composition by magnetic-field-controlled radio frequency magnetron sputtering," *J. Appl. Phys.* **87** (8), 6776 (2000).
105. P. Kumar, A. I. Maydykovskiy, M. Levy, N. V. Dubrovina, O. A. Aktsipetrov, "Second harmonic generation study of internally-generated strain in bismuth-substituted iron garnet films," *Opt. Exp.* **18** (2), 1076-1084 (2010).
106. A.V. Melnikov, A.A. Nikulin and O.A. Aktsipetrov, "Hyper-Rayleigh scattering by inhomogeneous thin films of $\text{Pb}_x(\text{Zr}_{0.53}\text{Ti}_{0.47})\text{O}_3$: Disorder effects," *Phys. Rev. B* **67**, 134104 (2003).
107. T. Pertsch, P. Dannberg, W. Elflein, A. BrÅNauer, and F. Lederer, *Phys. Rev. Lett.* **83**, 4752 (1999).
108. D. N. Christodoulides, F. Lederer, and Y. Silberberg, *Nature* **424**, 817 (2003).
109. B. A. Usievich, V. A. Sychugov, J. Kh. Nirligareev, and K. M. Golant, *Opt. Spectrosc.* **97**, 790 (2004).
110. N. Chiodo, G. DellaValle, R. Osellame, S. Longhi, G. Cerullo, R. Ramponi, P. Laporta, and U. Morgner, *Opt. Lett.* **31**, 1651 (2006).
111. H. Trompeter, W. Krolikowski, D. N. Neshev, A. S. Desyatnikov, A.A. Sukhorukov, Yu. S. Kivshar, T. Pertsch, U. Peschel, and F. Lederer, *Phys. Rev. Lett.* **96**, 053903 (2006).
112. S. Longhi, *Opt. Lett.* **32**, 2647 (2007).
113. S. Longhi, "Bloch oscillations in complex crystals with PT symmetry," *Phys. Rev. Lett.* **103**, 123601 (2009).
114. K. G. Makris, R. El-Ganainy, D. N. Christodoulides, Z. H. Musslimani, "Beam dynamics in PT symmetric optical lattices," *Phys. Rev. Lett.* **100**, 103904 (2008).
115. N. Bahlmann, M. Lohmeyer, O. Zhuromsky, H. Dötsch, P. Hertel, "Nonreciprocal coupled waveguides for integrated optical isolators and circulators for TM-modes," *Optics Comm.* **161**, 330-337 (1999).
116. A. Erdmann, M. Shamonin, P. Hertel and H. Dötsch, *Optics Comm.* **102**, 25 (1993).

117. J. Fujita, M. Levy, R. M. Osgood, Jr., L. Wilkens, and H. Doetsch, IEEE Photonics Technol. Lett. **12**, 1510-1512 (2000).
118. H. Dötsch, P. Hertel, B. Lührmann, S. Sure, H.P. Winkler, and M. Ye, "Applications of magnetic garnet films in integrated optics," IEEE Trans. on Magnetism **28**, 2979-2984 (1992).
119. J. Fujita, M. Levy, R. M. Osgood, Jr., L. Wilkens, and H. Dötsch, "Polarization-Independent Waveguide Optical Isolator based on Nonreciprocal Phase Shift," IEEE Photonics Technol. Lett. **12**, 1510-1512 (2000).
120. H. Hemme, H. Dötsch, P. Hertel, "Integrated optical isolator based on nonreciprocal-mode cut-off," Appl. Optics **29**, 2741-2744 (1990).
121. W. Zhang, J.-W. Mu, W.-P. Huang, and W. Zhao, "Enhancement of nonreciprocal phase shift by magneto-optical slot waveguide with a compensation wall," Appl. Phys. Lett. **98**, 171109 (2011).
122. R. Chen, G. Jiang, Y. Hao, J. Yang, M. Wang, and X. Jaing, "Enhancement of nonreciprocal phase shift by using nanoscale air gap," Opt. Lett. **35**, 1335-1337 (2010).
123. R. L. Espinola, T. Izuhara, M.-C. Tsai, R. M. Osgood, Jr., and H. Dotch, "Magneto-optical nonreciprocal phase shift in garnet/silicon-on-insulator waveguides," Opt. Lett. **29**, 941-943 (2004) and references therein.
124. S. Wang, M. Shah, J. D. Crow, "Studies of the use of gyrotropic and anisotropic materials for mode conversion in thin-film optical-waveguide applications," J. Appl. Phys. **43** 1861-1875 (1972).
125. J. Fujita, M. Levy, R. M. Osgood, Jr., L. Wilkens, and H. Dotsch, "Waveguide optical isolator based on Mach-Zehnder interferometer," Appl. Phys. Lett. **76**, 2158-2160 (2000).
126. Y. Shoji, I. -W. Hsieh, R. M. Osgood, Jr., and T. Mizumoto, "Polarization-Independent Magneto-Optical Waveguide Isolator Using TM-Mode Nonreciprocal Phase Shift," J. Lightwave Technol. **25**, 3108-3113 (2007).
127. Z. Yu, and S. Fan, "Complete optical isolation created by indirect interband photonic transitions," Nat. Photon. **3**, 91-94 (2009).
128. Y. Shoji, T. Mizumoto, H. Yokoi, I.-W. Hsieh, and R. M. Osgood, Jr., "Magneto-optical isolator with silicon waveguides fabricated by direct bonding," Appl. Phys. Lett. **92**, 071117 (2008).
129. H. L. Lira, Z. Yu, M. Lipson, and S. Fan, "Electro-optical silicon isolator," in CLEO: Science and Innovations, OSA Technical Digest (online) paper CW1K.5 (2012).

Publications & Achievements

Peer-Reviewed Journal Articles

1. R. El-Ganainy, **Pradeep Kumar**, and Miguel Levy, "On-chip optical isolation based on non-reciprocal resonant delocalization effects," Optics Letters Vol. **38**, Issue 1, 61-63 (2013)
2. **Pradeep Kumar** and Miguel Levy, "On-chip optical isolation via unidirectional Bloch oscillations in a waveguide array," Optics Letters Vol. **37**, Issue 18, 3762-3764 (2012)
3. **Pradeep Kumar** and Miguel Levy, "Unidirectional optical Bloch oscillations in asymmetric waveguide arrays," Optics Letters Vol. **36**, Issue 22, 4359-4361 (2011)
4. Miguel Levy and **Pradeep Kumar**, "Nonreciprocal Bloch oscillations in magneto-optic waveguide arrays," Optics Letters Vol. **35**, Issue 18, 3147-3149 (2010)
5. **Pradeep Kumar**, A. I. Maydykovskiy, Miguel Levy, N. V. Dubrovina, O. A. Aktsipetrov, "Second harmonic generation study of internally-generated strain in bismuth-substituted iron garnet films," Optics Express Vol. **18**, Issue 2, 1076-1084 (2010)

Book Chapter

1. Miguel Levy, Ashim Chakravarty, **Pradeep Kumar** and Xiaoyue Huang, Chapter title: "Magnetophotonic Bragg Waveguides, Waveguide Arrays and Nonreciprocal Bloch Oscillations" in the Springer-Verlag Book: "Magnetophotonics: From Theory to Applications", Editors: M. Inoue, M. Levy and A. V. Baryshev. (Scheduled for publication in January 2013)

International Conference Proceedings

1. **Pradeep Kumar** and Miguel Levy, "Nonreciprocal optical Bloch oscillations in garnet/silicon-on-insulator waveguide arrays," Materials Research Society (MRS) Proceedings **1291**, mrsf10-1291-j02-03, Published online by Cambridge University Press (2011)
2. **Pradeep Kumar** and Miguel Levy, "Unidirectional Optical Bloch Oscillations in Garnet/Silicon-On-Insulator Waveguide Arrays," Conference on Lasers and Electro-Optics: Science and Innovations, OSA Technical Digest (online), paper CTu1A.7 (2012)

Oral/Poster Presentations at International Conferences

1. Oral presentation at the Conference on Lasers and Electro-Optics: Science & Innovation, May 08, 2012, San Jose, CA, USA, “Unidirectional Optical Bloch Oscillations in Garnet/Silicon-On-Insulator Waveguide Arrays,”
2. Oral presentation at the fall meeting of the Materials Research Society, Nov. 30, 2010, Boston MA, USA “Nonreciprocal optical Bloch oscillations in magneto-optic waveguide arrays”,
3. N.V. Dubrovina, **Pradeep Kumar**, M. Levy, A.I. Maydykovskiy, O.A. Aktsipetrov, “Influence of annealing on nonlinear optical response of Bismuth-substituted Iron garnet films, Moscow International Symposium on Magnetism (MISM), Aug. 21-25, 2011, Moscow State University, Moscow, Russia (poster)
4. A.I. Maydykovskiy, N.V. Dubrovina, O.A. Aktsipetrov, **Pradeep Kumar**, M. Levy and A.A. Jalali, “Study of correlation between mismatch and nonlinear optical properties of Bi-substituted garnet films”, European Materials Research Society (EMRS-Symposium H) Spring meeting June 2009, Strasbourg, France (abstract).

Achievements

- “Outstanding Scholarship Award (Fall 2012)”, Department of Physics, Michigan Tech. University
- “Doctoral Finishing Fellowship (Fall 2012)” Graduate School Michigan Tech. University

Appendix 1

Table A1.1. Bi:YIG films set-1 summary

No.	Film	Summary
1 [†]	BiYIG120507	Ar:20sccm, O ₂ :0.1sccm, 80W, 700°C, B. Pressure:50mT, C.Pressure:23.7mT, 2:00 Hrs
2	BiYIG113007	Ar:20sccm, 80W, 700°C, B. Pressure:50mT, C.Pressure:23.0mT, 3:00 Hrs
3	BiYIG112907	Ar:20sccm, 80W, 700°C, B. Pressure:50mT, C.Pressure:23.7mT, 2:00 Hrs
4	BiYIG111507	Ar:20sccm, O ₂ :0.2sccm, 80W, 700°C, B. Pressure:50mT, C.Pressure:23.7mT, 2:00 Hrs
5 [‡]	BiYIG082107	Ar:20sccm, 50W-80W, 710°C, B. Pressure:50mT, C.Pressure:23.2mT, 1:30-0:45 Hrs
6	BiYIG080607	Ar:20sccm, 80W, 710°C, B. Pressure:50mT, C.Pressure:23.0mT, 2:30 Hrs
7	BiYIG072407	Ar:20sccm, 80W, 710°C, B. Pressure:50mT, C.Pressure:21.6mT, 1:04 Hrs
8	BiYIG061407	Ar:15sccm, 70W, 710°C, B. Pressure:50mT, C.Pressure:22.8mT, 1:30 Hrs

[†] Films 1- 4 → Target: Bi_{0.8}Y_{2.2}Fe_{4.8}Ga_{0.2}O₁₂ (Left side, Distance from Substrate = 3.7cm)

[‡] Films 5-8 → Target: Bi_{0.8}Y_{2.2}Fe_{4.8}Ga_{0.2}O₁₂ (Right side, Distance from the Substrate = 4cm)

■ Films with Oxygen

Note: Due to the heat loss at the contact, there was about 150 °C temperature difference between the measured substrate surface temperature and the heater control temperature. Thus, the substrate temperature was ~ 550 °C when the set temperature of the heater controller was ~ 700 °C.

Table A1.2. Bi:YIG films set-2 summary

Target: $\text{Bi}_{0.8}\text{Y}_{2.2}\text{Fe}_4\text{Ga}_1\text{O}_{12}$ (Right side, Distance from Substrate = 4.5cm)		
No.	Film	Summary
1	BiYIG013108	Ar:20sccm, 80W, 700°C, B. Pressure:50mT, C.Pressure:23mT, 3:00 Hrs
2	BiYIG020208	Ar:20sccm, O_2 :0.1sccm, 80W, 700°C, B. Pressure:50mT, C.Pressure:22.8mT, 2:00 Hrs, (film with oxygen)
3	BiYIG021208	Ar:20sccm, 80W, 700°C, B. Pressure:50mT, C.Pressure:22.3mT, 2:00 Hrs
4	BiYIG021308	Ar:20sccm, 60-80W, 700°C, B. Pressure:50mT, C.Pressure:23.0mT, (1hr-1hr, total =2:00 Hrs)
5	GGG021508	Ar:20sccm, O_2 :0.1sccm, 700°C, B. Pressure:50mT, C.Pressure:18.5mT, 2:00Hrs, (GGG substrate was kept in chamber with given parameters without plasma)
6	BiYIG021808	Ar:20sccm, 80W, 700°C, B. Pressure:50mT, C.Pressure:21.9mT, 2:00 Hrs, (annealed in chamber with Ar:20sccm, O_2 :0.1sccm, 700°C, B. Pressure:50mT, C.Pressure:21.6mT, 2:00Hrs)
7	BiYIG022208	Ar:20sccm, 80W, 700°C, B. Pressure:50mT, C.Pressure:21.4mT, 2:00Hrs, (film on CMG:GGG substrate)
8	BiYIG030408	Ar:15sccm, 80W, 710°C, B. Pressure:50mT, C.Pressure:22.3mT, 2:00 Hrs
9	BiYIG030508	Ar:15sccm, 70W, 710°C, B. Pressure:50mT, C.Pressure:22.8mT, 2:00 Hrs
10	CMG:GGG	Pure substrate
11	GGG	Pure substrate

■ Films with Oxygen

Table A1.3. Bi:YIG films set-3 summary

No.	Film	Summary
1	BiYIG 042108	Ar:15sccm, 70W, 710°C, B. Pressure:50mT, C.Pressure:22.8mT, 2:00 Hrs {RT}
2	BiYIG 042208	Ar:20sccm, 80W, 710°C, B. Pressure:50mT, C.Pressure:21.8mT, 1:00Hr, {first layer-RT} C.Pressure:22.3mT, 1:00Hr, {second layer-LT}
3	BiYIG 050708	Ar:20sccm, 80W, 710°C, B. Pressure:50mT, C.Pressure:22.8mT, 1:00 Hr, {first layer-LT} C.Pressure:21.6mT, 1:00 Hr, {second layer-RT}
4	BiYIG 051208	Ar:20sccm, 80W, 710°C, B. Pressure:50mT, C.Pressure:21.9mT, 2:00 Hrs, {LT}
5	BiYIG 051308	Ar:20sccm, 80W, 710°C, B. Pressure:50mT, C.Pressure:21.4mT, 2:00 Hrs, {RT}

No.	Film with patterning	Comments	No.	Film with patterning	Comments
6	BiYIG 042108-P1	Three different patterning on BiYIG042108 film (see the attached sketch for set-3)	12	BiYIG 051308-P1	Three different patterning on BiYIG051308 film (see the attached sketch for set-3)
7	BiYIG 042108-P2		13	BiYIG 051308-P2	
8	BiYIG 042108-P3		14	BiYIG 051308-P3	
9	BiYIG 051208-P1	Three different patterning on BiYIG051208 film (see the attached sketch for set-3)	15	BiYIG 061107	FIB patterning, area 40X40 μm^2 , this area contains 20 lines (approx.), each line with a thickness of 900nm and separation 1 μm
10	BiYIG 051208-P2		16	BiYIG 100407	Symmetrical broken lines were created using Photolithography and Dry etching technique
11	BiYIG 051208-P3				

Right Target: $\text{Bi}_{0.8}\text{Y}_{2.2}\text{Fe}_4\text{Ga}_1\text{O}_{12}$ (Right side, Distance from Substrate = 4.5cm)

Left Target : $\text{Bi}_{0.8}\text{Y}_{2.2}\text{Fe}_{4.8}\text{Ga}_{0.2}\text{O}_{12}$ (Left side, Distance from Substrate = 3.7cm)

Right Target*: $\text{Bi}_{0.8}\text{Y}_{2.2}\text{Fe}_{4.8}\text{Ga}_{0.2}\text{O}_{12}$ (Right side, Distance from Substrate = 4cm)

Table A1.4. Bi:YIG films set-4 summary

No.	Film	Summary
1	BiYIG 082608	Ar:20sccm, 80W, 710°C, B. Pressure:50mT, C.Pressure:22.3mT, 3:00 Hrs {RT}
2	BiLuIG 100508	Ar:20sccm, 80W, 710°C, B. Pressure:50mT, C.Pressure:21.6mT, 2:00Hrs {RT**}
3	BiLuIG 100708	Ar:20sccm, 80W, 710°C, B. Pressure:50mT, C.Pressure:20.3mT, 3:00 Hrs, {RT**}
4	BiYIG 082608-P1	FIB patterning over gold (~25nm) coated BiYIG082608 film, grating period 500nm (see the BiYIG082608 sketch file). Gold coating time 15min , FIB line dose 25

RT: $\text{Bi}_{0.8}\text{Y}_{2.2}\text{Fe}_4\text{Ga}_1\text{O}_{12}$ (Right side, Distance from Substrate = 4.5cm)

RT**: $\text{Bi}_{1.5}\text{Lu}_{1.5}\text{Fe}_4\text{Ga}_1\text{O}_{12}$ (Right side, Distance from Substrate = 4.5cm)

Table A1.5. Bi:YIG films set-5 summary

No.	Film	Summary
1*	BiYLuIG111408	Ar:20sccm, 80W, 710°C, B. Pressure:50mT, 25min {LRLRL, 5 layers}
2*	BiYLuIG111708	Ar:20sccm, 80W, 710°C, B. Pressure:50mT, 50min {LR..LR, 10 layers}
3*	BiYLuIG111808	Ar:20sccm, 80W, 710°C, B. Pressure:50mT, 75min {LR...LRL, 15 layers}
4	BiYLuIG112108	Ar:20sccm, 80W, 710°C, B. Pressure:50mT, 25min {LRLRL, 5 layers}
5	BiYLuIG112308	Ar:20sccm, 80W, 710°C, B. Pressure:50mT, 50min {LR..LR, 10 layers}
6	BiYLuIG112408	Ar:20sccm, 80W, 710°C, B. Pressure:50mT, 75min {LR...LRL, 15 layers}

Left Target*: $\text{Bi}_{0.8}\text{Y}_{2.2}\text{Fe}_{4.8}\text{Ga}_{0.2}\text{O}_{12}$ (Left side, Distance from Substrate = 3.7cm) (for film number 1, 2 and 3 this target was used)

Left Target: $\text{Bi}_{0.8}\text{Y}_{2.2}\text{Fe}_4\text{Ga}_1\text{O}_{12}$ (Left side, Distance from Substrate = 3.7cm) (for film number 4, 5 and 6 this target was used)

Right Target: $\text{Bi}_{1.5}\text{Lu}_{1.5}\text{Fe}_4\text{Ga}_1\text{O}_{12}$ (Right side, Distance from Substrate = 4.5cm)

Note: LRLRL means alternating sputtering from Left Target and Right Target for 5 minutes each. So L stand for sputtering from Left Target and R stands for sputtering from right target. Similar convention is used for 10-layer and 15-layer films.

Appendix 2

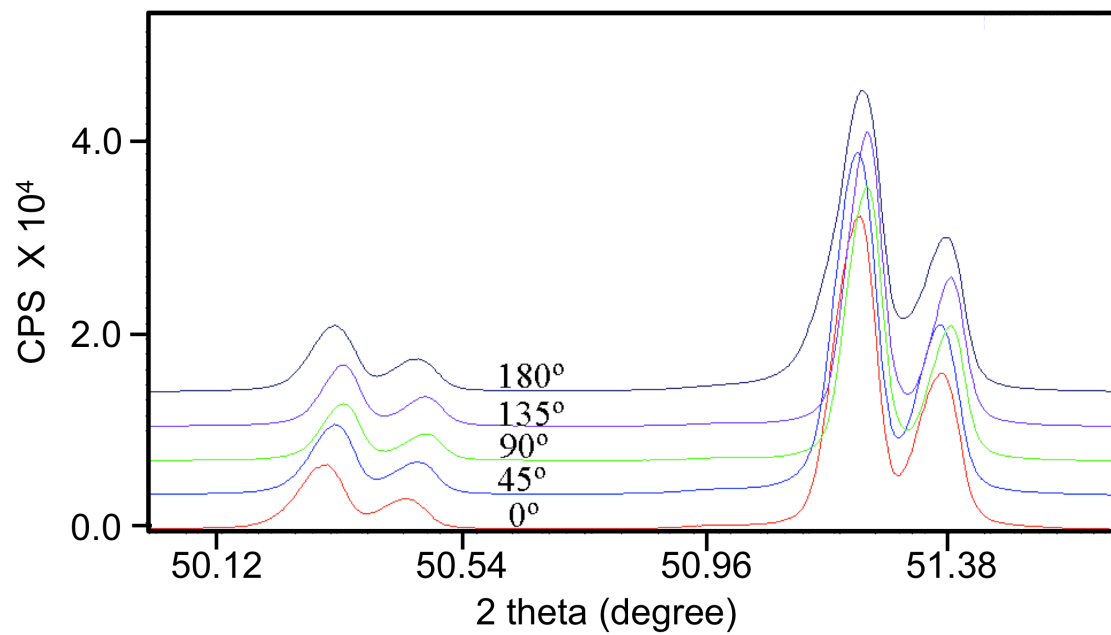


Fig. A2.1. XRD diffraction patterns of a typical sample at five different angles (0, 45, 90, 135 and 180 degree).

Appendix 3

Table A3.1. SHG results in PP geometry

Date	Right Target	Left Target	Max signal, a.u.	Min signal, a.u.	Difference (max-min), a.u.
061407	$\text{Bi}_{0.8}\text{Y}_{2.2}\text{Fe}_{4.8}\text{Ga}_{0.2}\text{O}_{12}$	-	54.7	4.7	50
072407	$\text{Bi}_{0.8}\text{Y}_{2.2}\text{Fe}_{4.8}\text{Ga}_{0.2}\text{O}_{12}$	-	7.7	1.0	6.7
080607	$\text{Bi}_{0.8}\text{Y}_{2.2}\text{Fe}_{4.8}\text{Ga}_{0.2}\text{O}_{12}$	-	9.1	1.7	7.4
082107	$\text{Bi}_{0.8}\text{Y}_{2.2}\text{Fe}_{4.8}\text{Ga}_{0.2}\text{O}_{12}$	-	3.9	1.6	2.3
111507	-	$\text{Bi}_{0.8}\text{Y}_{2.2}\text{Fe}_{4.8}\text{Ga}_{0.2}\text{O}_{12}$	5.3	2.5	2.8
112907	-	$\text{Bi}_{0.8}\text{Y}_{2.2}\text{Fe}_{4.8}\text{Ga}_{0.2}\text{O}_{12}$	6.8	1.9	4.9
113007	-	$\text{Bi}_{0.8}\text{Y}_{2.2}\text{Fe}_{4.8}\text{Ga}_{0.2}\text{O}_{12}$	51.3	5.8	45.5
120507	-	$\text{Bi}_{0.8}\text{Y}_{2.2}\text{Fe}_{4.8}\text{Ga}_{0.2}\text{O}_{12}$	2.8	1.5	1.3
013108	$\text{Bi}_{0.8}\text{Y}_{2.2}\text{Fe}_4\text{Ga}_1\text{O}_{12}$	-	11.8	2.8	9
020208	$\text{Bi}_{0.8}\text{Y}_{2.2}\text{Fe}_4\text{Ga}_1\text{O}_{12}$	-	13.8	8.2	5.6
021208	$\text{Bi}_{0.8}\text{Y}_{2.2}\text{Fe}_4\text{Ga}_1\text{O}_{12}$	-	6.2	3.2	3
021308	$\text{Bi}_{0.8}\text{Y}_{2.2}\text{Fe}_4\text{Ga}_1\text{O}_{12}$	-	13.9	8.1	5.8
021508	$\text{Bi}_{0.8}\text{Y}_{2.2}\text{Fe}_4\text{Ga}_1\text{O}_{12}$	-	0.8	0.3	0.5
021808	$\text{Bi}_{0.8}\text{Y}_{2.2}\text{Fe}_4\text{Ga}_1\text{O}_{12}$	-	6.0	4.6	1.4
022208	$\text{Bi}_{0.8}\text{Y}_{2.2}\text{Fe}_4\text{Ga}_1\text{O}_{12}$	-	30.8	15.8	15
030408	$\text{Bi}_{0.8}\text{Y}_{2.2}\text{Fe}_4\text{Ga}_1\text{O}_{12}$	-	1.9	0.5	1.4
030508	$\text{Bi}_{0.8}\text{Y}_{2.2}\text{Fe}_4\text{Ga}_1\text{O}_{12}$	-	15.3	2.6	12.7
CMG: GGG	-	-	94.6	14.2	80.4
GGG	-	-	0.5	0.3	0.2
042108	$\text{Bi}_{0.8}\text{Y}_{2.2}\text{Fe}_4\text{Ga}_1\text{O}_{12}$	-	4.7	0.3	4.4
042208	$\text{Bi}_{0.8}\text{Y}_{2.2}\text{Fe}_4\text{Ga}_1\text{O}_{12}$	$\text{Bi}_{0.8}\text{Y}_{2.2}\text{Fe}_{4.8}\text{Ga}_{0.2}\text{O}_{12}$	18.4	3.8	14.6
050708	$\text{Bi}_{0.8}\text{Y}_{2.2}\text{Fe}_{4.8}\text{Ga}_{0.2}\text{O}_{12}$	$\text{Bi}_{0.8}\text{Y}_{2.2}\text{Fe}_{4.8}\text{Ga}_{0.2}\text{O}_{12}$	9.4	0.6	8.8
051208	-	$\text{Bi}_{0.8}\text{Y}_{2.2}\text{Fe}_{4.8}\text{Ga}_{0.2}\text{O}_{12}$	11.6	0.3	11.3
051308	$\text{Bi}_{0.8}\text{Y}_{2.2}\text{Fe}_4\text{Ga}_1\text{O}_{12}$	-	51.5	11.5	40
061107	$\text{Bi}_{0.8}\text{Y}_{2.2}\text{Fe}_{4.8}\text{Ga}_{0.2}\text{O}_{12}$	-	9.3	2.6	6.7
100407	$\text{Bi}_{0.8}\text{Y}_{2.2}\text{Fe}_{4.8}\text{Ga}_{0.2}\text{O}_{12}$	-	4.6	1.7	2.9
082608	$\text{Bi}_{0.8}\text{Y}_{2.2}\text{Fe}_4\text{Ga}_1\text{O}_{12}$	-	18.1	7.1	11
100508	$\text{Bi}_{1.5}\text{Lu}_{1.5}\text{Fe}_4\text{Ga}_1\text{O}_{12}$	-	3.5	1.3	2.2
100708	$\text{Bi}_{1.5}\text{Lu}_{1.5}\text{Fe}_4\text{Ga}_1\text{O}_{12}$	-	5.7	1.0	4.7
111408	$\text{Bi}_{1.5}\text{Lu}_{1.5}\text{Fe}_4\text{Ga}_1\text{O}_{12}$	$\text{Bi}_{0.8}\text{Y}_{2.2}\text{Fe}_{4.8}\text{Ga}_{0.2}\text{O}_{12}$	6.6	0.9	5.7
111708	$\text{Bi}_{1.5}\text{Lu}_{1.5}\text{Fe}_4\text{Ga}_1\text{O}_{12}$	$\text{Bi}_{0.8}\text{Y}_{2.2}\text{Fe}_{4.8}\text{Ga}_{0.2}\text{O}_{12}$	2.5	0.6	1.9
111808	$\text{Bi}_{1.5}\text{Lu}_{1.5}\text{Fe}_4\text{Ga}_1\text{O}_{12}$	$\text{Bi}_{0.8}\text{Y}_{2.2}\text{Fe}_{4.8}\text{Ga}_{0.2}\text{O}_{12}$	10.8	4.0	6.8
112108	$\text{Bi}_{1.5}\text{Lu}_{1.5}\text{Fe}_4\text{Ga}_1\text{O}_{12}$	$\text{Bi}_{0.8}\text{Y}_{2.2}\text{Fe}_4\text{Ga}_1\text{O}_{12}$	14.4	11.0	3.4
112308	$\text{Bi}_{1.5}\text{Lu}_{1.5}\text{Fe}_4\text{Ga}_1\text{O}_{12}$	$\text{Bi}_{0.8}\text{Y}_{2.2}\text{Fe}_4\text{Ga}_1\text{O}_{12}$	8.4	0.6	7.8
112408	$\text{Bi}_{1.5}\text{Lu}_{1.5}\text{Fe}_4\text{Ga}_1\text{O}_{12}$	$\text{Bi}_{0.8}\text{Y}_{2.2}\text{Fe}_4\text{Ga}_1\text{O}_{12}$	23.8	13.5	10.3

Table A3.2. SHG results in PS geometry

Date	Right Target	Left Target	Max signal, a.u.	Min signal, a.u.	Difference (max-min), a.u.
061407	$\text{Bi}_{0.8}\text{Y}_{2.2}\text{Fe}_{4.8}\text{Ga}_{0.2}\text{O}_{12}$	-	6.4	0.9	5.5
072407	$\text{Bi}_{0.8}\text{Y}_{2.2}\text{Fe}_{4.8}\text{Ga}_{0.2}\text{O}_{12}$	-	2.0	0.3	1.7
080607	$\text{Bi}_{0.8}\text{Y}_{2.2}\text{Fe}_{4.8}\text{Ga}_{0.2}\text{O}_{12}$	-	?	?	?
082107	$\text{Bi}_{0.8}\text{Y}_{2.2}\text{Fe}_{4.8}\text{Ga}_{0.2}\text{O}_{12}$	-	1.9	0.7	1.2
111507	-	$\text{Bi}_{0.8}\text{Y}_{2.2}\text{Fe}_{4.8}\text{Ga}_{0.2}\text{O}_{12}$	1.2	0.7	0.5
112907	-	$\text{Bi}_{0.8}\text{Y}_{2.2}\text{Fe}_{4.8}\text{Ga}_{0.2}\text{O}_{12}$	2.1	0.9	1.2
113007	-	$\text{Bi}_{0.8}\text{Y}_{2.2}\text{Fe}_{4.8}\text{Ga}_{0.2}\text{O}_{12}$	22.4	1.1	21.3
120507	-	$\text{Bi}_{0.8}\text{Y}_{2.2}\text{Fe}_{4.8}\text{Ga}_{0.2}\text{O}_{12}$	1.5	0.7	0.8
013108	$\text{Bi}_{0.8}\text{Y}_{2.2}\text{Fe}_4\text{Ga}_1\text{O}_{12}$	-	4.0	1.3	2.7
020208	$\text{Bi}_{0.8}\text{Y}_{2.2}\text{Fe}_4\text{Ga}_1\text{O}_{12}$	-	8.9	5.5	3.4
021208	$\text{Bi}_{0.8}\text{Y}_{2.2}\text{Fe}_4\text{Ga}_1\text{O}_{12}$	-	1.7	0.3	1.4
021308	$\text{Bi}_{0.8}\text{Y}_{2.2}\text{Fe}_4\text{Ga}_1\text{O}_{12}$	-	1.7	0.2	1.5
021508	$\text{Bi}_{0.8}\text{Y}_{2.2}\text{Fe}_4\text{Ga}_1\text{O}_{12}$	-	0.5	0.2	0.3
021808	$\text{Bi}_{0.8}\text{Y}_{2.2}\text{Fe}_4\text{Ga}_1\text{O}_{12}$	-	0.3	0.1	0.2
022208	$\text{Bi}_{0.8}\text{Y}_{2.2}\text{Fe}_4\text{Ga}_1\text{O}_{12}$	-	28.2	15.8	12.4
030408	$\text{Bi}_{0.8}\text{Y}_{2.2}\text{Fe}_4\text{Ga}_1\text{O}_{12}$	-	1.1	0.2	0.9
030508	$\text{Bi}_{0.8}\text{Y}_{2.2}\text{Fe}_4\text{Ga}_1\text{O}_{12}$	-	4.7	0.2	4.5
CMG: GGG	-	-	90.1	18.7	71.4
GGG	-	-	0.5	0.2	0.3
042108	$\text{Bi}_{0.8}\text{Y}_{2.2}\text{Fe}_4\text{Ga}_1\text{O}_{12}$	-	1.6	0.3	1.3
042208	$\text{Bi}_{0.8}\text{Y}_{2.2}\text{Fe}_4\text{Ga}_1\text{O}_{12}$	$\text{Bi}_{0.8}\text{Y}_{2.2}\text{Fe}_{4.8}\text{Ga}_{0.2}\text{O}_{12}$	2.0	0.1	1.9
050708	$\text{Bi}_{0.8}\text{Y}_{2.2}\text{Fe}_{4.8}\text{Ga}_{0.2}\text{O}_{12}$	$\text{Bi}_{0.8}\text{Y}_{2.2}\text{Fe}_{4.8}\text{Ga}_{0.2}\text{O}_{12}$	6.5	0.2	6.3
051208	-	$\text{Bi}_{0.8}\text{Y}_{2.2}\text{Fe}_{4.8}\text{Ga}_{0.2}\text{O}_{12}$	5.0	0.1	4.9
051308	$\text{Bi}_{0.8}\text{Y}_{2.2}\text{Fe}_4\text{Ga}_1\text{O}_{12}$	-	18.3	0.2	18.1
061107	$\text{Bi}_{0.8}\text{Y}_{2.2}\text{Fe}_{4.8}\text{Ga}_{0.2}\text{O}_{12}$	-	6.6	1.8	4.8
100407	$\text{Bi}_{0.8}\text{Y}_{2.2}\text{Fe}_{4.8}\text{Ga}_{0.2}\text{O}_{12}$	-	2.7	1.0	1.7
082608	$\text{Bi}_{0.8}\text{Y}_{2.2}\text{Fe}_4\text{Ga}_1\text{O}_{12}$	-	1.5	0.2	1.3
100508	$\text{Bi}_{1.5}\text{Lu}_{1.5}\text{Fe}_4\text{Ga}_1\text{O}_{12}$	-	0.5	0.2	0.3
100708	$\text{Bi}_{1.5}\text{Lu}_{1.5}\text{Fe}_4\text{Ga}_1\text{O}_{12}$	-	1.0	0.4	0.6
111408	$\text{Bi}_{1.5}\text{Lu}_{1.5}\text{Fe}_4\text{Ga}_1\text{O}_{12}$	$\text{Bi}_{0.8}\text{Y}_{2.2}\text{Fe}_{4.8}\text{Ga}_{0.2}\text{O}_{12}$	3.4	0.2	3.2
111708	$\text{Bi}_{1.5}\text{Lu}_{1.5}\text{Fe}_4\text{Ga}_1\text{O}_{12}$	$\text{Bi}_{0.8}\text{Y}_{2.2}\text{Fe}_{4.8}\text{Ga}_{0.2}\text{O}_{12}$	1.5	0.2	1.3
111808	$\text{Bi}_{1.5}\text{Lu}_{1.5}\text{Fe}_4\text{Ga}_1\text{O}_{12}$	$\text{Bi}_{0.8}\text{Y}_{2.2}\text{Fe}_{4.8}\text{Ga}_{0.2}\text{O}_{12}$	3.0	0.2	2.8
112108	$\text{Bi}_{1.5}\text{Lu}_{1.5}\text{Fe}_4\text{Ga}_1\text{O}_{12}$	$\text{Bi}_{0.8}\text{Y}_{2.2}\text{Fe}_4\text{Ga}_1\text{O}_{12}$	0.7	0.2	0.5
112308	$\text{Bi}_{1.5}\text{Lu}_{1.5}\text{Fe}_4\text{Ga}_1\text{O}_{12}$	$\text{Bi}_{0.8}\text{Y}_{2.2}\text{Fe}_4\text{Ga}_1\text{O}_{12}$	4.0	0.2	3.8
112408	$\text{Bi}_{1.5}\text{Lu}_{1.5}\text{Fe}_4\text{Ga}_1\text{O}_{12}$	$\text{Bi}_{0.8}\text{Y}_{2.2}\text{Fe}_4\text{Ga}_1\text{O}_{12}$	0.8	0.3	0.5

Appendix 4

TM mode equation

Appendix 4

magnetic field components:

$$\left\{ \begin{aligned} & \left(\frac{\partial^2}{\partial x^2} + \frac{\partial^2}{\partial y^2} + \frac{\partial^2}{\partial z^2} - i g \frac{\partial}{\partial x} \frac{1}{\epsilon} \frac{\partial}{\partial z} + \omega^2 \mu_0 \epsilon_0 \epsilon \right) H_x \\ & + i \left(g \frac{\partial}{\partial x} \frac{1}{\epsilon} \frac{\partial}{\partial x} + \omega^2 \mu_0 \epsilon_0 g \right) H_z = 0 \end{aligned} \right. \quad (1)$$

$$\left\{ \begin{aligned} & \left(\frac{\partial^2}{\partial x \partial y} - \epsilon \frac{\partial}{\partial x} \frac{1}{\epsilon} \frac{\partial}{\partial y} - i \frac{g}{\epsilon} \frac{\partial^2}{\partial y \partial z} \right) H_x \\ & + \left(\epsilon \frac{\partial}{\partial x} \frac{1}{\epsilon} \frac{\partial}{\partial x} + \frac{\partial^2}{\partial y^2} + \frac{\partial^2}{\partial z^2} + \omega^2 \mu_0 \epsilon_0 \epsilon + i \frac{g}{\epsilon} \frac{\partial^2}{\partial x \partial z} \right. \\ & \quad \left. - i \epsilon \frac{\partial}{\partial x} \frac{g}{\epsilon^2} \frac{\partial}{\partial y} \right) H_y \\ & + i \left(\epsilon \frac{\partial}{\partial x} \frac{g}{\epsilon^2} \frac{\partial}{\partial y} \right) H_z = 0 \end{aligned} \right. \quad (2)$$

$$\left\{ \begin{aligned} & \left(i \frac{\partial^2}{\partial x \partial z} - i \epsilon \frac{\partial}{\partial x} \frac{1}{\epsilon} \frac{\partial}{\partial z} + \frac{g}{\epsilon} \frac{\partial^2}{\partial z^2} \right) H_x \\ & + i \left(\epsilon \frac{\partial}{\partial x} \frac{1}{\epsilon} \frac{\partial}{\partial x} + \frac{\partial^2}{\partial y^2} + \frac{\partial^2}{\partial z^2} + i \frac{g}{\epsilon} \frac{\partial^2}{\partial x \partial z} \right) H_z = 0 \end{aligned} \right. \quad (3)$$

these equation can be specialized to mode along z -direction
 $\rightarrow (\exp(i\beta z))$ and assuming that TM mode satisfies
 $H_y \gg H_x, H_z$ (quasi-TM)

Fig. A4.1. Intermediate terms in TM mode Eq. (4.27).

Appendix 5

MATLAB code main file for Ce:YIG/SOI material combination (see Fig. 4.10)

```
% Matlab script :- [TM mode nonreciprocal phase shift(difference)calculation for a Slab
% Waveguide made in a silicon substrate with a magnetic garnet cover layer].

% This is the main file that calls 'dF_SOI.m' {forward propagation} and
%'dB_SOI.m'{backward propagation} files

% [Note: program will not work without the forward and backward files]

% Original Date: Jan 06, 2011 [by Pradeep Kumar], Revised: December 10, 2012[by
%Pradeep Kumar]

clear all

clc;

d=linspace(0,2,10000);          %film thickness in micrometer (start, end, steps)

f_mode=zeros(length(d),1);

b_mode=zeros(length(d),1);

dbeta=zeros(length(d),1);

for i=1:length(d)

    if(d(i)<.22)

        bzero = 9.789;

    else

        bzero = 12;

    end

    f_mode(i)=fzero(@(x) d(i)-dF_SOI(x),bzero);

    b_mode(i)=fzero(@(x) d(i)-dB_SOI(x),bzero);

    dbeta(i)=f_mode(i) - b_mode(i);
```

```

end

plot(d',abs(dbeta))          %film thickness(d) Vs delta beta plot

%plot(d',f_mode);           %film thickness(d) Vs forward mode plot

%plot(d',b_mode);           %film thickness(d) Vs backward mode plot

xlabel('film thickness(d) (um)') % this generates label for X-axis

ylabel('delta beta (1/um)')   % this generates label for Y-axis

title('wa=1550nm nf=3.44, ns=1.45, nc=2.22, Exz=0.0086') % this generates title of the
%graph

[d',f_mode,b_mode,dbeta] % this generates forward mode(f_mode), backward
%mode(b_mode) and delta beta(dbeta) for a given film thickness(d)

```

MATLAB code dF_SOI file

```

function d = dF_SOI(x)      % file for FW direction

wa=1.55;                    % wavelength in micrometer

Ef=11.8336;                % Si core index =3.44

Exx=4.9284;                % MO cover layer index = 2.22

Ezz=4.9284;

Exz=0.0086;                % off diagonal gyrotropic term,  $Exz \sim (2 \cdot n_0 \cdot \text{abs}(\text{FR angle}))/k_0$ ,
cover layer is Ce:YIG with FR  $\sim 4500$  deg/cm

Es=2.1025;                 % SiO2 substrate index=1.45

k0=(2*pi)/wa;              % vacuum wavenumber

Eeff=Ezz-Exz^2/Exx;        % effective index

kx=sqrt(k0^2*Ef-x^2);

kc=sqrt(x^2-k0^2*Eeff);

ks=sqrt(x^2-k0^2*Es);

```

% [TM mode dispersion relation in a slab waveguide with magnetic garnet cover layer,
% d=film thickness of core layer, x= propagation constant]

% The following equation is for the Forward direction

$$d = (\text{atan}((E_f/k_x)*((k_c/E_{\text{eff}})+(x*E_{xz})/(E_{xx}*E_{\text{eff}})))+ \text{atan}((E_f/k_x)*(k_s/E_s)))/k_x;$$

MATLAB code dB_SOI file

```
function d = dB_SOI(x)      % file for BW direction

wa=1.55;                    % wavelength in micrometer

Ef=11.8336;                 % Si core index =3.44

Exx=4.9284;                 % MO cover layer index = 2.22

Ezz=4.9284;

Exz=0.0086;                % off diagonal gyrotropic term, Exz~(2*n0*abs(FR angle))/k0,
cover layer is Ce:YIG with FR ~ 4500 deg/cm

Es=2.1025;                  % SiO2 substrate index=1.45

k0=(2*pi)/wa;              % vacuum wavenumber

Eeff=Ezz-Exz^2/Exx;        % effective index

kx=sqrt(k0^2*Ef-x^2);

kc=sqrt(x^2-k0^2*Eeff);

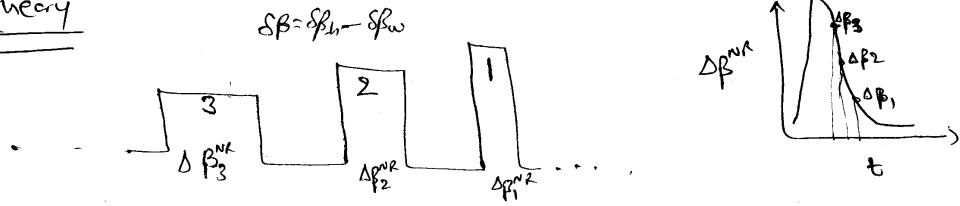
ks=sqrt(x^2-k0^2*Es);

% The following equation is for the Backward direction

d = (\text{atan}((E_f/k_x)*((k_c/E_{\text{eff}})-(x*E_{xz})/(E_{xx}*E_{\text{eff}})))+ \text{atan}((E_f/k_x)*(k_s/E_s)))/k_x;
```


Appendix 6

(1) theory



$$\Delta \beta_3^{NR} > \Delta \beta_2^{NR} > \Delta \beta_1^{NR} ; \quad \Delta \beta_3 - \Delta \beta_2 = \Delta \beta_2 - \Delta \beta_1 = \Delta \Delta \beta$$

WG 3

$$\text{FW: } \beta_3^f = \beta_0 + \frac{\Delta \beta_3}{2} ; \quad \text{WG 2} \quad \text{FW: } \beta_2^f = \beta_0 + \Delta \beta + \frac{\Delta \beta_2}{2} ; \quad \text{WG 1} \quad \beta_1^f = \beta_0 + 2\Delta \beta + \frac{\Delta \beta_1}{2}$$

$$\text{BW: } \beta_3^b = \beta_0 - \frac{\Delta \beta_3}{2} ; \quad \beta_2^b = \beta_0 + \Delta \beta - \frac{\Delta \beta_2}{2} ; \quad \beta_1^b = \beta_0 + 2\Delta \beta - \frac{\Delta \beta_1}{2}$$

WG 23

$$\text{FW: } \Delta \beta^f = \beta_2^f - \beta_3^f = \cancel{\beta_0} + \Delta \beta + \frac{\Delta \beta_2}{2} - \cancel{\beta_0} - \frac{\Delta \beta_3}{2} = \Delta \beta + \frac{1}{2}(\Delta \beta_2 - \Delta \beta_3) = \Delta \beta - \frac{\Delta \Delta \beta}{2}$$

$$\text{BW: } \Delta \beta^b = \beta_2^b - \beta_3^b = \cancel{\beta_0} + \Delta \beta - \frac{\Delta \beta_2}{2} - \cancel{\beta_0} + \frac{\Delta \beta_3}{2} = \Delta \beta - \frac{1}{2}(\Delta \beta_2 - \Delta \beta_3) = \Delta \beta + \frac{\Delta \Delta \beta}{2}$$

WG 12

$$\text{FW: } \Delta \beta^f = \beta_1^f - \beta_2^f = \cancel{\beta_0} + \Delta \beta + \frac{\Delta \beta_1}{2} - \cancel{\beta_0} - \Delta \beta - \frac{\Delta \beta_2}{2} = \Delta \beta + \frac{1}{2}(\Delta \beta_1 - \Delta \beta_2) = \Delta \beta - \frac{\Delta \Delta \beta}{2}$$

$$\text{BW: } \Delta \beta^b = \beta_1^b - \beta_2^b = \cancel{\beta_0} + \Delta \beta - \frac{\Delta \beta_1}{2} - \cancel{\beta_0} - \Delta \beta + \frac{\Delta \beta_2}{2} = \Delta \beta - \frac{1}{2}(\Delta \beta_1 - \Delta \beta_2) = \Delta \beta + \frac{\Delta \Delta \beta}{2}$$

$$\text{Bloch period } (L_B) = \frac{2\pi}{\Delta \beta^{fb}} = \frac{\lambda}{\Delta n} , \quad \text{WG spread} \approx \frac{8k}{\Delta \beta^{fb}}$$

Fig. A6.1. Nonreciprocal delta beta calculation of Eq. (4.29).

Appendix 7

Page - 1

Derivation of Bloch modes of the array

$$i \frac{d}{dz} a_n + \alpha_n a_n + a_{n+1} + a_{n-1} = 0 \quad (1)$$

$$a_n \rightarrow a_n(z), \quad \alpha = s\beta/k, \quad z = kz$$

$$a_n = \frac{1}{\sqrt{2\pi}} \int_{-\pi}^{\pi} \tilde{a}(k, z) e^{ikn} dk \quad \text{coupling constant} \quad (2)$$

Using (2) in (1),

$$i \frac{d}{dz} a_n = \frac{1}{\sqrt{2\pi}} \int_{-\pi}^{\pi} i \frac{d}{dz} \tilde{a}(k, z) e^{ikn} dk \rightarrow \text{(first term in (1))} \quad (3)$$

$$\begin{aligned} \alpha_n a_n &= \frac{1}{\sqrt{2\pi}} \int_{-\pi}^{\pi} \tilde{a}(k, z) \alpha_n e^{ikn} dk \\ \text{(2nd term in (1))} &= \frac{1}{\sqrt{2\pi}} \int_{-\pi}^{\pi} \tilde{a}(k, z) \alpha \left(-i \frac{d}{dk} e^{ikn} \right) dk \\ &= \frac{\alpha}{\sqrt{2\pi}} \left[\tilde{a}(\pi, z) e^{i\pi n} - \tilde{a}(-\pi, z) e^{i\pi n} \right] \\ &\quad + \frac{1}{\sqrt{2\pi}} \int_{-\pi}^{\pi} i \left(\frac{d}{dk} \tilde{a}(k, z) \right) \alpha e^{ikn} dk \\ &= \alpha \cdot \frac{1}{\sqrt{2\pi}} \int_{-\pi}^{\pi} \left(i \frac{d}{dk} \tilde{a}(k, z) \right) e^{ikn} dk \quad (4) \end{aligned}$$

$$a_{n+1} + a_{n-1} = \frac{1}{\sqrt{2\pi}} \int_{-\pi}^{\pi} \tilde{a}(k, z) e^{ikz} (e^{ik} + e^{-ik}) dk \quad \text{(3rd term in (1))} \quad (5)$$

Fig. A7.1. Page-1 of the derivation for the field dynamics in the coupled array structure Eq. (4.30).

Using eqns. (3), (4), and (5) in eqn (1), we get

$$i \frac{d}{dz} \tilde{a}(k, z) + i\alpha \frac{d}{dk} \tilde{a}(k, z) + 2(\cos k) \tilde{a}(k, z) = 0 \quad (6)$$

field amplitude

$$\begin{aligned} \tilde{a}_m(z) &= e^{i\beta_m z} \frac{1}{\sqrt{2\pi}} \int_{-\pi}^{\pi} \tilde{u}(k) e^{ikn} dk \\ &= \frac{1}{\sqrt{2\pi}} \int_{-\pi}^{\pi} \tilde{u}(k) e^{ikn} e^{i\beta_m z} dk \end{aligned}$$

$$\tilde{a}_m(k, z) = \tilde{u}_m(k) e^{i\beta_m z} \quad (7)$$

Using (7) in (6),

$$\begin{aligned} \Rightarrow i(i\beta_m) \tilde{u}(k) + i\alpha \frac{d\tilde{u}}{dk} + 2(\cos k) \tilde{u}(k) &= 0 \\ -\beta_m \tilde{u}(k) + i\alpha \frac{d\tilde{u}}{dk} + 2\cos k \tilde{u}(k) &= 0 \end{aligned}$$

$$\frac{d\tilde{u}}{dk} = -\frac{i}{\alpha} [-2\cos k + \beta_m] \tilde{u}$$

$$\tilde{u}(k) = \exp\left[-\frac{i}{\alpha} (\beta_m k - 2\sin k)\right] \quad (8)$$

Now, since $\tilde{u}(k)$ is periodic in k , with $\tilde{u}(-\pi) = \tilde{u}(\pi)$

then from eqn (8), $\exp\left[-\frac{i}{\alpha} \beta_m (-\pi)\right] = \exp\left[-\frac{i}{\alpha} \beta_m (\pi)\right]$

$$\therefore \boxed{\beta_m = m\alpha} \quad (9)$$

$m = 1, 2, 3, \dots$

Fig. A7.2. Page-2 of the derivation for the field dynamics in the coupled array structure Eq. (4.30).

Page-3

Now, let's look at the mode shape for $m=0$, mode.

$$\begin{aligned}
 U_n^0 &= \frac{1}{\sqrt{2\pi}} \int_{-\pi}^{\pi} e^{(i\frac{2\sin k}{\alpha})} \cdot e^{ikn} dk \\
 &= \frac{1}{\sqrt{2\pi}} \int_{-\pi}^{\pi} \exp\left(\frac{2j}{\alpha} \sin k + jkn\right) dk \\
 U_n^0 &= \sqrt{2\pi} J_{-n}\left(\frac{2}{\alpha}\right) \quad \text{---(10)}
 \end{aligned}$$

this is the amplitude of the supermode of the array ($m=0$) at waveguide 'n'.

[Ref. Peschel et. al. Optics Letters vol 23, No. 21, page 1701-1703 [1998].]

Fig. A7.3. Page-3 of the derivation for the field dynamics in the coupled array structure Eq. (4.30).

Appendix 8

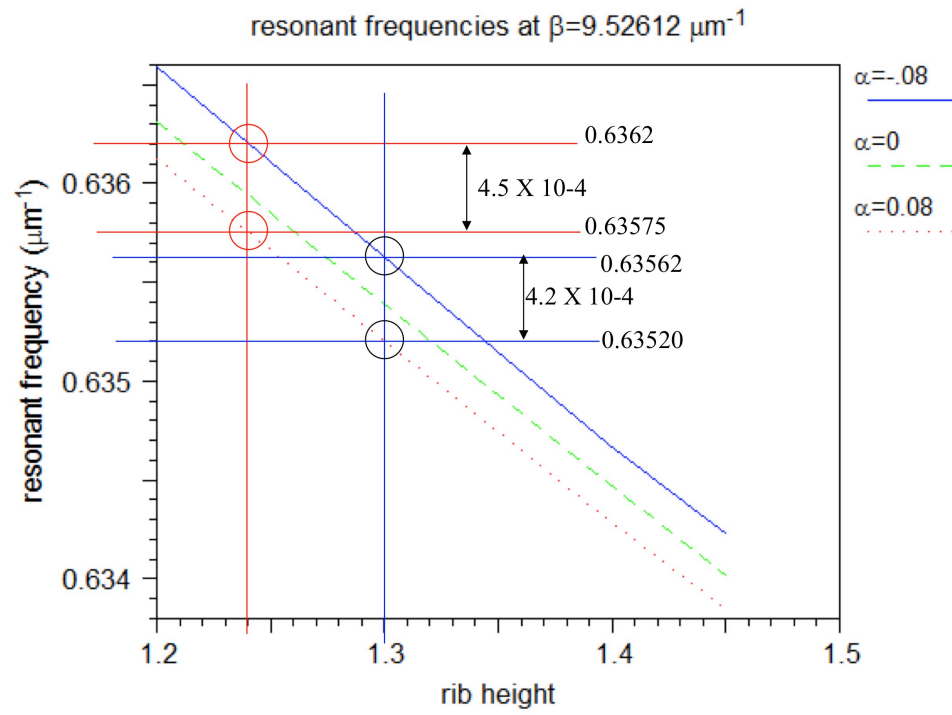


Fig. A8.1. FDTD calculation.

Differential NRPS calculation and comparison between various methods

FDTD calculations: -

$$\Delta\beta_1^{nr} = 3.322230 \times 10^{-4} \mu m^{-1} \quad [\text{after dividing by 20, WG } t = 1.24 \mu m]$$

$$\Delta\beta_2^{nr} = 3.100752 \times 10^{-4} \mu m^{-1} \quad [\text{after dividing by 20, WG } t = 1.30 \mu m]$$

$$\Rightarrow \Delta(\Delta\beta^{nr}) \sim 22 \text{ } m^{-1}$$

Perturbation Eq.: -

$$\Rightarrow \Delta(\Delta\beta^{nr}) \sim 14 \text{ } m^{-1}$$

TM mode Eq. for slab (MATLAB program): -

$$\Delta\beta_1^{nr} = 3.610 \times 10^{-4} \mu m^{-1} \quad [\text{WG } t = 1.24 \mu m]$$

$$\Delta\beta_2^{nr} = 3.275 \times 10^{-4} \mu m^{-1} \quad [\text{WG } t = 1.30 \mu m]$$

$$\Rightarrow \Delta(\Delta\beta^{nr}) \sim 33.5 \text{ } m^{-1}$$

Average over WG array $t = 1.24$ to $1.70 \mu m$: -

$$\Delta\beta_1^{nr} = 3.61 \times 10^{-4} \mu m^{-1} \quad [\text{WG } t = 1.24 \mu m]$$

$$\Delta\beta_9^{nr} = 1.80 \times 10^{-4} \mu m^{-1} \quad [\text{WG } t = 1.70 \mu m]$$

$$\Rightarrow \text{Avg. } \Delta(\Delta\beta^{nr}) \sim 22.6 \text{ } m^{-1}$$

Appendix 9

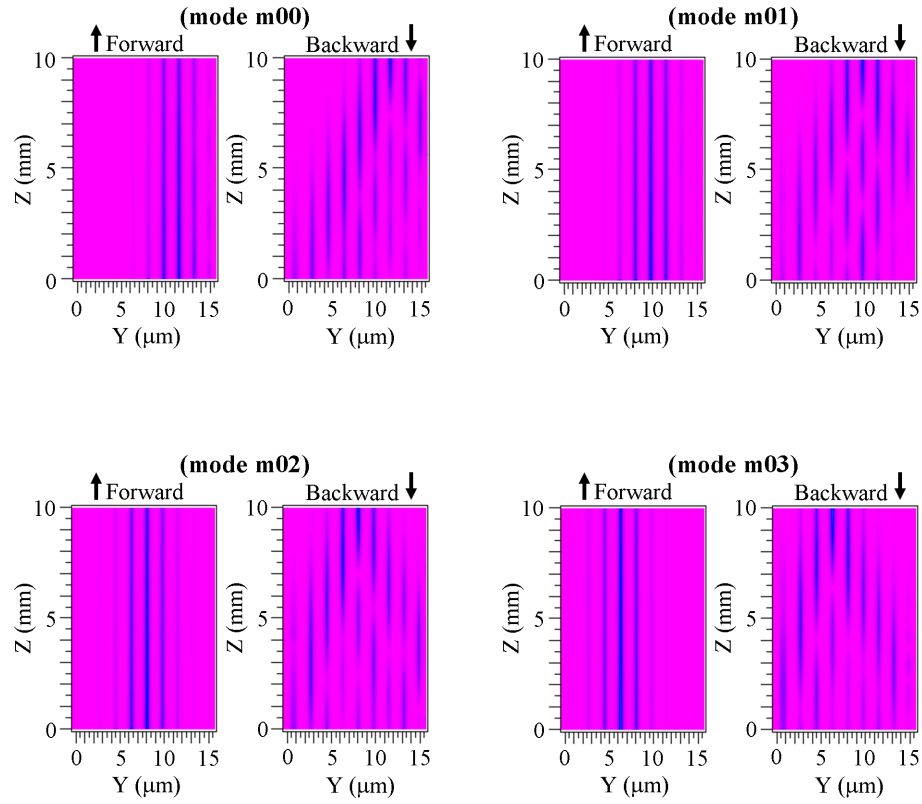


Fig. A9.1. BPM simulation graphs showing FW and BW propagation of normal modes (supermodes) of the array structure. Note that normal modes maintain constant amplitude and width in FW direction, whereas they diffract out in BW direction.

Appendix 10

Permissions from Authors/Companies to reproduce, text and images, from published work in the present dissertation.

Permission for Fig. 2.2

On Thu, Dec 6, 2012 at 1:21 AM, Haichun Yang <haichun@gmail.com> wrote:

Hi Pradeep,

I have no problem with that. Good luck on your thesis writing and Ph.D defnese.

Best,

Haichun

On Mon, Dec 3, 2012 at 7:48 PM, Pradeep Kumar <pradeepk@mtu.edu> wrote:

Dear Haichun,

I wanted to use a figure (Figure 1.4 Arrangement of cations in a YIG formula unit) from your PhD dissertation. I liked this figure and wanted to reproduce in my dissertation, of course only if you allow me to use it.

I am looking forward to your prompt reply.

Best

Pradeep

Permission for Fig. 2.8

Dear Mr. Pradeep Kumar,

Thank you for placing your order through Copyright Clearance Center's RightsLink service. American Institute of Physics has partnered with RightsLink to license its content. This notice is a confirmation that your order was successful.

Order Details

Licensee: Pradeep Kumar

License Date: Jan 3, 2013

License Number: 3061140861323

Publication: Applied Physics Letters

Title: Gyrotropic photonic crystal waveguide switches

Type Of Use: Thesis/Dissertation

Total: 0.00 USD

Permission for Fig. 2.9

Dear Mr. Pradeep Kumar,
Thank you for placing your order through Copyright Clearance Center's RightsLink service. American Institute of Physics has partnered with RightsLink to license its content. This notice is a confirmation that your order was successful.

Order Details

Licensee: Pradeep Kumar

License Date: Jan 3, 2013

License Number: 3061151351264

Publication: Applied Physics Letters

Title: Magneto-photonic crystal optical sensors with sensitive covers

Type Of Use: Thesis/Dissertation

Total: 0.00 USD

Permission for Fig. 2.11

On Thu, Dec 13, 2012 at 5:20 PM, Tetsuya
MIZUMOTO <tmizumot@pe.titech.ac.jp> wrote:

Dear Pradeep,
Yes, I am happy to give you permission to reproduce the figure you mention.

Best regards.

Copyright permission from the Optical Society of America (OSA) to reproduce text and images from reference [24], [25], [42], and [105] in Chapter 3 and Chapter 4 of this dissertation

On Mon, Jan 14, 2013 at 11:35 AM, pubscopyright <copyright@osa.org> wrote:
Dear Pradeep Kumar,

Thank you for contacting The Optical Society.

Because you are the author of the source paper from which you wish to reproduce material, OSA considers your requested use of its copyrighted materials to be permissible within the author rights granted in the Copyright Transfer Agreement submitted by the requester on acceptance for publication of his/her manuscript. It is

requested that a complete citation of the original material be included in any publication. This permission assumes that the material was not reproduced from another source when published in the original publication.

Please let me know if you have any questions.

Kind Regards,

Susannah Lehman

Susannah Lehman
January 14, 2013
Authorized Agent, The Optical Society

From: Pradeep Kumar [mailto:pradeepk@mtu.edu]
Sent: Friday, January 11, 2013 4:36 PM
To: pubscopyright
Subject: Copyright permission request

Dear OSA Staff,

I am writing to request your permission, as copyright holder, to reproduce text and images from the following articles

- (1) **Pradeep Kumar**, A. I. Maydykovskiy, Miguel Levy, N. V. Dubrovin, and O. A. Aktsipetrov, "Second harmonic generation study of internally generated strain in bismuth-substituted iron garnet films," OPTICS EXPRESS 18, 1076-1084 (2010).
- (2) Miguel Levy and **Pradeep Kumar**, "Nonreciprocal Bloch oscillations in magneto-optic waveguide arrays," OPTICS LETTERS 35, 3147-3149 (2010).
- (3) **Pradeep Kumar** and Miguel Levy, "Unidirectional optical Bloch oscillations in asymmetric waveguide arrays," OPTICS LETTERS 36, 4359-4361 (2011).
- (4) **Pradeep Kumar** and Miguel Levy, "On-chip optical isolation via unidirectional Bloch oscillations in a waveguide array," OPTICS LETTERS 37, 3762-3764 (2012).

I (Pradeep Kumar) have coauthored all the above four articles published in Optics Letters and Optics Express journals of OSA.

The text and images will appear in my PhD Dissertation currently entitled:

"NONLINEAR EFFECTS IN MAGNETIC GARNET FILMS
AND NONRECIPROCAL OPTICAL BLOCH OSCILLATIONS IN WAVEGUIDE
ARRAYS"

to be published by the Michigan Technological University in the Spring 2013.

Since Optical Society of America (OSA) is the copyrights holder, may I have the permission from OSA to reprint the above work in my PhD Dissertation? Please contact me if you have any questions regarding this request.

Sincerely,
Pradeep Kumar

Note: To comply with the copyright requirements of the OSA, all the four articles mentioned in the above email have been cited in the text and are listed in the Reference list as [24], [25], [42], and [105]. To comply with the requirements of the Graduate School at Michigan Technological University, a “Preface” is included at the beginning of this dissertation and footnotes are placed on the first page of Chapter 3 and Chapter 4.